

# **Modeling and Analysis of Metal Cutting Process using Self-Propelled Rotary Tools**

by

Waleed A. Abdelfattah Ahmed

A thesis submitted to the  
School of Graduate and Postdoctoral Studies in partial  
fulfillment of the requirements for the degree of

**Doctor of Philosophy in Mechanical Engineering**

Faculty of Engineering and Applied Science

University of Ontario Institute of Technology (Ontario Tech University)

Oshawa, Ontario, Canada

February 2021

## THESIS EXAMINATION INFORMATION

Submitted by: **Waleed A. Abdelfattah Ahmed**

### **Doctor of Philosophy in Mechanical Engineering**

Thesis title: Modeling and Analysis of Metal Cutting Process using Self-Propelled Rotary Tools
---

An oral defense of this thesis took place on January 27,2021 in front of the following examining committee:

#### **Examining Committee:**

Chair of Examining Committee	Dr. Scott Nokleby
Research Supervisor	Dr. Hossam Kishawy
Research Co-supervisor	Dr. Atef Mohany
Examining Committee Member	Dr. Sayyed Ali Hosseini
Examining Committee Member	Dr. Remon Pop-Iliev
University Examiner	Dr. Martin Agelin-Chaab
External Examiner	Dr. Stephen Veldhuis (McMaster University)

The above committee determined that the thesis is acceptable in form and content and that a satisfactory knowledge of the field covered by the thesis was demonstrated by the candidate during an oral examination. A signed copy of the Certificate of Approval is available from the School of Graduate and Postdoctoral Studies.

## **Abstract**

Machining difficult-to-cut materials is still one of the challenges facing different industries such as aerospace, nuclear and automotive sectors. That's mainly because of the excessive heat generated, which affects the tool wear behavior and machinability performance. Rotary tools can be employed to solve these issues as they offer an acceptable tool life compared to traditional tools, especially under dry-environment conditions. Despite the attempts offered in the area of machining with rotary tools, there is a noticeable lack in understanding the physical aspects and mechanics of this process. Thus, the current work focuses on three main pillars to fully address this research gap. The first pillar of this study presents a novel analytical model to predict the cutting forces and tool rotational speeds during the machining process using self-propelled rotary tools with considering the tool bearing friction. The prediction capabilities of this analytical model are higher than all existing models in the open literature. The objective of the second pillar is to propose a hybrid finite element model which is able to predict the temperature distribution during cutting with self-propelled rotary tools. The proposed model addresses the limitation of other previous models as it is purely focused on significant aspects such as; heat partition factor and the contact area between the tool and the chip. The simulation results in terms of cutting forces, temperature, heat flux, and the contact area between the chip and the tool are obtained, and good agreement is observed between the numerical and experimental results. In terms of the third pillar, deep-understanding of the process mechanisms is fully discussed through conducting experimental tests on AISI 4140 hardened-steel, followed by analysis of variance, empirical modeling of the process, and process optimization. Besides, a detailed mechanism for the machining process with self-propelled rotary tools is concluded. It should be stated that this work offers a valuable comprehensive analysis for the metal cutting industry in terms of modeling, optimization, and assessment of the machining process with rotary tools.

**Keywords:** machining; difficult-to-cut materials; rotary tools; modeling; optimization

## **Author's Declaration**

I hereby declare that this thesis consists of original work of which I have authored. This is a true copy of the thesis, including any required final revisions, as accepted by my examiners.

I authorize the University of Ontario Institute of Technology (Ontario Tech University) to lend this thesis to other institutions or individuals for the purpose of scholarly research. I further authorize University of Ontario Institute of Technology (Ontario Tech University) to reproduce this thesis by photocopying or by other means, in total or in part, at the request of other institutions or individuals for the purpose of scholarly research. I understand that my thesis will be made electronically available to the public.

---

Waleed A. Abdelfattah Ahmed

## **Acknowledgements**

The author would like to sincerely express his profound thanks to his supervisors, Dr. Hossam Kishawy and Dr. Atef Mohany, for their continuous guidance, suggestions, and support to conduct this research.

Sincerely thanks should go to all members in the Machining Research Laboratory (MRL), and in particular to Dr. Hussien Hegab for patiently and carefully reviewing my work. The author would also like to thank the committee members, Dr. Sayyed Ali Hosseini and Dr. Remon Pop-Iliev, for their helpful discussion during the regular research meetings.

Finally, the author is most grateful to his wife Fathia and sons, Salma, Salim, and Adam, for their encouragement during this endeavor.

## **Statement of Contributions**

Part of the work described in Chapter 4 and Chapter 5 has been published as:

Ahmed, W., Hegab, H., Kishawy, H. A., & Mohany, A. Estimation of temperature in machining with self-propelled rotary tools using finite element method. *Journal of Manufacturing Processes*, 61, 100-110.

The numerical model is an extension of the previous model(s) presented by Dr. Kishawy and his research group. I wrote the first draft of the manuscript.

## Table of Contents

Abstract .....	i
Author's Declaration.....	ii
Acknowledgements.....	iii
Statement of Contributions .....	iv
List of Tables .....	x
List of Figures .....	xi
List of Abbreviations and Symbols.....	xvii
Chapter 1: Introduction .....	1
1.1 Preamble .....	1
1.2 Machining with rotary tools.....	3
1.2.1 Types of rotary tools .....	4
1.3 Literature survey .....	5
1.4 Motivation.....	9
1.5 Objectives .....	10
1.6 Thesis outline .....	11
Chapter 2: Mechanics of metal cutting .....	13
2.1 Preamble .....	13
2.2 Orthogonal metal cutting .....	13

2.3 Merchant's Theory.....	17
2.4 Lee and Shaffer Theory .....	20
2.5 Oxley's Theory .....	22
2.6 Extension of Oxley's theory .....	26
2.6.1 Primary shear zone relationships .....	30
2.6.2 Secondary shear zone relationships .....	33
2.7 Armarego's rotary tools: fundamental study .....	36
2.8 Important relationships for machining with rotary tools .....	49
2.9 Prediction of the chip flow angle .....	54
Chapter 3: Analytical-based modeling of metal cutting process with SPRT.....	62
3.1 Preamble .....	62
3.2 Equivalent parameters.....	65
3.3 Orthogonal cutting forces .....	67
3.4 Radial cutting force.....	68
3.5 Bearing friction .....	70
3.6 Model validation and discussion.....	72
Chapter 4: Finite element modeling.....	77
4.1 Preamble .....	77
4.2 Model formation .....	78

4.3 Material modeling.....	80
4.4 Chip separation modeling .....	82
4.5 Failure damage models .....	84
4.5.1 Damage initiation.....	85
4.5.2 Damage evaluation.....	86
4.6 Friction modeling.....	88
4.7 Finite element modeling of machining with rotary tools.....	90
4.7.1 Model geometry and meshing.....	90
4.7.2 Material behavior .....	94
4.7.3 Chip formation modeling.....	95
4.7.4 Model validation and discussion.....	96
Chapter 5: Cutting temperature hybrid model .....	99
5.1 Preamble .....	99
5.2 Hybrid modeling approach: stages and methodology.....	100
5.3 Phase II: heat transfer modeling .....	102
5.4 Mesh and boundary conditions .....	103
5.5 Temperature model results and discussions.....	105
5.6 Mechanism of machining with SPRT .....	111
Chapter 6: Experimental setup.....	114

6.1 Preamble .....	114
6.2 Materials and Methods.....	114
6.3 Force measurements.....	116
6.4 Temperature measurements .....	117
6.5 Surface roughness measurements .....	118
6.6 Tool wear measurements .....	119
6.7 Tool rotational speed measurements.....	120
6.8 Plan of experimentation .....	120
Chapter 7: Experiments results and analysis .....	124
7.1 Preamble .....	124
7.2 Mapping matrix results .....	126
7.3 Cutting forces results and discussion.....	127
7.4 Flank tool wear results .....	132
7.5 Average surface roughness results.....	136
7.6 Temperature results and influence of the tool speed on the thermal behavior	139
7.7 Machining performance characteristics modeling and optimization .....	144
7.8 Optimized scenarios.....	149
Chapter 8: Conclusions .....	152
Chapter 9: Thesis contributions and future work.....	156

9.1 Contributions.....	156
9.2 Future work.....	156
References.....	158

## List of Tables

Table 4-1: Properties of the uncoated carbide [126].....	92
Table 4-2. AISI/SAE 1045 chemical composition [85].....	94
Table 4-3. Mechanical properties and Johnson–Cook parameters for AISI 1045 steel [127].....	94
Table 4-4. Johnson–Cook damage parameters for AISI 1045 steel [128].....	95
Table 4-5. Validation tests cutting conditions .....	96
Table 6-1. AISI 4140 steel properties [137] .....	115
Table 6-2. Assigned level to the design variables.....	121
Table 6-3. L16OA for the experiment runs .....	122
Table 7-1. Experimental plan results .....	126
Table 7-2. Quality levels.....	127
Table 7-3. Tests mapping matrix .....	127
Table 7-4. ANOVA response table for resultant cutting force (N) means .....	130
Table 7-5. ANOVA response table for flank tool wear ( $\mu\text{m}$ ) means.....	134
Table 7-6. ANOVA response table for surface roughness ( $\mu\text{m}$ ) means .....	138
Table 7-7. ANOVA response table for the tool rotational speed (RPM) means .....	140
Table 7-8. ANOVA response table for the tool temperature ( $^{\circ}\text{C}$ ) means.....	143
Table 7-9. Weighting factors for the machining scenarios .....	150
Table 7-10. A summary of the optimal solutions for the studied scenarios .....	151

## List of Figures

Figure 1-1. Machining with self-propelled rotary tools.....	4
Figure 1-2. Types of rotary tools [12].....	5
Figure 1-3. Rotary tool inclination types [44] .....	7
Figure 2-1. Basic cutting processes [65]; orthogonal (a) and oblique (b) .....	14
Figure 2-2. Examples of orthogonal metal cutting [67]; tube-end turning (a) and transverse turning (b) .....	16
Figure 2-3. Merchant's orthogonal cutting model [71] .....	17
Figure 2-4. Velocity triangle at the shear zone [71] .....	18
Figure 2-5. Slip line field model geometry [69] .....	21
Figure 2-6. Oxley orthogonal cutting model [64]; deformation zone (a) and simplified deformation zone (b).....	23
Figure 2-7. Oxley orthogonal cutting model flow chart [64].....	24
Figure 2-8. Tool-chip interface forces and stresses [64].....	25
Figure 2-9. Flow chart for the modified Oxley model [80] .....	29
Figure 2-10. Oxley orthogonal cutting model geometry [64].....	30
Figure 2-11. Rotary tools tube-end turning [57]; tool above the workpiece center (a), tool in the same level of the workpiece center (b), and tool below the workpiece center (c) .....	37
Figure 2-12. An actively driven rotary tool [57]; an oblique case (a) and its equivalent classical process (b) .....	39

Figure 2-13. Stationary rotary tool [57]; an oblique case (a) and its equivalent classical process (b).....	41
Figure 2-14. An actively driven rotary tool [57]; an oblique case (a) and its equivalent classical process (b) .....	42
Figure 2-15. An actively driven rotary tool [57]; an oblique case (a) and its equivalent classical process (b) .....	44
Figure 2-16. An actively driven rotary tool [57]; an oblique case (a) and its equivalent classical process (b) .....	45
Figure 2-17. Self-propelled rotary tool [57]; tool positioned above the workpiece center (a) and its equivalent classical process (b).....	47
Figure 2-18. Self-propelled rotary tool [57]; tool positioned below the workpiece center (a) and its equivalent classical process (b).....	48
Figure 2-19. Rotary tools velocities.....	49
Figure 2-20. The geometry of the chip area at the nose radius cutting edge [83] .....	55
Figure 2-21. Velocity vectors and chip widths for machining using self-propelled rotary tools [84] .....	57
Figure 2-22. The geometry of the chip flow angle calculation [84] .....	59
Figure 3-1. Kinematics of machining with SPRT.....	63
Figure 3-2. Flowchart for the cutting forces and tool motion predictions .....	64
Figure 3-3. Velocity and chip width relations in SPRT .....	65
Figure 3-4. A comparison between the predicted and measured forces at cutting velocity of 120 m/min.....	73

Figure 3-5. A comparison between the predicted and measured forces at cutting velocity of 170 m/min.....	73
Figure 3-6. A comparison between the predicted and measured forces at cutting velocity of 230 m/min.....	74
Figure 3-7. A comparison between the predicted and measured tool rotational speeds .....	76
Figure 4-1. Arbitrary Lagrange-Eulerian (ALE) boundary conditions [89] .....	80
Figure 4-2. Node separation technique [102] .....	83
Figure 4-3. Element deletion technique [104] .....	83
Figure 4-4. Stress-strain relation for a metal workpiece.....	85
Figure 4-5. Normal and shear stresses along the rake face [108] .....	89
Figure 4-6. Rotary insert geometry and mesh.....	92
Figure 4-7. Workpiece geometry and mesh (left-side), tool-workpiece assembly (right-side).....	93
Figure 4-8. A comparison between the predicted and experimental [85] forces .....	97
Figure 4-9. A comparison between the simulated chip morphology and experimental chips images at 130 m/min cutting velocity and 0.225 mm/rev feed rate: left is the chip's image obtained by Parker [129] and right is the ESM image obtained by Zhang [130].....	97
Figure 4-10. A comparison between the predicted and experimental [84] chip flow angle at 230 m/min cutting speed and 0.2 mm/rev feed rate .....	98
Figure 5-1. Heat generation in metal cutting .....	99

Figure 5-2. Hybrid model flowchart .....	102
Figure 5-3. COMSOL tool model geometry.....	104
Figure 5-4. COMSOL tool model mesh .....	105
Figure 5-5. Rotary tool predicted temperature distribution (in °C) at 170 m/min cutting speed and 0.2 mm/rev feed rate .....	106
Figure 5-6. Temperature distribution over the rake face for fixed and rotating cases (in °C) at 170 m/min cutting speed and 0.2 mm/rev feed rate .....	107
Figure 5-7. Average tool temperature for fixed and rotating cases (in °C) at 170 m/min cutting speed and 0.2 mm/rev feed rate .....	107
Figure 5-8. Temperature pattern at an intermediate cross-section plane of fixed and rotating cases (in °C) at 170 m/min cutting speed and 0.2 mm/rev feed rate .....	108
Figure 5-9. Heat flux distribution over the rake face (in w/m <sup>2</sup> ) at cutting speed of 170 m/min cutting speed and feed rate of 0.2 mm/rev .....	109
Figure 5-10. COMSOL tool temperature distribution (in °C) at 170 m/min cutting speed and 0.2 mm/rev feed rate .....	109
Figure 5-11. The temperature influence over the tool rake face for four different cases .....	110
Figure 5-12. Tool temperature history of a point on the cutting edge at 170 m/min cutting speed and 0.2 mm/rev feed rate .....	111
Figure 5-13. Schematic of machining using a rotary tool.....	112
Figure 6-1. Tube shape workpiece.....	114
Figure 6-2. Schematic of the experimentation setup for machining with a self-propelled rotary tool.....	116

Figure 6-3. The used equipment for measuring forces .....	117
Figure 6-4. Optris PI 640 infra-red thermal camera .....	117
Figure 6-5. A sample of temperature measurement.....	118
Figure 6-6. Surface roughness tester (Mitutoyo SJ.201) .....	119
Figure 6-7. Toolmaker microscope (Mitutoyo TM-A505B) .....	119
Figure 6-8. Digital laser tachometer .....	120
Figure 7-1. Flowchart for the experimental methodology .....	125
Figure 7-2. Cutting forces results.....	128
Figure 7-3. Cutting force in Z-direction, at $V = 240\text{mmmin}$ , $f = 0.3\text{mmrev}$ , and $i = 5^\circ$ .....	128
Figure 7-4. Cutting force in y-direction, $V = 127\text{mmmin}$ , $f = 0.25\text{mmrev}$ , and $i = 15^\circ$ .....	129
Figure 7-5. Design variables effect on the resultant cutting force .....	131
Figure 7-6. Resultant cutting force results for rotatory tool versus fixed tool at worst and best conditions.....	132
Figure 7-7. Flank tool wear results .....	133
Figure 7-8. Design variables effect on the flank tool wear.....	134
Figure 7-9. Average flank tool wear results for rotary tool versus fixed tool at worst and best conditions.....	135
Figure 7-10. A Comparison between the finished surface and corresponding tool damage based on the tool inclination angle; (a, and c) at $20^\circ$ and (b, and d) at $5^\circ$ ...	136

Figure 7-11. Average surface roughness results .....	137
Figure 7-12. Design variables levels effect on the surface roughness .....	138
Figure 7-13. Surface roughness results for rotary tool versus fixed tool at worst and best conditions .....	139
Figure 7-14. Design variables levels effect on the tool rotational speed .....	141
Figure 7-15. Cutting temperature results .....	142
Figure 7-16. Design variables levels effect on the cutting temperature .....	143
Figure 7-17. Cutting temperature results for rotary tool versus fixed tool at worst and best conditions .....	144
Figure 7-18. A Comparison between experimental and predicted flank tool wear ..	146
Figure 7-19. A Comparison between experimental and predicted average surface roughness .....	146
Figure 7-20. (a) Individual's binary representation (genotype), (b) schematic of the crossover process, (c) schematic of the mutation process .....	147
Figure 7-21. Pareto-front solutions .....	149
Figure 7-22. Experimental validation of the optimized scenarios results; (a) Average surface roughness and (b) Flank tool wear .....	151

## List of Abbreviations and Symbols

$B$	Width of cut
$B_c$	Chip width
$B_{cr}$	Relative chip width
$b$	Equivalent width of cut
$C_o$	Ratio between the length of the plane AB to the primary shear zone thickness
$C_p$	Specific heat
$F$	Friction force
$F_C$	Cutting force
$F_t$	Thrust force
$F_n$	Normal to AB force
$F_s$	Shear force
$F_R$	Radial force
$F_r$	Tangential force component
$f$	Feed rate
$f_y$	Feed rate in the y-direction
$G_f$	Energy of fracture
$H$	Chip-tool contact length
$H_V$	Vickers hardness
$h$	Contact length
$i$	Tool inclination angle
$i_s$	Static inclination angle
$i_w$	Angle of the cutting velocity
$i_{wr}$	Angle of the relative cutting velocity
$K$	Thermal conductivity
$K_{AB}$	Shear stress along AB plane
$K_{chip}$	Chip's shear stress
$L$	Characteristic length

$l$	Length of plane AB
$l_c$	Chip length
$m$	Slope between the shear and normal stresses
$m_{chip}$	Chip load
$N$	Normal to rake face force
$n$	Material strain hardening expansion
$P_n$	Normal plane
$Q_{SZ}$	Heat of the second shear zone
$Q_{chip}$	Heat of the chip
$Q_{tool}$	Heat of the tool
$Q_{cond}$	Conduction heat
$Q_{motion}$	Motion heat
$\dot{Q}$	Volume heat source
$R$	Resultant cutting force
$R_T$	Dimensionless thermal number
$r_l$	Chip length ratio
$T$	Temperature
$T_{ref}$	Reference temperature
$T_{room}$	Room temperature
$T_{melt}$	Melting temperature
$T_{mod}$	Modified temperature,
$T_{AB}$	Temperature of plane AB
$T_{int}$	Temperature of the tool-chip interface
$T^*$	Homogeneous temperature
$T_b$	Torque of bearing
$t_c$	Chip thickness
$t_{cr}$	Relative chip thickness
$t_1$	Uncut chip thickness
$t_2$	Deformed chip thickness

$V_c$	Chip velocity
$V_s$	Shear velocity
$V_W$	Cutting velocity
$V_{wr}$	Relative cutting speed
$V_r$	Tool speed
$\tau$	Shear stress
$\tau_{int}$	Shear stress of the secondary shear zone
$\tau_f$	Friction stress
$\tau_Y$	Yield stress
$\sigma_N$	Normal stress of the secondary shear zone
$\sigma^0$	Material flow stress
$\sigma_1$	Material strength coefficient
$\bar{\sigma}$	Equivalent stress
$\bar{\epsilon}_{pl}$	Equivalent plastic strain
$\dot{\bar{\epsilon}}_{pl}$	Equivalent plastic strain rate
$\dot{\epsilon}_0$	Reference strain rate
$\epsilon_{AB}$	Strain of the plane AB
$\epsilon_{int}$	Equivalent strain in the secondary shear zone
$\dot{\epsilon}_{int}$	Equivalent strain rate in the secondary shear zone
$\mathcal{E}^f$	Fracture strain
$\dot{\mathcal{E}}^*$	Dimensionless strain rate
$\bar{\mathcal{E}}_F^p$	Fracture equivalent plastic strain
$\gamma_{AB}$	Average shear strain of plane AB
$\dot{\gamma}_{AB}$	Average shear strain rate of plane AB
$\gamma_{jnt}$	shear strain of the secondary shear zone
$\mu$	Coefficient of friction
$\emptyset$	Shear flow angle
$\alpha$	Rake angle

$\lambda$	Friction angle
$\theta$	Angle between R and AB plane
$\delta$	Ratio between the thickness of the secondary deformation shear zone and the chip's thickness
$\rho$	Density
$\eta_c$	Chip flow angle
$\psi$	Relative chip flow angle
$\alpha_e$	Equivalent rake angle
$\alpha_n$	Normal rake angle
$\phi_n$	Normal shear angle
$\Omega$	Angle of the friction force
$\bar{\Omega}$	Resultant chip flow angle
$\mu_b$	Bearing friction coefficient
$\bar{u}^p$	Equivalent plastic displacement
$\omega$	Rotational speed vector
$\Delta T_{SZ}$	Primary shear zone temperature rise
$\Delta T_M$	Temperature rise of the deformed chip
$\Delta T_c$	Average chip temperature rise
ADRT	Actively driven rotary tools
ALE	Arbitrary Lagrangian-Eulerian
ANOVA	Analysis of variance
BUE	Built-up edge
DOE	Design of experiments
FEM	Finite element modeling
GP	Genetic programming
HPC	High-pressure coolant
MQL	Minimum quantity lubrication

MRR	Material removal rate
NSGA-II	Non-dominated sorting genetic algorithm
SPRT	Self-propelled rotary tools

# Chapter 1: Introduction

## 1.1 Preamble

Machining processes are widely used in manufacturing industries. In metal cutting, the final product is developed by removing parts of raw materials in the shape of chips until reaching the required size and shape. Machining is usually common in manufacturing metal parts; however, it also can be used with other materials such as wood, plastic, composites, and ceramic. The machining processes are normally followed by other manufacturing processes such as casting and forging. Furthermore, machining is used in nearly all mechanical components manufacturing at some stage. Therefore, studying such processes is always required to have a deep understanding of the mechanics and mechanisms of metal cutting processes. Understanding such aspects will support in enhancing the machinability of certain alloys, reducing the cycle time, decreasing the harmful environmental effect, and improving the economies.

Cutting tools are used to remove part of the workpiece material during the machining process. The cutting tools may have one cutting edge, such as turning, or more than one cutting edge, such as milling. To perform a metal cutting operation, the cutting tool materials must be harder than the workpiece materials [1]. During the cutting process, the cutting edge is exposed to severe temperatures and forces. These conditions result in increasing the tool wear rate, which leads to tool failure after a certain time. The tool wear rate issue becomes significant when machining Difficult-to-Cut materials. This tool wear depends on many parameters, such as the temperature, cutting conditions, and cooling mechanism. Two important indicators are used to control the machining cost; the tool life and material removal rate (MRR). Thus, to reduce the cost and the time, the tool life and MRR should be increased to the highest possible values. However, it is not easy to achieve both objectives at the same time when machining difficult-to-cut materials.

There are many studies have been focused on difficult-to-cut materials due to their low productivity and relatively high machining cost. In a previous work [2], Kishawy experimentally discussed the effects of different design parameters on the temperature of the cutting edge during high speed machining of D2 tool steel. One of the main reasons behind the temperature issue during machining difficult-to-cut materials is the low thermal conductivity of these materials, which leads to an excessive level of heat generation in the cutting zone due to the low heat dissipation rate. Accordingly, high tool wear, low productivity, and high cost associate the machining processes of the difficult-to-cut materials. However, regardless the mentioned issues, these materials are widely used in many engineering applications such as aerospace and automotive sectors, in which around two-thirds of all difficult-to-cut materials alloys are used, while the third portion is used in gas turbines, furnaces, oil, and chemical industry [3]. These materials are the first choice for many engineering applications due to their superior properties. These properties include high strength to weight ratio, high temperature, and chemical resistance [4]. Difficult-to-cut materials include titanium alloys, nickel-based alloys, stainless steel alloys, ceramics, and composites [5-7]. Therefore, machining difficult-to-cut materials should be studied to solve the associated problems with machining such materials.

Several studies have been done in the metal cutting area to investigate, model, and increase the efficiency of machining processes. Using cutting fluid is one of the major environmental concerns during metal cutting. Moreover, the usage of the coolant represents around 5 to 15 % of the total machining cost [8]. However, coolant fluids have a significant effect on the tool life and quality characteristics of machining processes. That is because the coolant has three main functions, which are dissipation of the heat generated in the cutting zone, lubrication between the workpiece and the tool, and removal of the produced chip. Flood coolant offers proper cooling and lubricating; however, flood coolant has a severe environmental and social impact. New techniques are presented throughout the literature as alternatives to the flood coolant method, such as minimum quantity lubrication (MQL), where a low amount of coolant is used, dry machining, high-pressure coolant (HPC), and cryogenic cooling. These

techniques have many benefits in terms of cost, health, and environmental impact [9-11]. However, applying these techniques still needs more improvements to become efficient alternatives.

As mentioned before, reducing cost and environmental impact are essential objectives in any machining process. Reducing the cost can be obtained by increasing tool life and material removal rate, while reducing the health and environmental impact can be achieved by the dry machining. However, those two factors are contradictory. In other words, using dry machining has less environmental impact comparing with flood coolant and is much safer for workers' health. Besides, dry machining saves the coolant cost, which is about 10 to 15 %, as mentioned before. Still, dry machining highly increases the tool wear rate, especially when machining difficult-to-cut materials, which significantly affects the machining cost. Beside, using dry machining increases the friction between the tool and the workpiece, which accordingly reduces the surface quality, especially when machining aerospace alloys.

## **1.2 Machining with rotary tools**

In the conventional cutting tools (i.e., single point cutters), the cutting point is continuously in contact with the workpiece. As a result of the machining process, high stresses and heat are generated in the cutting zone. That causes the cutting point to be exposed to a severe temperature, which leads to high tool wear rate and short tool life. Rotary tools can be used to solve the temperature issue by offering the ability to machine difficult-to-cut materials even under dry conditions with suitable tool life. In the rotary tool, the tool takes the shape of a circular disc, which has a sharp cutting edge along the whole outer circumference. During machining, the tool rotates around its axis; this angular motion allows the interaction between the tool and the workpiece to occur over the whole perimeter of the cutting edge instead of at a single-point. Thus, the tool wear is much smaller compared to the traditional tool. Figure 1-1 shows a schematic for the machining process using self-propelled rotary tools.

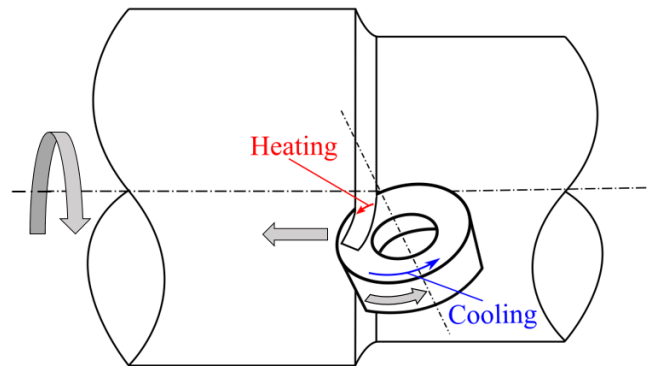


Figure 1-1. Machining with self-propelled rotary tools

### 1.2.1 Types of rotary tools

There are two main types of rotary tools: self-propelled rotary tools (SPRT) and actively driven rotary tools (ADRT). For actively driven rotary tools (ADRT), the tool is rotating by an external motor. Therefore, the rotational speed and the rotation direction (clockwise or counter-clockwise) can be controlled by the motor. Besides, the cutting process is not necessary to be oblique cutting because the tool motion occurs by an external power source (i.e., machine shaft or tool motor). For self-propelled rotary tools (SPRT), the tool rotates around its axis by the interaction between the tool and the workpiece. During the metal cutting, part of the raw material is removed in the shape of chips. The generated chip is then sliding over the tool rake face, and friction force is generated between the chip and the tool. The cutting process in the case of self-propelled rotary tools (SPRT) must be oblique, that means, the inclination angle between the tool and the workpiece axis ( $i$ ) should not be equal to zero. In other words, the friction force should have an angle with the tool axis; therefore, the tangential component of the friction force can guide the tool to rotate in the proper direction. Figure 1-2 shows types of rotary tools.

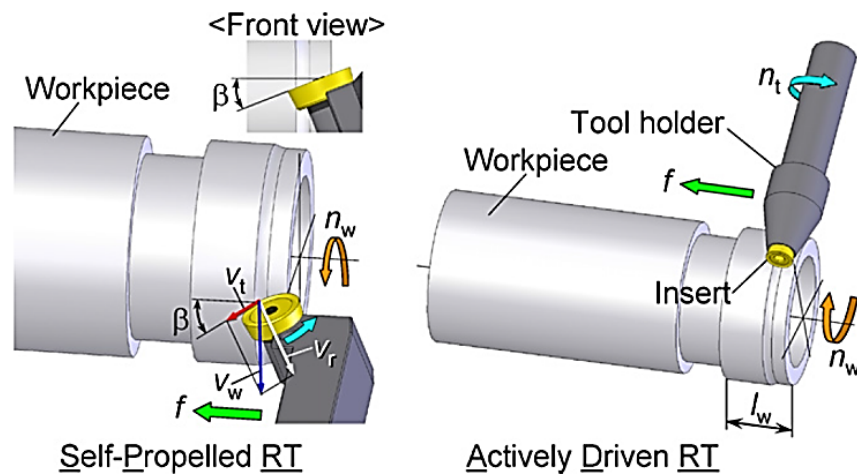


Figure 1-2. Types of rotary tools [12]

### 1.3 Literature survey

It seems that there is no clear time in which rotary tools were firstly foreseen. Shaw et al. [13] have mentioned that in 1868 James was the first person who predicted the importance of the rotary tools. However, there are no available details for this work. The first appearance of rotary tools papers was in the 1930s. In 1934 Sokolov [14] has published the first known paper in this area of research (i.e., machining using rotary tools). Afterward, R.G.H in 1936 [15] performed orthogonal cutting using self-propelled rotary tools.

In 1952, Shaw et al. [13] have developed the most significant work that shows theoretically and experimentally the advantages of applying the rotary tools. In this study, the first attempt to use a driven type rotary tool was carried out to perform orthogonal cutting. Since a driven type is used, the tool motion must be provided using an external source. The drilling machine was mounted over the bed of a center lathe, and the cutting insert was attached to the driller shaft. Consequently, the tool rotational speed could be independently controlled. The influence of the cutting edge motion on the machining characteristics (i.e., cutting forces, chip formation, and temperature) was

deeply investigated in this study. A comparison between rotary and conventional tools was provided. The tool rotational speed was considered to define the absolute and relative cutting velocities. Extended forces relationships were also presented in their work.

In the early 1950s, Zhivchikov [16] investigated the application of the SPRT with reverse feed. The influence of different aspects, such as the tool speed, rake angle, and clearance angle, on the machining performance were discussed.

Through the literature, it seems that there was no significant work in the rotary tools area from 1952 to 1962. However, by 1963, many papers have been published in the rotary tools area, especially from the Soviet Union. For example, there are three papers [17-19] that can be found in the proceeding of the machining titanium and heat resistant alloys conference. In these papers, different aspects such as geometrical parameters, wear mechanism, chip formation, and machining surface quality were investigated.

Zemlyanskii et al. have published many papers in the area of machining using rotary tools [20-29]. Different types of workpiece materials have been used in their studies. The workpieces material used were: carbon steel, zinc, nickel alloys, copper, brass, cast iron, and titanium alloys. High-speed steel (HSS) round cutting inserts were used, and wide ranges of operating conditions were investigated. They found that the cutting and thrust forces were mainly affected by the insert inclination angle. On the other hand, the feed force was almost constant. The effect of workpiece materials and cutting velocities on the cutting forces were presented. The rake angle variations showed a low effect on the cutting forces. Moreover, increasing the depth of cut resulted in an increase in the thrust and cutting forces.

Granin [30, 31] studied the tool life and surface roughness when machining using rotary tools. The theoretical surface roughness model was presented, and the rotary tools showed the ability to generate a better surface quality compared to the conventional tools under the same operating conditions. Dramatically increase in the tool life was obtained when using rotary tools. That is mainly due to the low friction

coefficient and the large diameter of the cutting inserts. Koosher and Reznikov [19, 32-34] developed modified fixtures of the tools, which were used for milling and shaping operations.

Afterward, attempts were developed in the Soviet Union to use the side face of the round insert as the rake face, while the top face becomes the flank face (type II in Figure 1-3) [35-37]. This configuration was used in the finishing or semi-finishing processes as it generates good surface quality. A theoretical surface roughness model was developed in their works. The same technique was also studied in the 1970s [38, 39]. In these studies, the difference between the regular rotary tools and the modified ones was discussed. High-speed steel round inserts were used to perform face milling operation using the self-propelled rotary technique [40]. The main differences between the rotating case and the fixed one were investigated in this study. No built-up edge, low tool wear rate, and lower temperature were observed when machining using the rotary tools compared to the fixed cases. The rotary tools technique was then studied in India [41, 42], and later on, it reached U.K. [43].

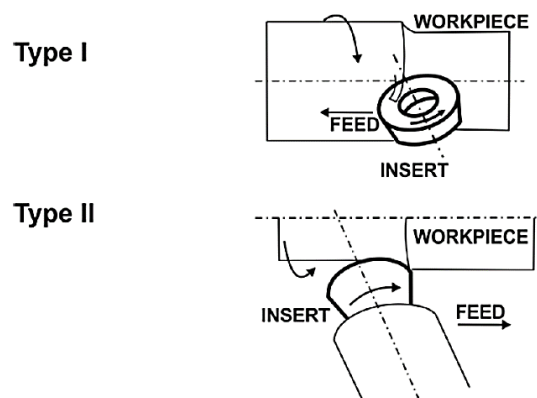


Figure 1-3. Rotary tool inclination types [44]

In the early stages of the research on machining with rotary tools, most of the papers studied the theoretical aspects of rotary tools [13-16, 43]. On the other hand, the industrial applications and structure design of the tool were studied [43, 45-54].

Therefore, different designs have appeared, which allows the rotary tools cutters to be commercially available [55].

In the 1990s, Armarego et al. [56-58] have developed important studies, which include analytical models based on the fundamental principles. An equivalent orthogonal model was developed for the self-propelled machining process, while an equivalent oblique model was presented for the actively driven rotary tool. The tool rotational speed was considered in their equivalent models.

Chen et al. [59] have studied the utilization of self-propelled rotary tools in machining a modern difficult to cut material, SiC whisker-reinforced aluminum composite workpiece. The tool performance was studied, and dramatically increasing in the tool life was noticed for the self-propelled rotary tools compared to the fixed tools and single point conventional tools. Distribution of the tool wear over the whole insert circumference and reduction of the relative cutting speeds lead to a reduction in the tool wear rate and residual stresses. As a result, high cutting velocities and feed rates were used to increase the material removal rate.

Recently, Kishawy et al. [60, 61] have developed self-propelled rotary tools studies. There was no crater wear observed due to the noticeable lower temperature. Besides, Kishawy et al. [62] have developed a model to predict the tool temperature when machining using self-propelled rotary tools. Sasahara et al. [63] have studied the thermal characteristics for the actively driven rotary tools, and they showed that there is a heating-cooling cycle for each point of the cutting edge. Thus, the generated heat in the cutting zone can be carried away by the tool. As a result, the tool cutting edge temperature can be reduced by offering a fresh cooled portion to the cutting zone and taking away the hot portion to cool down before feeding it again to the cutting zone. According to that, the rotary tools can be used in machining difficult-to-cut materials without using coolant fluids and retain the tool temperature and tool wear within acceptable limits.

## 1.4 Motivation

Difficult-to-cut materials are used in many applications such as aerospace, automotive, chemical, and oil industries. The reason behind that is the promising properties of these materials. For example, high strength to weight ratio, high corrosion resistance, high chemical resistance, and the ability of these materials to retain their properties at high levels of temperature. Machining of difficult-to-cut materials is still suffering from low productivity and relatively high machining cost. That is because the machining of these materials is usually associated with very high thermal loads due to their low thermal conductivity, which leads to a very high temperature in the cutting zone. Thus, there is a need to improve the machinability of Difficult-to-cut materials.

The flood coolant approach can be used with conventional cutting tools when machining difficult-to-cut materials to avoid the temperature issue by dissipating the generated heat. However, using flood coolants has harmful effects on the environment and the workers' health. Therefore, the usage of the flood coolant should be avoided as possible in the metal cutting industries.

Many alternative methods were studied in the open literature, which could include as options to address the flood coolant issue. These methods include minimum quantity lubrication (MQL), high-pressure coolant (HPC), and internal tool cooling. However, these methods still need to be improved in order to replace the flood coolant.

The rotary tool is one of the efficient methods that can be used in machining difficult-to-cut materials. Not only because it offers the entire perimeter as a cutting edge instead of a single point, which highly reduces the tool wear, but also because it keeps the temperature within the acceptable limit, even under dry conditions, which is environment friendly and has no effect on the workers' health. Besides, Rotary tool opens up new opportunities for optimizing performance to fully take advantage can redesign tool materials, coatings, machining time. Thus, research in this area is still needed to provide a deep understanding of the complex interaction between the tool

and the workpiece in order to improve the performance of the machining process using SPRT.

## 1.5 Objectives

The analysis of a metal cutting process is essential to correlate the machining performance indicators (e.g., forces, stress, temperature, and tool wear) to the process inputs such as feed, cutting speed, depth of cut, tool geometry, and materials. Three different techniques are used to analyze the machining processes; experiments, numerical modeling (e.g., finite element), and analytical modeling. Each one of these techniques has the advantage of predicting different outputs. In the current study, the three techniques are used to provide a comprehensive analysis of metal cutting using self-propelled rotary tools.

Several experimental studies were developed in the rotary tools area, while very few analytical studies were performed. All these studies have demonstrated that rotary tools offer many benefits in terms of temperature, tool life, and power consumption compared to traditional tools. However, there is still a need to provide a deep understanding of such a complex process. Thus, the objectives of this study are classified into different phases, as follows:

- Develop a novel analytical model to accurately correlate and predict cutting forces and tool rotational speed for different workpiece materials when machining using self-propelled rotary tools. The tool bearing friction will be considered in this model to obtain the tool drive force component.
- Offer a solid numerical model to deeply understand the mechanics of the cutting process using a self-propelled rotary tool in terms of heat transfer mechanism and the interaction between the cutting tool and workpiece, which can be achieved by:
  - Build up three-dimensional geometry for the tool and the workpiece
  - Define the tool and the workpiece materials models
  - Define accurate interaction characteristics between the tool and the workpiece

- Analysis of the cutting process aspects that are not easy to measure experientially, such as temperature field
- Develop a hybrid approach to provide the steady-state tool temperature distribution
- Experimentally investigate the effects of the cutting conditions on the overall machining performance, which can be achieved by:
  - Use the Taguchi design of experiments (DOE) approach to build up the tests matrix
  - Apply analysis of variance (ANOVA) technique to study the effect of every studied design variable on the machining performance
  - Develop data models for the measured performance indicators using genetic programming
  - Perform multi-objective optimization for the developed models using the non-dominated sorting genetic algorithm (NSGA-II) to generate the Pareto-front optimal solutions
  - Optimize the Pareto-front solutions based on different machining scenarios (i.e., finishing and productively)

## 1.6 Thesis outline

This thesis consists of nine chapters, as follows:

- Chapter 1 provides an introduction to the importance of using the self-propelled rotary tools when machining difficult-to-cut materials. Literature survey, motivations, and objectives of the current research are presented in this chapter.
- Chapter 2 provides a background on the metal cutting process. Previous studies, which are directly related to the current research, are presented in detail.
- Chapter 3 provides an analytical-based model to predict the cutting forces and tool rotational speed, which is a significant design aspect when machining with self-propelled rotary tools. To minimize the model assumptions and maintain high accuracy, the bearing friction of the cutting insert is considered.

- Chapter 4 provides descriptions for the finite element aspects, which are mandatory to simulate the metal cutting process. A 3-D numerical simulation for the machining process using SPRT is developed based on materials plastic model, damage model, and friction law. ABAQUS commercial software is used to perform the simulation process.
- Chapter 5 provides a hybrid model to predict and investigate the temperature characteristics when machining using self-propelled rotary tools. Two separate phases are employed to study the steady-state temperature field. In the first phase, the outputs of the 3-D ABAQUS model are used to obtain the second phase boundary conditions. In the second phase, COMSOL software is utilized to achieve a steady-state temperature distribution.
- Chapter 6 provides detailed information regarding the used materials, measuring equipment, and the experimental plan.
- Chapter 7 provides the experimental results in terms of cutting forces, tool wear, temperature, tool rotational speed, and surface roughness. The analysis of variance (ANOVA) is utilized to determine the significant design variables for each performance indicator and to select the optimum level of each variable. Genetic programming is used to correlate the tool wear and surface roughness to the decision variables. Afterward, the non-dominated sorting genetic algorithm (NSGA-II) is used to perform multi-objective optimization of the machining process.
- Chapter 8 provides the conclusions of the current research findings.
- Chapter 9 provides the contributions of the current work and recommendations for future work.

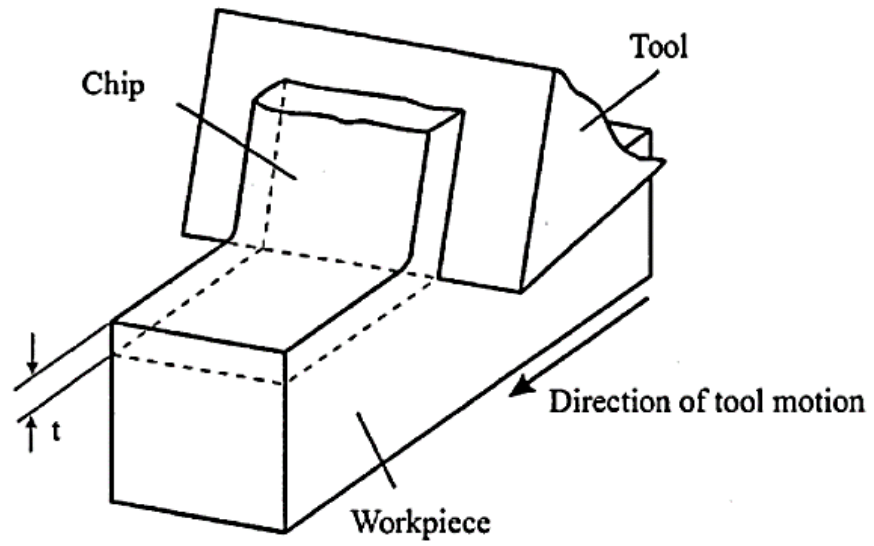
# Chapter 2: Mechanics of metal cutting

## 2.1 Preamble

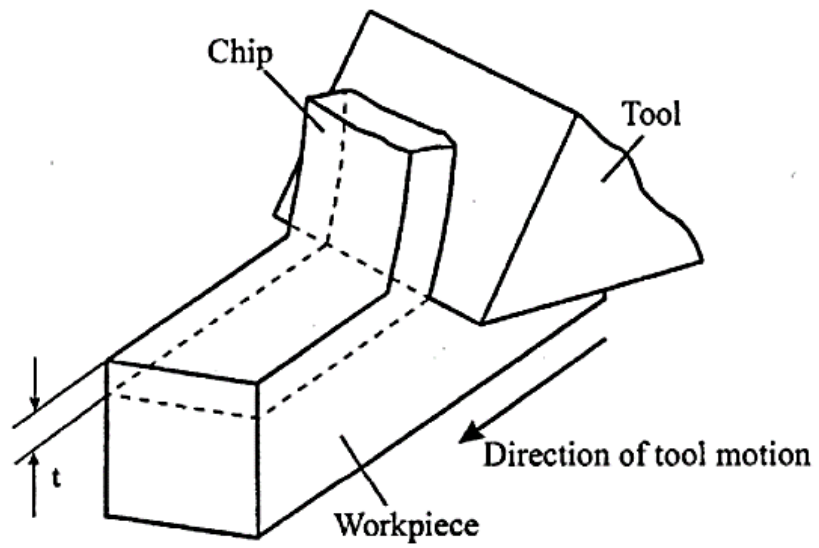
Metal cutting processes (e.g., turning, milling, and drilling) are usually used at some stages of any product manufacturing process. That is due to the ability to produce accurate dimensions and good surface finishing compared to other manufacturing processes such as casting. For example, the manufacturing of the engine blocks usually starts with casting or forging, and then metal cutting is required to get the accurate dimensions and gaps between parts. This chapter provides a background on the metal cutting process. Previous studies, which are directly related to the current research, are also presented in details.

## 2.2 Orthogonal metal cutting

There are two fundamental types of metal cutting processes: orthogonal and oblique metal cutting. In the orthogonal cutting process, the cutting edge is normal to the cutting velocity direction (see Figure 2-1). According to Oxley [64], when the width of cut ( $w$ ) is equal or higher than ten times of the uncut chip thickness ( $t_1$ ), the plane strain assumption can be used. Hence, there is no chip side flow occurs parallel to the cutting edge. Therefore, two-dimension geometry can be used to model the cutting process.



(a) Conventional orthogonal cutting



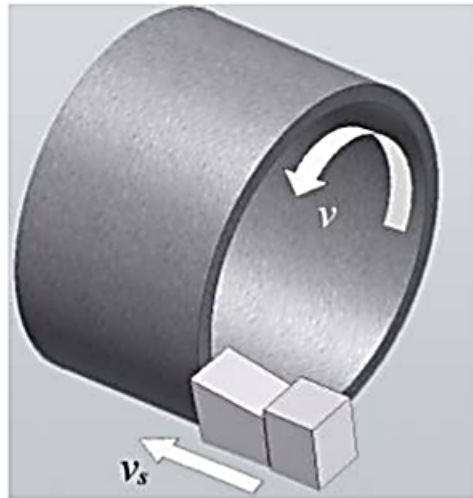
(b) Conventional oblique cutting

Figure 2-1. Basic cutting processes [65]; orthogonal (a) and oblique (b)

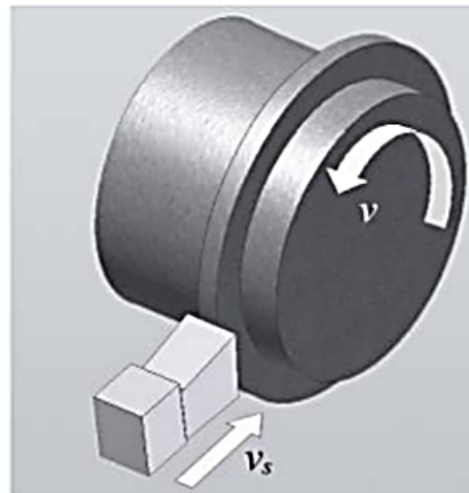
Two different methods can be used to experimentally perform the orthogonal cutting. The first one is the transverse turning operation with a width of cut equal to or higher than ten times the feed. The other way is the tube end turning with a thickness equal to or higher than ten times the feed, as shown in Figure 2-2. The tube diameter should be large enough; therefore, the cutting velocity variation can be ignored. The following assumptions are used to analysis the orthogonal cutting process based on the plane strain concept [66]:

- There is no thickness for the primary shear plane ( $AB$ )
- The tool has a sharp edge, and there is no plowing or rubbing in the cutting zone
- The shear plane stresses are uniformly distributed
- The tool-chip interference force ( $R$ ) is equal and opposite in direction to the resultant cutting force ( $R$ )

According to Merchant, by using the forces balance, the feed force ( $F_T$ ) and the cutting force ( $F_C$ ) are related to the material's shear stress ( $\tau$ ), coefficient of friction ( $\mu$ ), shear flow angle ( $\phi$ ), width of cut ( $w$ ), rake angle ( $\alpha$ ), and undeformed chip thickness ( $t_1$ ).



(a)



(b)

Figure 2-2. Examples of orthogonal metal cutting [67]; tube-end turning (a) and transverse turning (b)



In Figure 2-3,  $\alpha$  is the tool rake angle, and  $\phi$  is the shear flow angle.  $t_1$  is the uncut chip thickness, and  $t_2$  is the deformed chip thickness. The shear flow angle  $\phi$  can be presented in equation 2-1:

$$\tan \phi = \frac{(t_1/t_2) \cos \alpha}{1 - (t_1/t_2) \sin \alpha} \quad 2-1$$

Figure 2-4 shows the velocity triangle at the shear zone, which can be utilized to drive the following equations:

$$V_s = U \frac{\cos \alpha}{\cos (\phi - \alpha)} \quad 2-2$$

$$V = U \frac{\sin \alpha}{\cos (\phi - \alpha)} = U \left( \frac{t_1}{t_2} \right) \quad 2-3$$

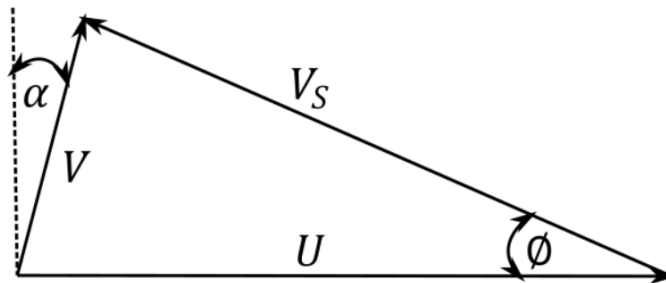


Figure 2-4. Velocity triangle at the shear zone [71]

where  $V_s$  is the shear velocity,  $V$  is the chip velocity, and  $U$  is the cutting velocity.

In this model, the chip is assumed to be under equilibrium of two equal forces and opposite in direction (i.e.,  $R$  and  $R'$ ). Where  $R$  is the exerting force from the workpiece on the chip, while  $R'$  is the applying force from the tool on the chip.

The friction coefficient  $\mu$  between the tool and the chip can be presented by equation 2-4:

$$\mu = \frac{F}{N} = \tan \lambda \quad 2-4$$

where  $F$  is the friction force (i.e., the tangential to the rake face force), while  $N$  is normal to the rake face force.

By dissolving  $R$  into two force components, the below equations can be obtained:

$$F_c = R \cos (\lambda - \alpha) \quad 2-5$$

$$F_t = R \sin (\lambda - \alpha) \quad 2-6$$

$$F = R \sin \lambda \quad 2-7$$

$$N = R \cos \lambda \quad 2-8$$

$$R = \frac{F_s}{\cos \theta} = \frac{k_{AB} t_1 W}{\sin \phi \cos \theta} \quad 2-9$$

where  $F_c$  is the cutting force,  $F_t$  is the thrust force,  $F_s$  is the shear force (i.e., force along  $AB$ ), and  $F_n$  is normal to  $AB$  force. Besides,  $\lambda$  is the friction angle,  $\theta$  is the angle between  $R$  and  $AB$  plane, and  $K_{AB}$  is the shear stress along  $AB$  plane.

Usually, the tool rake angle  $\alpha$  and the uncut chip thickness  $t_1$  are known. However, the shear flow angle  $\phi$  or the chip thickness  $t_2$  should be known in order to solve the equations and obtain cutting forces. Many studies have been done to develop a model (i.e., equation) for the shear flow angle  $\phi$ . For example, Ernest and Merchant [71] have

assumed that the plane  $AB$  is the direction of the maximum shear stress, the following equation can be found:

$$\phi = \frac{\pi}{4} + \frac{\alpha}{2} - \frac{\lambda}{2} \quad 2-10$$

Later in 1945, Merchant [66] has proved that the same equation (i.e., equation 2-10) can be found by assuming the angle  $\phi$  is adjusted to minimize the cutting work. Afterward, the shear flow  $\phi$  was modified by making the shear stress along  $AB$  depends on the normal stress to  $AB$ . The modified shear flow angle is shown in equation 2-11:

$$\phi = \frac{1}{2}(\cot^{-1}m + \alpha - \lambda) \quad 2-11$$

where  $m$  is the slope between the shear and normal stresses.

## 2.4 Lee and Shaffer Theory

The theory of plasticity was also used by Lee and Shaffer [69] in order to analyze the orthogonal cutting process. They assumed that there is no plastic deformation in the chip material at the very beginning (i.e., above the plane  $AB$ ). Figure 2-5 shows that the plane  $AB$  is connected to the chip-tool interference area by straight slip lines. The stress was assumed to be uniform in the  $ABC$  region, and the maximum shear stress occurs along the plane  $AC$ . Based on this assumption, zero stress occurs along the plane  $AB$ , which makes the angle between the plane  $AB$  and the force  $F$  to be  $\frac{\pi}{4}$ . Then, the shear flow angle  $\phi$  can be written as shown in equation 2-12:

$$\phi = \frac{\pi}{4} + \alpha - \lambda \quad 2-12$$

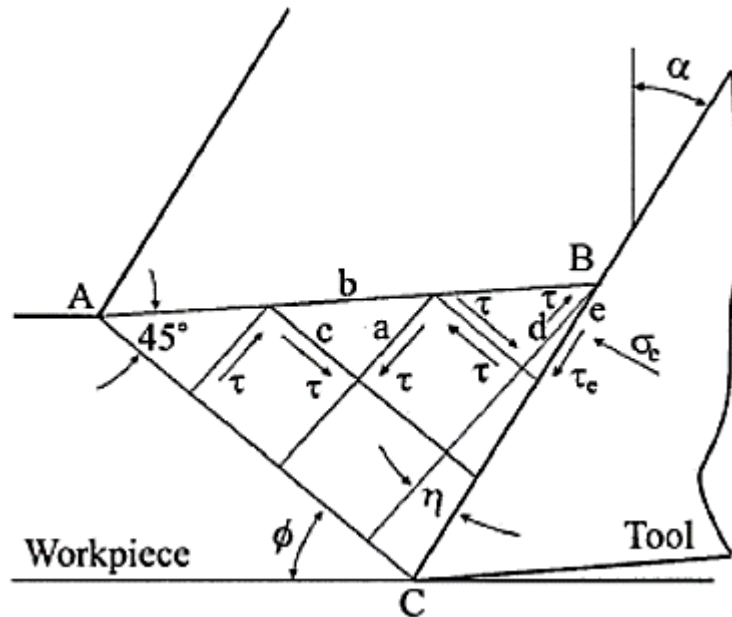


Figure 2-5. Slip line field model geometry [69]

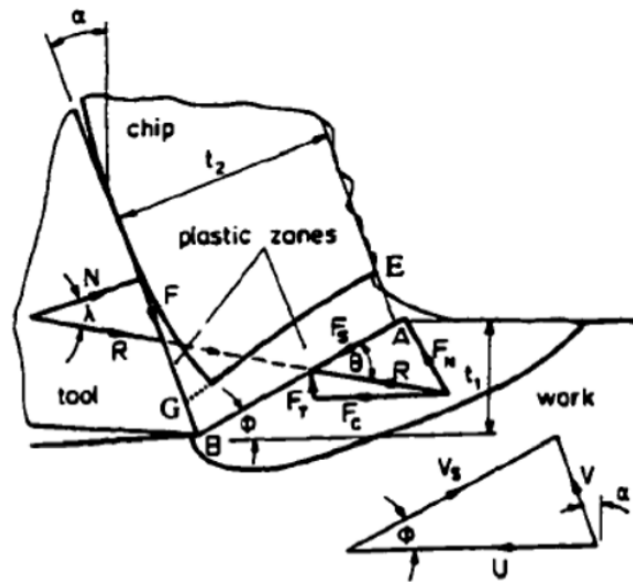
This model is not valid for all conditions. For example, when the angle  $\lambda$  is equal to  $\frac{\pi}{4}$  and the rake angle  $\alpha$  is equal to zero, the model will lead to zero shear flow angle  $\phi$ , which is not right. Therefore, the built-up edge (BUE) was included by adding the angle  $\theta$ , which depends on the BUE's size. Then the shear flow angle  $\phi$  is presented by equation 2-13 [44]:

$$\phi = \frac{\pi}{4} - (\lambda - \alpha) + \theta \quad 2-13$$

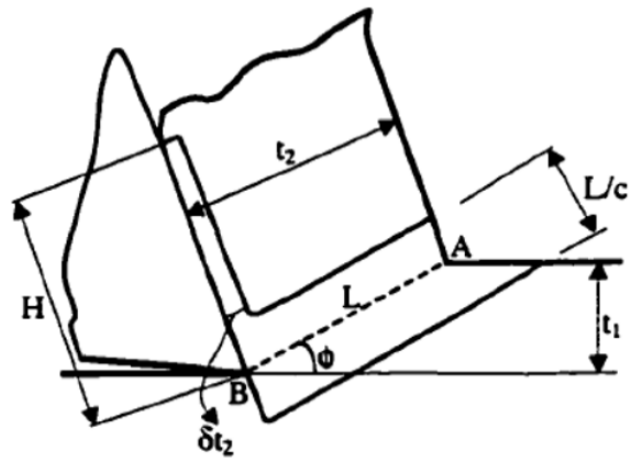
## 2.5 Oxley's Theory

In 1959 Palmer and Oxley [72] have developed their first orthogonal cutting model based on the material deformation principle. Figure 2-6 shows the geometry of Oxley's orthogonal model [64]. In the metal cutting, there are two main deformation zones; the primary shear zone, which is centered around the plane  $AB$ , and the secondary shear zone, which occurs along the tool-chip contact length. In this model, the primary shear deformation zone was assumed to have parallel sides, while the secondary deformation shear zone was considered to have a constant thickness along the contact length between the chip and the tool, as shown in Figure 2-6 (b). Oxley's model flow chart is shown in Figure 2-7. The parameter  $c$  is the ratio between the length and the thickness of the primary shear zone, while  $\delta$  is the ratio between the thickness of the secondary deformation shear zone and the chip's thickness.

Besides, the strain along the  $AB$  plane was assumed to be uniform and equal to half of the primary shear zone strain. The strain rate and the temperature were also considered to be uniform along the plane  $AB$ . The shear stress at the plane  $AB$  depends on the ratio  $c$ . Besides, the moving heat source theory [73] was used to calculate the heat partition of the workpiece and the chip. The temperature along the plane  $AB$  is iteratively calculated in order to consider the effect of the temperature variation on the thermal characteristics. The parameter  $\eta$  was used to estimate the middle shear zone's temperature by considering it as a percent of the primary deformation shear zone's temperature rise. Besides, the slip line field theory was utilized to calculate the pressure along the plane  $AB$  [74]. The pressure  $p_A$  is calculated by applying the force equilibrium on an element close to point  $A$  and located at the free surface of the workpiece. The pressure along the plane  $AB$  is estimated by applying force equilibrium at the same plane. By obtaining the shear stress and the pressure along the plane  $AB$ , the resultant force and its direction can be found .



(a)



(b)

Figure 2-6. Oxley orthogonal cutting model [64]; deformation zone (a) and simplified deformation zone (b)

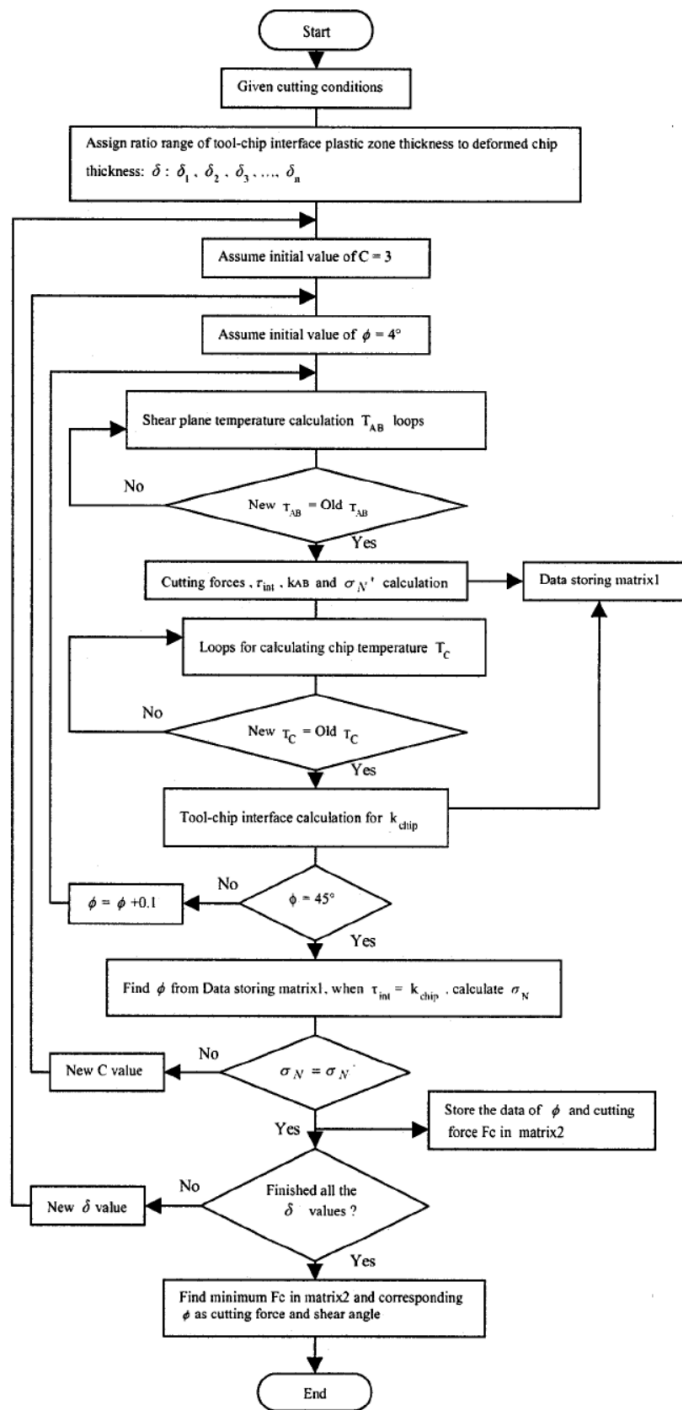


Figure 2-7. Oxley orthogonal cutting model flow chart [64]

The tool-chip contact length can be observed by assuming a uniform normal stress distribution in the secondary shear zone. Therefore, the equilibrium condition occurs as the resultant force's momentum around point  $B$  is equal to the normal force's momentum. Figure 2-8 shows the stresses and forces at the chip-tool interface. The shear and normal stresses of the rake face can be obtained by equations 2-14 and 2-15:

$$\tau_{int} = \frac{F}{Hb_1} \quad 2-14$$

$$\sigma_N = \frac{N}{Hb_1} \quad 2-15$$

where  $H$  is the chip-tool contact length, and  $b_1$  is the width of cut.

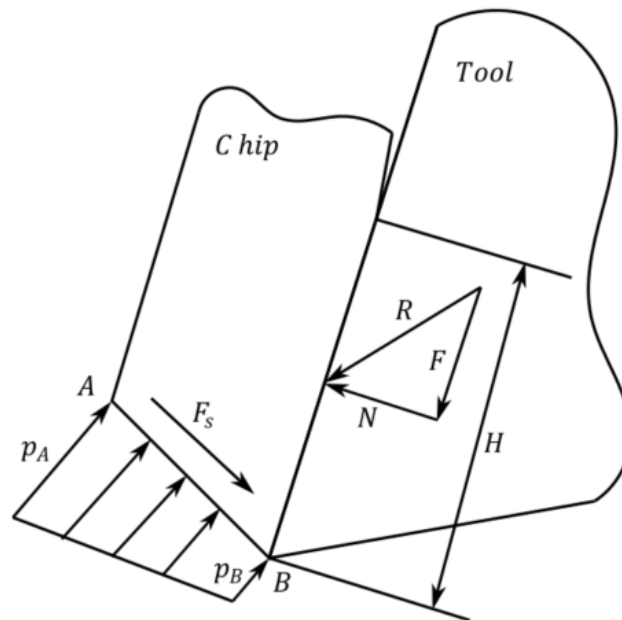


Figure 2-8. Tool-chip interface forces and stresses [64]

By assuming sticking friction at the tool-chip interface, the chip's shear stress ( $K_{chip}$ ) should be equal to  $\tau_{int}$ . Besides, The maximum tool-chip interface's temperature can be estimated based on Boothroyd's work [73]. After obtaining the maximum rise in temperature  $\Delta\theta_m$ , the parameter  $\psi$  was used to get the tool-chip interface's average. To perform the analysis, there are three unknowns should be obtained (i.e.,  $c$ ,  $\delta$ , and  $\phi$ ). Figure 2-7 shows the flow chart of the iterative approach that was used to get the solution. The shear flow angle ( $\phi$ ) is obtained when  $\tau_{int} = k_{chip}$ . The iteration operation was allowed to proceed until a very small difference between  $\sigma_N$  and  $\sigma_N'$  is achieved, then the value of  $c$  is determined. Finally, the parameter  $\delta$  is selected based on the minimum energy principle, in which  $F_c$  should be minimum. A computer-based algorithm was developed by Oxley [64] to perform the analysis. Good agreement between the experiments and the predicted results was obtained after tuning  $\eta$  and  $\psi$  parameters.

## 2.6 Extension of Oxley's theory

There are many researchers have extended Oxley's theory to use different materials models such as the Johnson-Cool model [75], the power-law model [76], and threshold model [77]. Involving such models allowed a wide range of materials to be analyzed by Oxley's theory.

Recently, simulation of the high-speed machining requires different materials characteristics to be involved in order to account for the high temperature and strain rate. Johnson-Cook model is widely used in such analysis; thus, the model constants for a large number of workpiece materials can be found in the literature. Equation 2-16 shows the Johnson-Cook material model.

$$\sigma^o = (A + B \bar{\epsilon}_{pl}^n) [1 + C \ln(\frac{\dot{\bar{\epsilon}}_{pl}}{\dot{\epsilon}_o})] [1 - \left( \frac{T - T_{ref}}{T_{melt} - T_{ref}} \right)^m] \quad 2-16$$

where  $A$ ,  $B$ ,  $C$ ,  $n$ ,  $m$  and  $\dot{\epsilon}_0$  are material constants which can be experimentally obtained at the reference temperature  $T_{ref}$ . Besides,  $\bar{\epsilon}_{pl}$  is the equivalent plastic strain, and  $\dot{\bar{\epsilon}}_{pl}$  is the equivalent plastic strain rate. While  $T$  is the temperature and  $T_{melt}$  is the melting temperature.

On the other hand, Lin et al. [78] utilized their own material model. In their model, the velocity modified temperature law was used to correlate the properties of the material to the temperature and the strain rate. Equation 2-17 presents the velocity modified temperature.

$$T_{mod} = \left( 1 - v \log_{10} \left( \frac{\dot{\epsilon}}{\dot{\epsilon}_0} \right) \right) T \quad 2-17$$

where  $T_{mod}$  is the modified temperature,  $\dot{\epsilon}$  is the equivalent strain rate, and  $\dot{\epsilon}_0$  is the reference strain rate.

It can be seen that the modified temperature increases when the temperature increases and decreases when the strain rate increases. The material flow stress is then calculated as shown in equation 2-18:

$$\sigma = \sigma_1 \epsilon^n \quad 2-18$$

where  $\sigma_1$  is the material strength coefficient and  $n$  is the material strain hardening expansion, which is a function in the modified temperature.

The forces are then calculated by finding the stresses, which are depending on the temperature, strain, and strain rate. The modified temperature law was originally developed for steel and then extended to different materials [79].

For different ranges of  $T_{mod}$ , the variables  $\sigma_1$  and  $n$  can be presented by polynomial relations. Although these equations are available for a few materials, the relations for

many engineering alloys are missing. Therefore, the usage of the Johnson-Cook material's model extends the Oxley's theory and makes it useful for many engineering alloys. For this purpose, the new variable  $n_{eq}$  was used instead of  $n$ , and accordingly the Oxley's equations were updated. The new strain hardening index  $n_{eq}$  can be estimated as shown in equation 2-19:

$$n_{eq} \approx \frac{nB\varepsilon_{AB}^n}{(A + B\varepsilon_{AB}^n)} \quad 2-19$$

where  $A$  and  $B$  are material constants. Besides,  $\varepsilon_{AB}$  is the strain at the plane  $AB$ , which is assumed to be constant.

Figure 2-9 shows the flow chart for the modified Oxley model [80]. The values of the shear angle  $\phi$ , the constant  $C_0$ , and the constant  $\delta$  need to be tuned through an iteration loop. The shear angle  $\phi$  is selected when the shear stress  $\tau_{int}$  at the tool-chip interface equals the chip material's shear stress  $K_{chip}$ . The constant  $C_0$  is selected when the tool-chip interface normal stress  $\sigma_N$  equals the normal stress  $\sigma'_N$ . Besides, the constant  $\delta$  is chosen based on the minimum cutting force condition. Figure 2-10 shows the geometry of the Oxley orthogonal cutting model.

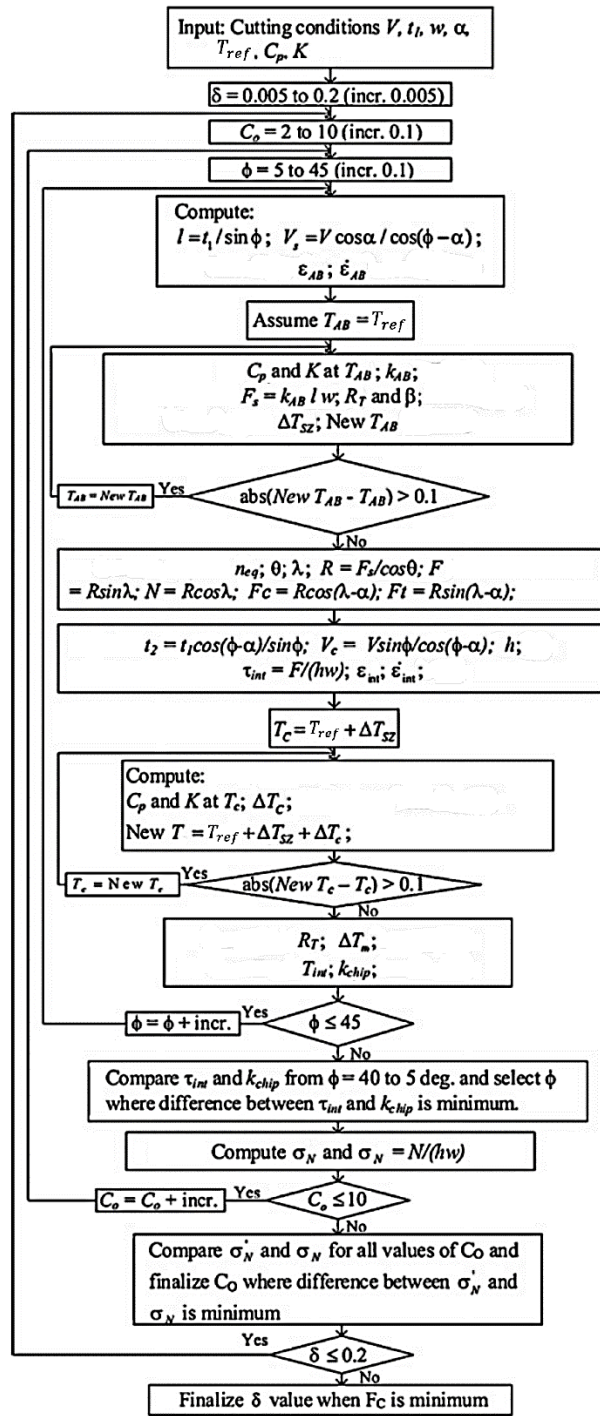


Figure 2-9. Flow chart for the modified Oxley model [80]

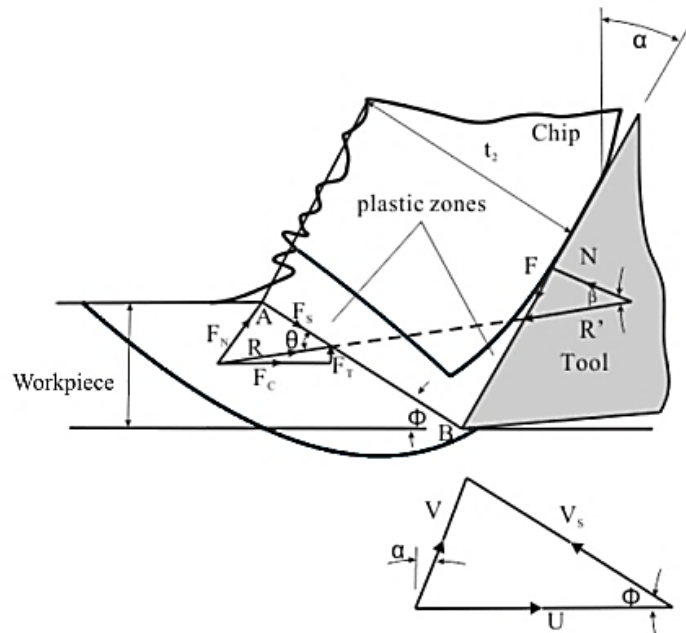


Figure 2-10. Oxley orthogonal cutting model geometry [64]

### 2.6.1 Primary shear zone relationships

The primary shear zone flow stress based on the Von-Mises yield criteria can be expressed, as shown in equation 2-20:

$$k_{AB} = \frac{\sigma_{AB}}{\sqrt{3}} = \frac{1}{\sqrt{3}} (A + B\varepsilon_{AB}^n) \left(1 + C \ln \frac{\dot{\varepsilon}_{AB}}{\varepsilon_0}\right) \left(1 - \left(\frac{T_{AB} - T_{ref}}{T_{melt} - T_{ref}}\right)^m\right) \quad 2-20$$

Where  $A$ ,  $B$ ,  $C$ , and  $m$  are material constants that can be obtained using experimental tests.  $T_{ref}$  is the reference temperature,  $T_{AB}$  is the primary shear plane temperature (which assumed to be constant), and  $T_{melt}$  is the melting temperature. Moreover,  $\dot{\varepsilon}_{AB}$  is the strain rate of the plane  $AB$ , and was assumed to be constant.

The angle  $\theta$ , which is located between the shear plane  $AB$  and the resultant force  $R$ , can be presented as shown in equation 2-21:

$$\tan \theta = 1 + 2\left(\frac{\pi}{4} - \phi\right) - C_o n_{eq} \quad 2-21$$

where  $\phi$  is the shear flow angle and  $C_o$  is the ratio between the length of the shear plane (i.e., plane  $AB$ ) to the primary shear zone thickness.

The shear flow angle can also be found, as shown in equation 2-22:

$$\theta = \phi + \lambda - \alpha \quad 2-22$$

Since the plane  $AB$  is assumed to be in the middle of the primary shear zone, thus its average shear strain ( $\gamma_{AB}$ ) is equal to half of the primary shear strain and can be expressed, as shown in equation 2-23:

$$\gamma_{AB} = \frac{1}{2} \frac{\cos \alpha}{\sin \phi \cos (\phi - \alpha)} \quad 2-23$$

The plane  $AB$  average strain rate  $\dot{\gamma}_{AB}$  is given by equation 2-24:

$$\dot{\gamma}_{AB} = \frac{C_o V_s}{l} \quad 2-24$$

where  $V_s$  is the shear flow velocity and  $l$  is the plane  $AB$  length.

Based on Von-Mises criteria, the plane  $AB$  equivalent strain  $\epsilon_{AB}$  and equivalent strain rate  $\dot{\epsilon}_{AB}$  can be obtained as shown in equation 2-25 and equation 2-26:

$$\varepsilon_{AB} = \frac{\gamma_{AB}}{\sqrt{3}} \quad 2-25$$

$$\dot{\varepsilon}_{AB} = \frac{\dot{\gamma}_{AB}}{\sqrt{3}} \quad 2-26$$

The plane  $T_{AB}$  is the average temperature, which can be written as shown in equation 2-27:

$$T_{AB} = T_{ref} + \eta \Delta T_{SZ} \quad 2-27$$

where  $T_{ref}$  is the reference temperature, which can be considered as the room temperature. Besides,  $\eta$  was used to scale the amount of the deformation energy which converts to heat and is usually assumed to be 0.9. In other words, 90% of the deformation energy converts to heat and increases the primary shear zone temperature. The remaining percent was assumed to be carried away by the chip. The primary shear zone temperature rise  $\Delta T_{SZ}$  can be estimated using the plastic work of the shear zone. Since the plastic work was assumed to be equal to the shear force  $F_s$  multiplies by the shear flow velocity  $V_s$ , the plane  $AB$  temperature rise can be found, as shown in equation 2-28:

$$\Delta T_{SZ} = \frac{(1 - \beta)F_s V_s}{m_{chip} C_p} \quad 2-28$$

where  $m_{chip}$  is the chip load, which can be given by equation 2-29:

$$m_{chip} = \rho V t_1 w \quad 2-29$$

Besides,  $\beta$  is the percentage of the heat which moves from the primary shear zone to the workpiece, and can be expressed by equation 2-30:

$$\beta = 0.5 - 0.35 \log_{10}(R_T \tan \phi) \text{ for } 0.04 \leq R_T \tan \phi \leq 10$$

$$\beta = 0.3 - 0.15 \log_{10}(R_T \tan \phi) \text{ for } R_T \tan \phi > 10$$
2-30

where  $R_T$  is a dimensionless thermal number, and can be given as shown in equation 2-31:

$$R_T = \frac{\rho C_p V t_1}{K}$$
2-31

where  $\rho$  is the density,  $C_p$  is the specific heat,  $V$  is the cutting velocity,  $t_1$  is the uncut chip thickness, and  $K$  is the thermal conductivity.

Finally, the point  $B$  normal stress  $\sigma'_N$  (i.e., at the tool tip) can be expressed by equation 2-32:

$$\sigma'_N = k_{AB} \left( 1 + \frac{\pi}{2} - 2\alpha - 2C_o n_{eq} \right)$$
2-32

## 2.6.2 Secondary shear zone relationships

The secondary shear zone is assumed to be rectangular. Besides,  $\delta$  is the ratio between the thickness of the secondary shear zone to the deformed chip thickness  $t_2$ . Thus, the average thickness of the secondary shear zone is equal to  $\delta * t_2$ .

Therefore, the equivalent strain-rate in the secondary shear zone  $\epsilon_{int}$  can be expressed by equation 2-33:

$$\varepsilon_{int} = \frac{\gamma_{int}}{\sqrt{3}} = \frac{1}{\sqrt{3}} \frac{V_c}{\delta t_2} \quad 2-33$$

The length of the secondary shear zone was assumed to be equal to the contact length  $h$ . This contact length can be obtained by applying the normal stresses momentum balance around point  $B$ , and can be found as shown in equation 2-34:

$$h = \frac{t_1 \sin \theta}{\cos \lambda \sin \phi} \left( 1 + \frac{C_0 n_{eq}}{3(1 + 2(\frac{\pi}{4} - \phi) - C_0 n_{eq})} \right) \quad 2-34$$

The normal stress at the interface between the chip and the tool was assumed to be uniform. Thus, the normal stress at the point  $B$  can be presented as shown in equation 2-35:

$$\sigma_N = \frac{N}{hw} \quad 2-35$$

where  $N$  is the normal force at the tool-chip interface, and  $w$  is the chip width.

The temperature of the tool-chip interface can be given, as shown in equation 2-36:

$$T_{int} = T_{ref} + \Delta T_{SZ} + \psi \Delta T_M \quad 2-36$$

where  $T_{ref}$  is the room temperature and  $\Delta T_M$  is the temperature rise of the deformed chip. The constant  $\psi$  is used to scale the temperature rise in order to get an average temperature rise. Boothroyd [81] has developed an equation to find the temperature rise of a rectangular heat source:

$$\log_{10}\left(\frac{\Delta T_M}{\Delta T_c}\right) = 0.06 - 0.195(\delta) \sqrt{\frac{R_T t_2}{t_1}} + 0.5 \log_{10}\left(\frac{R_T t_2}{h}\right) \quad 2-37$$

where  $\Delta T_c$  is the average chip temperature rise, and can be found as shown in equation 2-38:

$$\Delta T_c = \frac{F V_c}{m_{chip} C_p} \quad 2-38$$

According to Mathew et al., the maximum shear strain in the secondary shear zone can be calculated by equation 2-39:

$$\gamma_{jnt} = 2\gamma_{AB} + 0.5\gamma_M \quad 2-39$$

The maximum shear strain in the secondary shear zone can be expressed by equation 2-40:

$$\gamma_M = \frac{h}{(\delta t_2)} \quad 2-40$$

Thus, the equivalent strain in the secondary shear zone can be obtained as shown in equation 2-41:

$$\varepsilon_{int} = \frac{\gamma_{int}}{\sqrt{3}} = \left(\frac{1}{\sqrt{3}}\right)(2\gamma_{AB} + 0.5\gamma_M) \quad 2-41$$

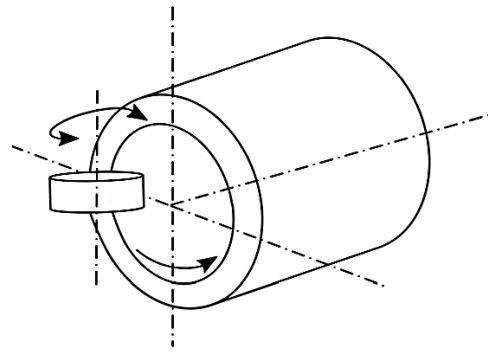
Finally, the flow stress at the interface between the tool and the chip can be found by equation 2-42:

$$k_{chip} = \frac{1}{\sqrt{3}} (A + B \varepsilon_{int}^n) (1 + C \ln \frac{\varepsilon_{int}}{\varepsilon_o}) (1 - (\frac{T_{int} - T_{ref}}{T_{melt} - T_{ref}})^m) \quad 2-42$$

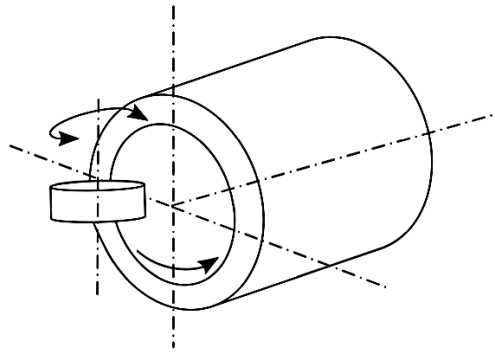
## 2.7 Armarego's rotary tools: fundamental study

In the early 1990s, Armarego et al. [56-58] developed a fundamental explanation of the machining using rotary tools. In their research, the tool rotational speed was considered in the analysis process by developing the equivalent cutting concept. An equivalent orthogonal cutting model was used for the self-propelled cutting tools, while an equivalent oblique model was employed for the driven rotary tools. They verified their models by comparing the predicted results to the experimentally obtained results.

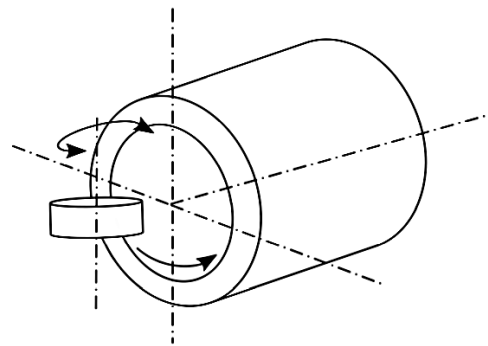
The cutting process by rotary tools is more complex compared to conventional cutting. That is because the tool itself rotates around its axis, which impacts the machining temperature, friction at the tool-chip interface, and the chip formation mechanism. To study the cutting process using rotary tools, a tube-end turning process was selected to simplify the analysis. In Figure 2-11a and Figure 2-11b, the machining process must be actively driven to control the tool rotational direction (i.e., clockwise or counter-clockwise). On the other hand, the cutting process in Figure 2-11c can be actively driven or self-propelled. In this specific case, if the rotary tool is actively driven, then the tool can rotate in either clockwise or counter-clockwise direction with any desired speed. However, if it is a self-propelled cutting process, the tool has to rotate in the counter-clockwise direction. The tool rotational speed will depend on the cutting velocity and the distance between the tool and the center of the workpiece.



(a)



(b)



(c)

Figure 2-11. Rotary tools tube-end turning [57]; tool above the workpiece center (a), tool in the same level of the workpiece center (b), and tool below the workpiece center (c)

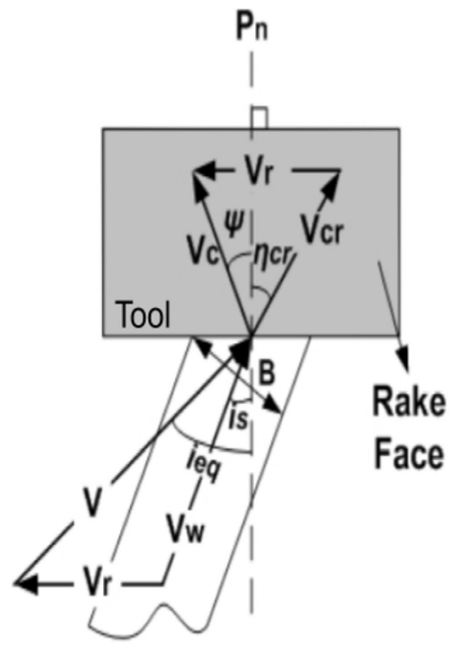
The following assumptions were considered to analyze the machining process using rotary tools [57]:

- The ratio between the tube diameter and the insert diameter to the tube thickness is large enough to neglect the tool's curvature
- The orientation between the cutting speed and the insert's normal plane depends on the tool location (i.e., above or below the workpiece axis)
- The variation in the cutting velocity is neglected since the tube thickness is small
- The cutting velocity is large enough to neglect the feed velocity

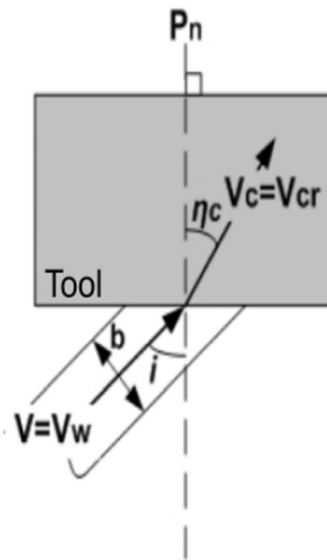
As mentioned before, the equivalent oblique cutting model is used to simulate the cutting process using the driven rotary tools. In the driven rotary tools, the tool rotates by an external power source. This external source could be the CNC machine tool's shaft or motor mounted on the tool holder.

The main difference between the rotary tools and the traditional cutting tools is the tool motion. At constant cutting velocity  $V_w$ , the tool motion only modifies the magnitude and the direction of the relative cutting speed  $V$ .

Unlike the self-propelled rotary tools, the tool speed of the driven rotary tools does not depend on the cutting speed and the inclination angle. Therefore, the tool rotational speed and the inclination angle can be adjusted to any required value, which cannot occur in the SPRT.



(a)

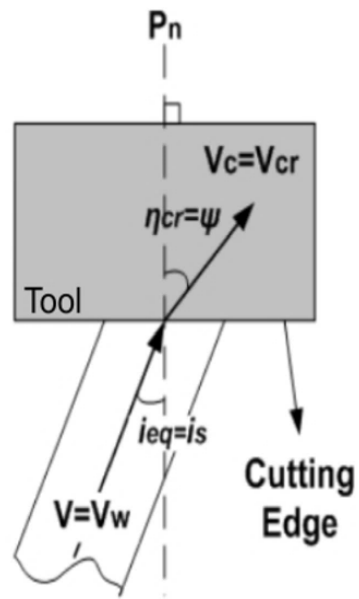


(b)

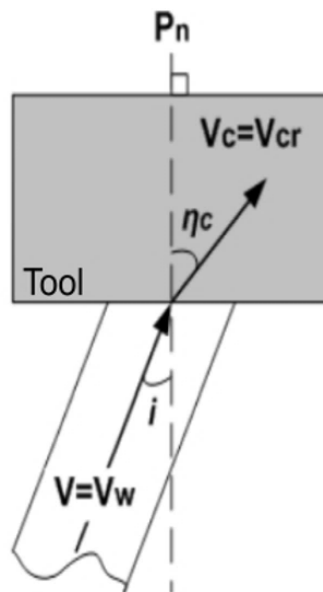
Figure 2-12. An actively driven rotary tool [57]; an oblique case (a) and its equivalent classical process (b)

Figure 2-12 shows an actively driven rotary tool case in which the tool is located above the workpiece axis. In Figure 2-12,  $P_n$  is the normal plane,  $V_W$  is the cutting speed,  $V$  is the relative cutting speed, and  $V_r$  is the tool velocity. While,  $V_{cr}$  is the relative chip flow velocity,  $V_c$  is the absolute chip flow velocity,  $i_s$  is the static inclination angle, and  $i$  is the equivalent inclination angle. Besides,  $\eta_c$  is the chip flow angle,  $\eta_{cr}$  is the relative chip flow angle, and  $\psi$  is the absolute chip flow angle. The cutting speed  $V_W$  inclines to the normal plane  $P_n$  with angle  $i_s$ . Based on the tool speed direction, the tool rotates in the clockwise direction, while the workpiece rotates in the counter-clockwise direction. Using the tool velocity  $V_r$  and the cutting speed  $V_W$ , the relative cutting velocity  $V$  can be obtained. As can be seen, the process becomes oblique cutting; in other words, the angle  $i$  between the relative cutting velocity  $V$  and the normal plane  $P_n$  is larger than the angle  $i_s$ . Although, the relative chip flow angle  $\eta_{cr}$  is in the right side of the normal plane  $P_n$ , the observer can notice that the absolute chip flow direction  $\psi$  is in the other direction, which occurs due to the direction of the tool velocity  $V_r$ . Figure 2-12 a shows the equivalent classic oblique cutting process for this case.

Figure 2-13 shows a fixed tool case, where tool rotational velocity  $V_r$  is equal to zero. Thus, there is no change in the cutting velocity  $V_W$  or in the chip flow velocity  $V_c$ . This process is identical to a regular oblique cutting process, as seen in Figure 2-13 b.

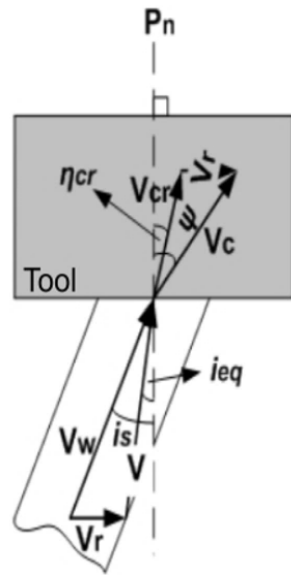


(a)

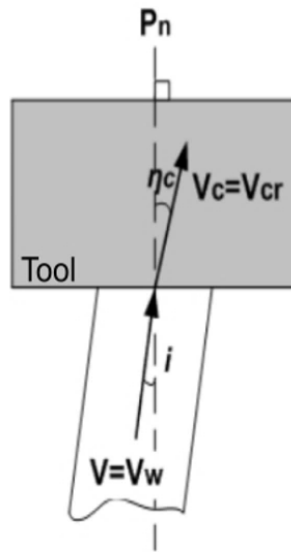


(b)

Figure 2-13. Stationary rotary tool [57]; an oblique case (a) and its equivalent classical process (b)



(a)



(b)

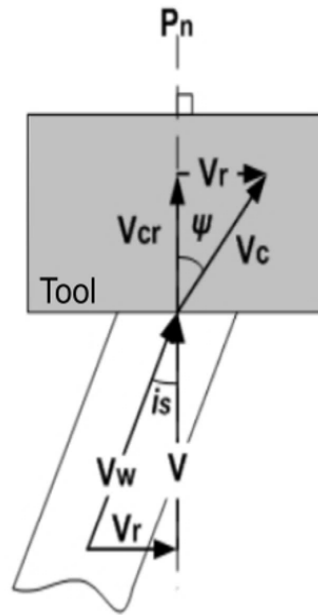
Figure 2-14. An actively driven rotary tool [57]; an oblique case (a) and its equivalent classical process (b)

Figure 2-14 shows an actively driven rotary tool case, in which the tool is located above the workpiece axis. Therefore, the cutting speed  $V_w$  inclines to the normal plane  $P_n$

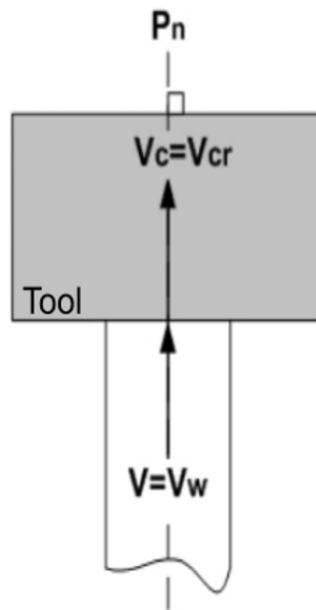
with an angle  $i_s$ . In this case, the tool rotates in the counter-clockwise direction. The tool speed  $V_r$  reduces the cutting speed  $V_W$ , thus the relative cutting speed  $V$  and its direction  $i_{eq}$  are smaller than the cutting speed  $V_W$  and the angle  $i_s$ , respectively. Besides, the relative chip flow velocity  $V_{cr}$  is lower than the absolute chip flow velocity  $V_c$ , and both of them are in the right side of the normal plane  $P_n$ .

Similarly, Figure 2-15 shows the specific case of actively driven rotary tools. In this case, the tool rotational speed  $V_r$  is selected in order to minimize the relative cutting speed  $V$ . The minimum relative cutting speed  $V$  occurs when the relative inclination angle  $i_{eq}$  is equal to zero. On the other hand, the relative chip flow angle is equal to zero, while the relative chip velocity reaches the minimum. Accordingly, the equivalent orthogonal cutting process was used to simulate this case, as shown in Figure 2-15 b.

Finally, Figure 2-16 shows a case of the actively driven rotary tool, in which the tool rotational speed  $V_r$  is larger than the previous case. As a result, the direction of the relative cutting speed  $V$  was changed. Besides, the relative chip flow velocity  $V_{cr}$  was changed as well, while the tool rotational direction and the absolute chip flow direction were the same. Moreover, it can be seen that the equivalent inclination angle  $i_{eq}$  and the relative chip flow angle  $\eta_{cr}$  were flipped. The equivalent oblique cutting process was used to model the current case, as shown in Figure 2-16 b.

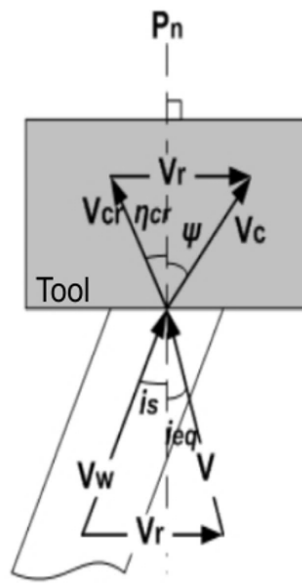


(a)

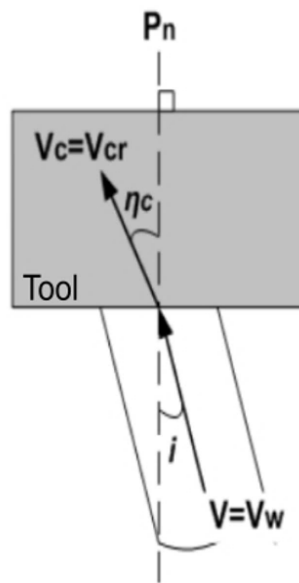


(b)

Figure 2-15. An actively driven rotary tool [57]; an oblique case (a) and its equivalent classical process (b)



(a)



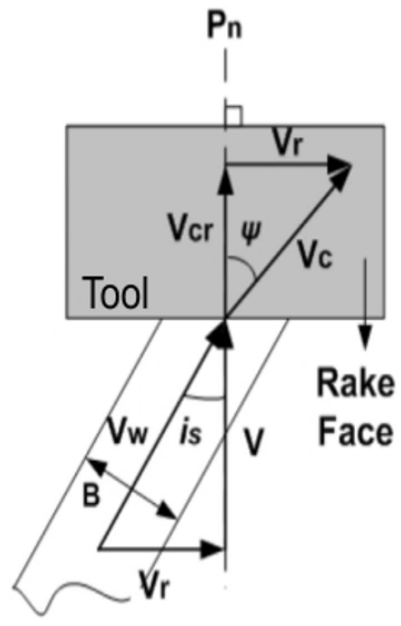
(b)

Figure 2-16. An actively driven rotary tool [57]; an oblique case (a) and its equivalent classical process (b)

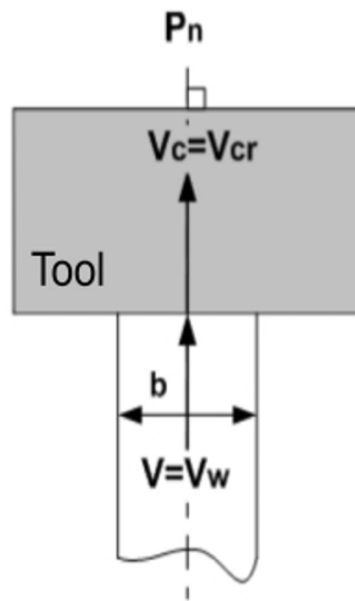
For the self-propelled rotary tool, the tools are allowed to freely rotate around its own axis. The inclination angle between the workpiece and the insert causes the generated chip to flow at an angle  $\eta_c$ . As a result, the friction force at the tool-chip interface inclines to the normal plane  $P_n$  with the same angle  $\eta_c$ . This force can be decomposed into two components; the tangential component and the normal component. Since the tool is allowed to freely rotate, the tangential component will be able to guide the insert to rotate. This is the reason behind calling it self-propelled rotary tools.

In Figure 2-17, the tool was positioned above the workpiece axis. Therefore, the cutting velocity  $V_w$  makes angle  $i_s$  with the normal plane  $P_n$ . As mentioned before, the tangential component of the friction force guides the tool to rotate. The tool accelerates in the same direction of the tangential force component until it balances with the bearing friction force. At this time, the tool reaches its equilibrium velocity  $V_r$ . In order to simplify the analysis, the bearing friction was ignored, and the tool reaches its maximum speed  $V_r$ , at which the relative cutting velocity  $V$  makes zero angle with the normal plane  $P_n$ . Besides, the relative chip flow velocity  $V_{cr}$  is in the direction of  $P_n$  (i.e., the relative chip flow angle  $\eta_{cr}$  is equal to zero). Thus, the equivalent orthogonal cutting process was used to model the current case, as shown in Figure 2-17b.

Similarly, Figure 2-18 shows the self-propelled rotary tool in which the tool was positioned below the workpiece axis (see Figure 2-11). In this case, the chip makes an angle  $\psi$  to the right side with the normal plane  $P_n$ . The tangential force component guides the tool to rotate and accelerate until the tool velocity  $V_r$  reaches its steady state value. As can be seen, the relative cutting velocity  $V$  and the relative chip flow velocity  $V_{cr}$  are in the same direction of the normal plane  $P_n$ . In other words, the equivalent inclination angle  $i_{eq}$  and the relative chip flow angle  $\eta_{cr}$  are equal to zero. Therefore, the equivalent orthogonal cutting force was also utilized to simulate this case, as shown in Figure 2-18 b. It is important to notice that the tool velocity  $V_r$  depends on the static inclination angle  $i_s$  and the cutting speed  $V_w$ .

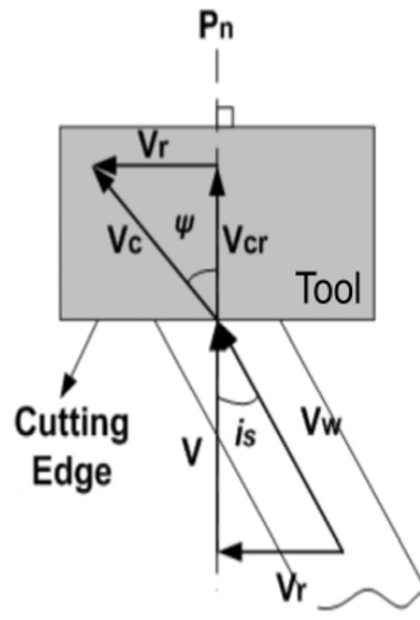


(a)

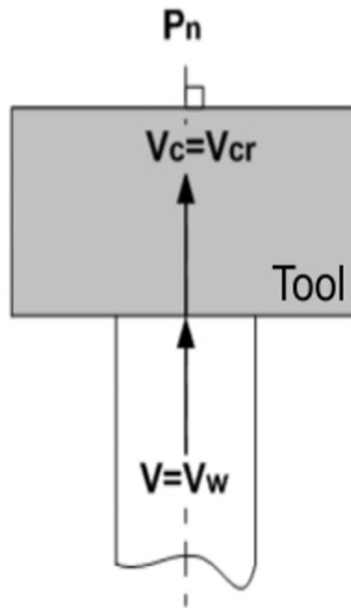


(b)

Figure 2-17. Self-propelled rotary tool [57]; tool positioned above the workpiece center (a) and its equivalent classical process (b)



(a)



(b)

Figure 2-18. Self-propelled rotary tool [57]; tool positioned below the workpiece center (a) and its equivalent classical process (b)

## 2.8 Important relationships for machining with rotary tools

To analyze the machining process using rotary tools, some important velocities, geometry, and forces relations should be obtained. Figure 2-19 shows a geometry for velocities and angles of rotary tools.

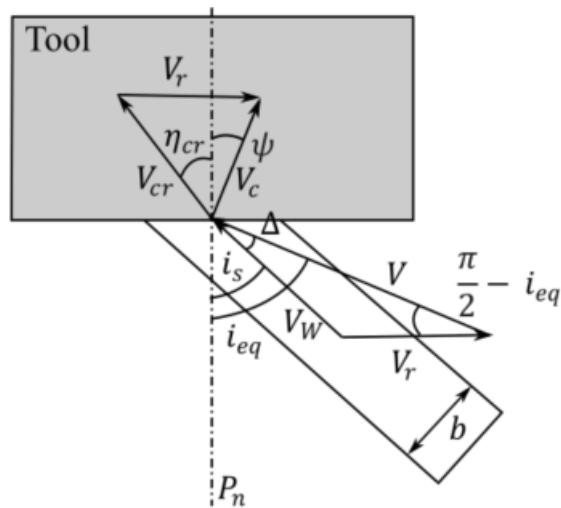


Figure 2-19. Rotary tools velocities

According to Figure 2-19, the cutting speed  $V_w$  can be found, as shown in equation 2-43:

$$V_w = V_r + V \quad 2-43$$

Similarly, the chip flow velocity  $V_c$  can be obtained, as shown in equation 2-44:

$$V_c = V_r + V_{cr} \quad 2-44$$

The relative cutting velocity can be expressed, as shown in equation 2-45:

$$V = \sqrt{(V_w \cos i_s)^2 + (V_r + V_w \sin i_s)^2} \quad 2-45$$

The equivalent inclination angle can be obtained, as shown in equation 2-46:

$$\tan i_{eq} = \frac{V_r + V_w \sin i_s}{V_w \cos i_s} \quad 2-46$$

More relations can be found, as shown below:

$$\Delta = i_{eq} - i_s \quad 2-47$$

$$\frac{V_w}{\sin(\frac{\pi}{2} - i_{eq})} = \frac{V}{\sin(\pi - (\frac{\pi}{2} - i_{eq}) - \Delta)} \quad 2-48$$

$$V_w * \cos i_s = V * \cos i_{eq} \quad 2-49$$

$$\frac{V_r}{\sin(i_{eq} - i_s)} = \frac{V}{\sin(90 + i_s)} = \frac{V}{\cos i_s} \quad 2-50$$

Since the material removal rate is constant, the equivalent depth of cut can be expressed, as shown in equation 2-52:

$$V_W * B * t = V * b * t = V * B * \frac{\cos i_{eq}}{\cos i_s} * t \quad 2-51$$

$$b = B * \frac{\cos i_{eq}}{\cos i_s} \quad 2-52$$

where  $B$  is the width of the cut,  $b$  is the width of the cut in the equivalent coordinate system, and  $t$  is the unreformed chip thickness.

The relations between the absolute and relative chip width can be presented as shown below:

$$\frac{b}{\cos i_s} = \frac{B_c}{\cos \psi} = \frac{B_{cr}}{\cos \eta_c} \quad 2-53$$

$$B_c = b \frac{\cos \psi}{\cos i_s} \quad 2-54$$

$$B_{cr} = b \frac{\cos \eta_c}{\cos i_s} \quad 2-55$$

$$B_{cr} = B_c \frac{\cos \eta_c}{\cos \psi} \quad 2-56$$

where  $B_c$  is the chip width and  $B_{cr}$  is the relative chip width.

Again, since the material removal rate is constant, equation 2-57 can be provided:

$$V_c B_c t_c = V_w b t = V_{cr} B_{cr} t_{cr} = V B t \quad 2-57$$

Since  $t_c = t_{cr}$ ; thus, equation 2-58 can be found:

$$r_l = \frac{V_c}{V_w} = \frac{l_c}{l} \quad 2-58$$

where  $r_l$  is the chip length ratio,  $l_c$  is the length of the chip in the direction of the chip velocity, and  $l$  is the cut length of the workpiece in the direction of the cutting velocity  $V_w$ .

The ratio of the chip thickness  $r_c$  can be presented, as shown in equation 2-59:

$$r_c = r_l * \frac{\cos \psi}{\cos i_s} \quad 2-59$$

According to Shaw et al. [13], the rake angle  $\alpha_e$  in the equivalent oblique coordinate system can be expressed by equation 2-60:

$$\sin \alpha_e = \sin \eta_{cr} * \sin i_{eq} + \cos \eta_{cr} * \cos i_{eq} * \sin \alpha_n \quad 2-60$$

where  $\alpha_n$  is the normal rake angle.

The normal shear angle  $\phi_n$  can be presented, as shown in equation 2-61:

$$\tan (\phi_n) = \frac{r_c * \cos \alpha_n}{1 - r_c * \sin \alpha_n} = \frac{r_l * \left(\frac{\cos \psi}{\cos i_s}\right) * \cos \alpha_n}{1 - r_l * \left(\frac{\cos \psi}{\cos i_s}\right) * \sin \alpha_n} \quad 2-61$$

The equivalent shear angle  $\phi_e$  in the equivalent oblique coordinate system can be found as shown below:

$$\tan (\phi_e) = \frac{\frac{V_{cr}}{V} \cos \alpha_e}{1 - \frac{V_{cr}}{V} \sin \alpha_e} \quad 2-62$$

$$\sin (\phi_e) = \frac{\cos \eta_s * \cos \alpha_e}{\cos \eta_{cr} * \cos \alpha_n} * \sin (\phi_n) \quad 2-63$$

After applying some geometrical relations, the relative chip flow angle  $\eta_{cr}$  can be expressed by equation 2-64:

$$\tan \eta_{cr} = \frac{\sin (i_{eq} - i_s)}{r_t * \cos i_{eq} * \cos i_s} - \tan \psi \quad 2-64$$

where  $r_t$  is the ratio between the undeformed chip thickness  $t$  to the deformed chip thickness  $t_c$ .

The velocity vectors in the Cartesian coordinates system can be found as shown below:

$$V = \begin{bmatrix} V \cos i_{eq} \\ V \sin i_{eq} \\ 0 \end{bmatrix} \quad 2-65$$

$$V_{cr} = \begin{bmatrix} V_{cr} \cos \eta_{cr} \sin \alpha_n \\ V_{cr} \sin \eta_{cr} \\ V_{cr} \cos \eta_{cr} \cos \alpha_n \end{bmatrix} \quad 2-66$$

$$V_s = \begin{bmatrix} -V_s \cos \eta_s \cos \phi_n \\ -V_s \sin \eta_s \\ V_s \cos \eta_s \sin \phi_n \end{bmatrix} \quad 2-67$$

where  $V_s$  is the shear flow velocity and  $\eta_s$  is the rake face angle in the shear plane direction.

Since the relative cutting velocity  $V$ , the relative chip velocity  $V_{cr}$ , and the shear flow velocity  $V_s$  are in balance, the below relations can be demonstrated:

$$\frac{V_{cr}}{V} = \frac{\sin \phi_n \cos i_{eq}}{\cos (\phi_n - \alpha_n) \cos \eta_{cr}} \quad 2-68$$

$$\frac{V_s}{V} = \frac{\cos i_{eq} \cos \alpha_n}{\cos \eta_s \cos (\phi_n - \alpha_n)} \quad 2-69$$

## 2.9 Prediction of the chip flow angle

According to Colwell [82], the chip flow angle was shown to be depending on the cutting forces. As a result of the chip flow at the tool-chip interface, two components of the force are generated. The first force component is the friction force, which affects the rake face of the tool. This force has the same angle as the chip itself (i.e., tangents to the chip). The other force component is the normal force, which is normal to the rake face of the tool. As the second force component is normal to the chip, it does not have a contribution toward the chip flow angle. Therefore, the chip flow angle depends only on the friction force.

Usually, the chip does not have a uniform cross-section area, which means the friction force is not uniformly distributed over the chip area. Thus, the chip is considered as segment elements. The thickness and orientation of each element are not the same. As a result, the friction force component magnitude and direction for each chip's element are different. The total friction force can be obtained by getting the summation of the friction force components in all the elements. The chip flow angle coincides with the friction force angle.

According to Young et al. [83], the friction force per unit area of the chip is assumed to be constant for each material. This constant is called the friction force intensity  $u$ . In

each element, the magnitude of the friction force  $|dF|$  is expressed as shown in equation 2-70:

$$|dF| = u dA \quad 2-70$$

where  $dA$  is the area of the chip element and can be given as shown in equation 2-71:

$$dA = t(s) ds \quad 2-71$$

where  $ds$  is the element's width, while  $t(s)$  is the thickness of the element.

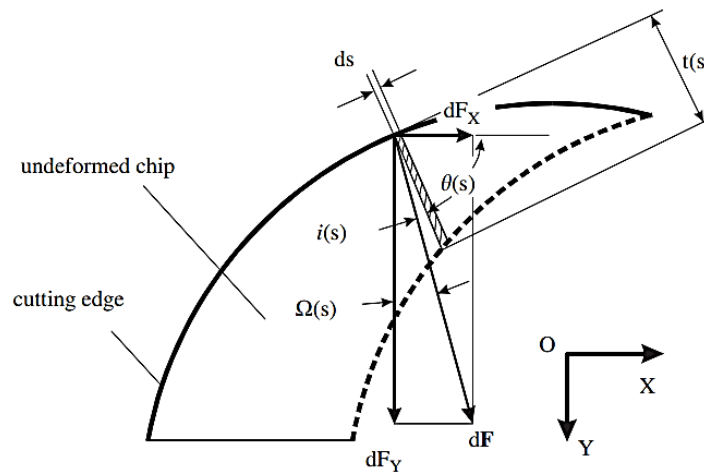


Figure 2-20. The geometry of the chip area at the nose radius cutting edge [83]

Figure 2-20 shows the geometry of the chip area in round insert cases [83]. The angle between each chip element vector and the friction force is denoted by  $i(s)$ . The friction force vector in each element can be dissolved into two components in the Cartesian coordinates system. Besides,  $\theta$  is the angle between the chip element vector and the x-direction, while  $\Omega$  is the angle between the friction force vector and the y-direction, and can be presented by equation 2-72:

$$\Omega(s) = \frac{\pi}{2} - i(s) - \theta(s) \quad 2-72$$

To get the total friction force  $F$ , integration is utilized to obtain the summation of the friction force components in all chip elements as shown below:

$$F = F_x i + F_y j$$

$$F = \left( \int dF_x \right) i + \left( \int dF_y \right) j \quad 2-73$$

$$F = \left( \int |dF| \sin \Omega \right) i + \left( \int |dF| \cos \Omega \right) j$$

where  $i$  is the x-direction unit vector, while  $j$  is the y-direction unit vector.

By substituting  $|dF| = u dA$ , the friction force  $F$  can be written as shown in equation 2-74:

$$F = \left( u \int \sin \Omega dA \right) i + \left( u \int \cos \Omega dA \right) j \quad 2-74$$

The chip flow angle coincides with the friction force angle and can be calculated as shown in equation 2-76:

$$\bar{\Omega} = \tan^{-1} \left( \frac{F_x}{F_y} \right) \quad 2-75$$

$$\bar{\Omega} = \tan^{-1} \left( \frac{\int \sin \Omega dA}{\int \cos \Omega dA} \right) \quad 2-76$$

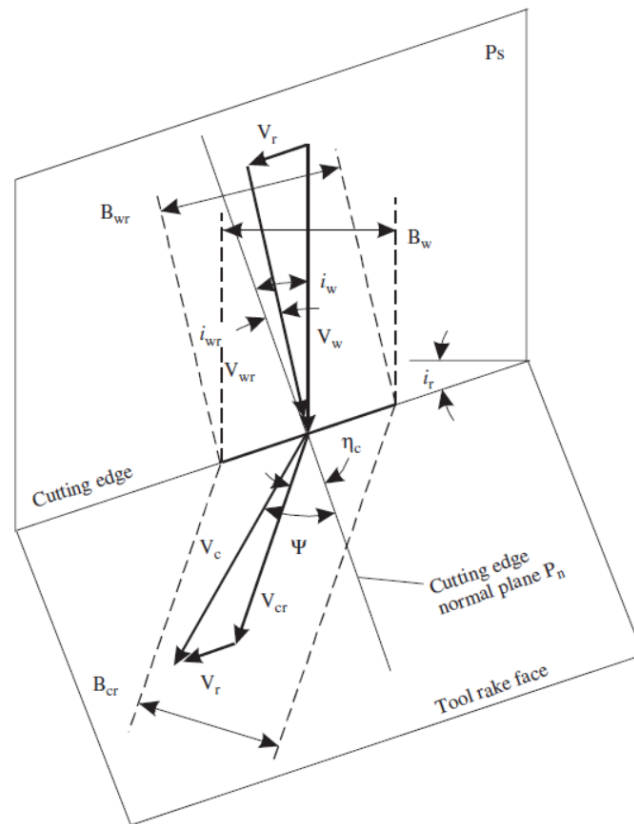


Figure 2-21. Velocity vectors and chip widths for machining using self-propelled rotary tools [84]

Kishawy et al. [84] have extended this model to include the tool motion of the self-propelled rotary tools. The below assumptions were considered in their model:

- The insert diameter is large enough to assume that the cutting edge is straight
- The chip velocity is uniform along the chip width
- The formed chip is assumed to be continuous
- The chip flow angle coincides with the friction force angle
- There is no chip side flow

Figure 2-21 shows the velocity vectors and chip widths in machining using self-propelled rotary tools.  $i_r$  is the tool equivalent inclination angle and  $i_w$  is the inclination angle between the tool and the workpiece, while  $i_{wr}$  is the relative cutting

velocity angle. Besides,  $\eta_c$  is the relative chip flow angle and  $\Psi$  is the absolute chip flow angle. The following velocity relations can be found:

$$V_W = V_{Wr} + V_r \quad 2-77$$

$$V_c = V_{cr} + V_r \quad 2-78$$

where  $V_w$  is the cutting velocity,  $V_r$  is the tool velocity, and  $V_{wr}$  is the relevant cutting velocity. On the other hand,  $V_c$  is the chip velocity and  $V_{cr}$  is the relative chip velocity.

The following relations can be obtained from Figure 2-21:

$$i_w = i_r \quad 2-79$$

$$B_x = \frac{B_w}{\cos i_w} \quad 2-80$$

$$B_{Wr} = \frac{B_w \cos i_{Wr}}{\cos i_w} = \frac{B_w \cos i_{Wr}}{\cos i_r} \quad 2-81$$

$$\tan i_{Wr} = \frac{V_w \sin i_w - V_r}{V_w \cos i_w} \quad 2-82$$

where  $B_w$  is the cutting width, while  $B_x$  is the engaged width in the cutting edge direction.

Figure 2-22 shows the geometry of the chip on the tool rake face. In order to calculate the chip flow angle on the tool rake face, a transformation for the machining coordinate system should be utilized to have a new coordinate system tangents the rake face. The area RCEV indicates the chip area. This area is splitted into four different smaller areas: RMNS, MCKN, RSV, and CEK.

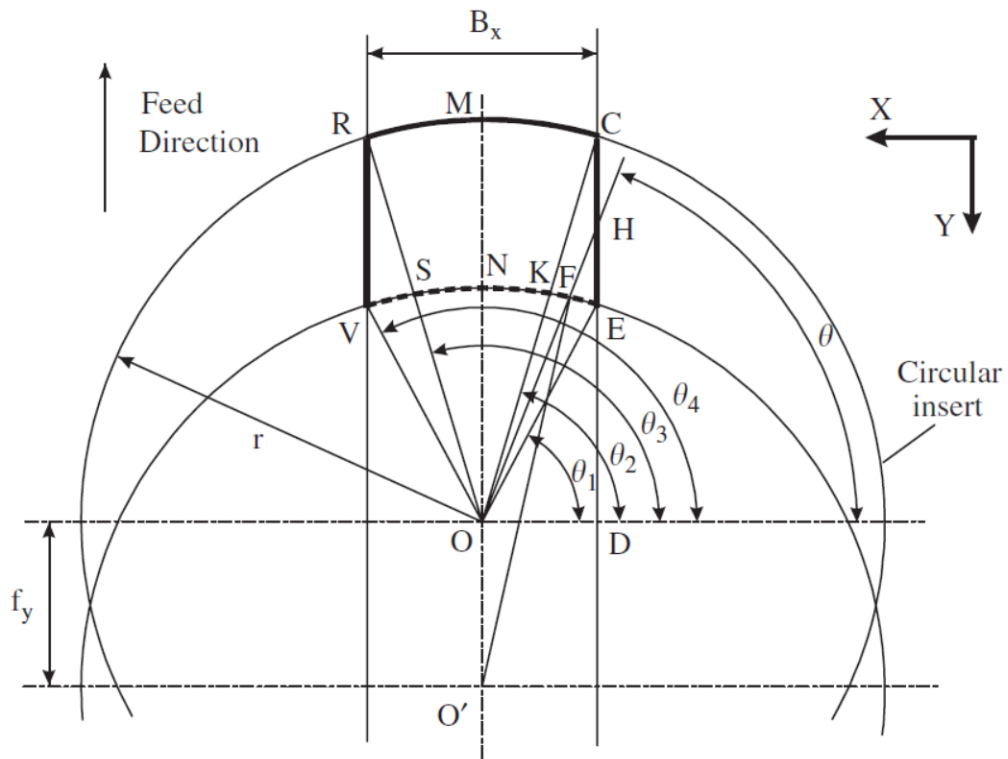


Figure 2-22. The geometry of the chip flow angle calculation [84]

These areas are bounded by angles  $\theta_1$ ,  $\theta_2$ ,  $\theta_3$ , and  $\theta_4$ , which can be expressed as shown below:

$$\theta_1 = \tan^{-1} \left( \frac{r \sin \theta_2 - f_y}{\frac{B_x}{2}} \right) \quad 2-83$$

$$\theta_2 = \cos^{-1} \left( \frac{B_x}{2r} \right) \quad 2-84$$

$$\theta_3 = \pi - \theta_2 \quad 2-85$$

$$\theta_4 = \pi - \theta_3 \quad 2-86$$

where  $f_y$  is the feed in the Y-direction.

The corresponding chip thickness for each region can be presented as shown below:

For  $\theta_1 < \theta < \theta_2$

$$t_1(\theta) = \frac{B_x}{2 \cos \theta} - r \frac{\sin \left( \frac{\pi}{2} - \theta - \sin^{-1} \left( \frac{f_y \cos \theta}{r} \right) \right)}{\cos \theta} \quad 2-87$$

For  $\theta_2 < \theta < \frac{\pi}{2}$

$$t_2(\theta) = r - r \frac{\sin \left( \frac{\pi}{2} - \theta - \sin^{-1} \left( \frac{f_y \cos \theta}{r} \right) \right)}{\cos \theta} \quad 2-88$$

For  $\frac{\pi}{2} < \theta < \theta_3$

$$t_3(\theta) = r + r \frac{\sin \left( \frac{\pi}{2} - \theta - \sin^{-1} \left( \frac{f_y \cos \theta}{r} \right) \right)}{\cos \theta} \quad 2-89$$

For  $\theta_3 < \theta < \theta_4$

$$t_4(\theta) = r \frac{\sin \left( \frac{\pi}{2} - \theta - \sin^{-1} \left( \frac{f_y \cos \theta}{r} \right) \right)}{\cos \theta} - \frac{B_x}{2 \cos \theta} \quad 2-90$$

The chip flow angle in these areas are denoted by  $\Omega_1$ ,  $\Omega_2$ ,  $\Omega_3$ , and  $\Omega_4$  and can be obtained in the transformed coordinate system, as discussed by Kishawy et al. [84].

Finally, the resultant chip flow angle  $\bar{\Omega}$  can be obtained by using integration to get the summation of all terms, as shown in equation 2-91:

$$\bar{\Omega} = \tan^{-1} \left( \frac{\int_{\theta_1}^{\theta_2} \sin \Omega_1 r t_1(\theta) d\theta + \int_{\frac{\pi}{2}}^{\frac{\pi}{2}} \sin \Omega_2 r t_2(\theta) d(\theta)}{\int_{\theta_1}^{\theta_2} \cos \Omega_1 r t_1(\theta) d\theta + \int_{\frac{\pi}{2}}^{\frac{\pi}{2}} \cos \Omega_2 r t_2(\theta) d(\theta)} \right. \\ \left. + \frac{\int_{\frac{\pi}{2}}^{\theta_3} \sin \Omega_3 r t_3(\theta) d\theta + \int_{\theta_3}^{\theta_4} \sin \Omega_4 r t_4(\theta) d(\theta)}{\int_{\frac{\pi}{2}}^{\theta_3} \cos \Omega_3 r t_3(\theta) d\theta + \int_{\theta_3}^{\theta_4} \cos \Omega_4 r t_4(\theta) d(\theta)} \right)$$

2-91

## Chapter 3: Analytical-based modeling of metal cutting process with SPRT

### 3.1 Preamble

Li and Kishawy [85] developed an analytical force model for the machining process using self-propelled rotary tools. In their model, the conventional cutting forces of Oxley's theory was extended to include the tool motion effect. Prior knowledge of the tool rotational velocity is required to get the forces. The tool rotational velocity can be easily estimated using the frictionless rotary axis assumption. However, the friction in the rotary axis has been shown to not be negligible [86].

As discussed earlier, Armarego et al. [57] modeled the SPRT as an equivalent orthogonal process. In their model, the tool bearing friction was ignored, and thus, the tangential cutting force is equal to zero. In this case, the relative chip flow angle and the resultant cutting force must be perpendicular to the cutting edge in the equivalent relative coordinate system. This way, the process can be easily analyzed, and the tool rotational velocity  $V_r$  reaches its maximum value as provided in equation 3-1 [57]:

$$V_r = V \sin(i) \quad 3-1$$

The current proposed model is extending the previous equivalent orthogonal approach by including the bearing friction to achieve more accurate results. In this case, the tangential cutting force is no longer zero, and the chip flow angle inclines over the normal to the cutting-edge direction. Thus, the equivalent orthogonal concept can't be utilized; instead, the equivalent oblique approach is used to include the bearing friction, as discussed by Norikazu et al. [87]. The kinematic of the proposed model for the machining process with the SPRT is illustrated in Figure 3-1.



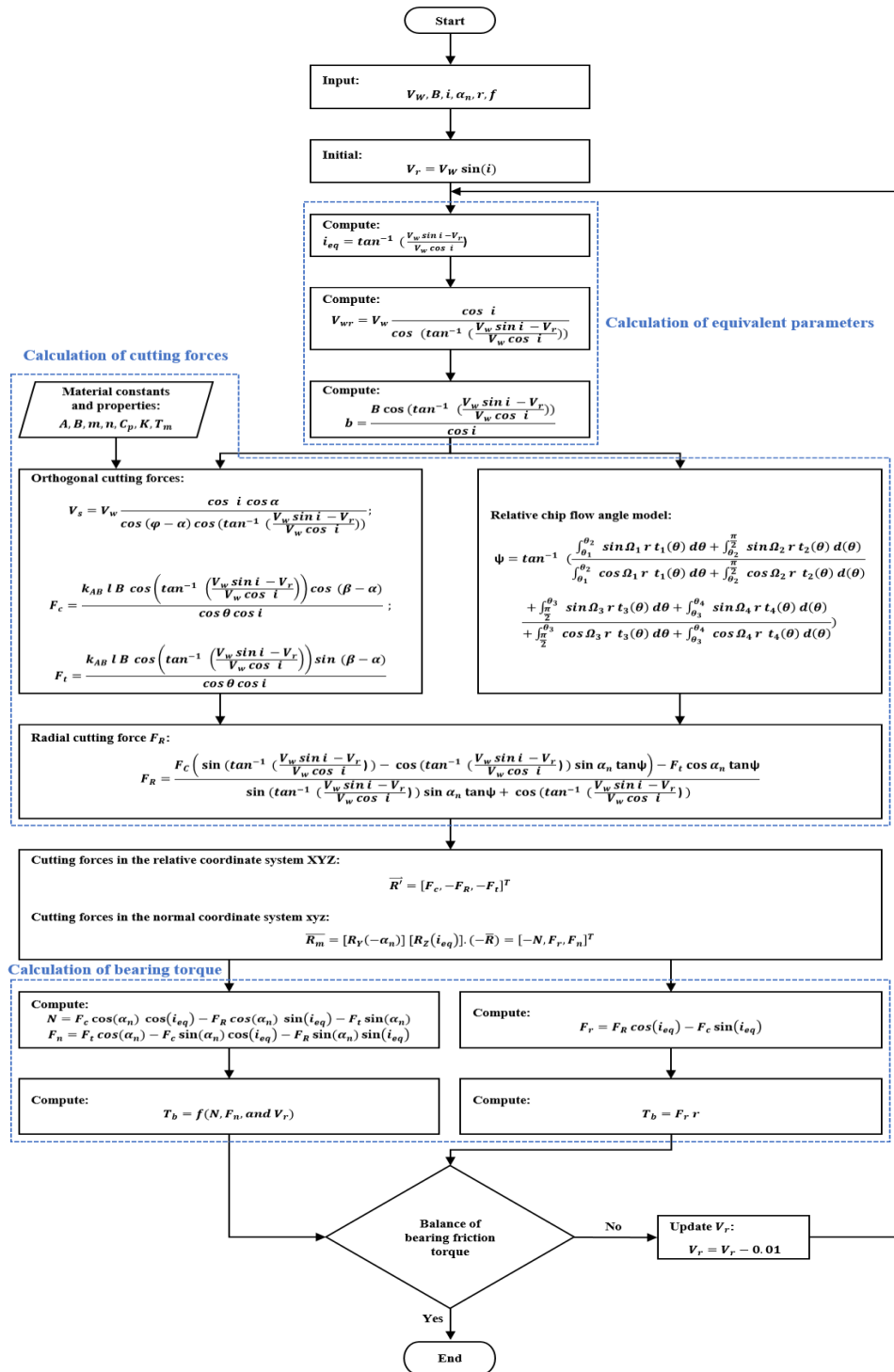


Figure 3-2. Flowchart for the cutting forces and tool motion predictions



The cutting velocity  $V_w$  can be expressed as shown in equation 3-2:

$$\vec{V}_w = \vec{V}_r + \vec{V}_{wr} \quad 3-2$$

where  $V_r$  is the tool rotational velocity, and  $V_{wr}$  is the relative cutting velocity.

Similarly, the chip velocity  $V_c$  can be found as provided in equation 3-3:

$$\vec{V}_c = \vec{V}_r + \vec{V}_{cr} \quad 3-3$$

where  $V_{cr}$  is the relative chip velocity.

The equivalent inclination angle  $i_{eq}$  can be obtained as can be seen in equation 3-4:

$$\tan i_{eq} = \frac{V_w \sin i - V_r}{V_w \cos i} \quad 3-4$$

The relative cutting velocity  $V_{wr}$  can then be determined based on equation 3-5:

$$V_{wr} = \frac{V_w \cos i}{\cos i_{eq}} \quad 3-5$$

The relationship between the absolute and relative cut widths can be presented as shown in equation 3-6:

$$b = \frac{B \cos i_{eq}}{\cos i} \quad 3-6$$

where  $B$  is the cutting width, and  $b$  is the relative cutting width.

### 3.3 Orthogonal cutting forces

Armarego et al. [68] have recognized that the cutting force  $F_c$  and the thrust force  $F_t$  are independent on the oblique inclination angle  $i$  for the same cutting conditions and normal rake angle  $\alpha_n$ . Accordingly, Lin et al. [78] proved that the orthogonal cutting force  $F_c$  and the orthogonal thrust force  $F_t$  can be obtained and used as oblique force components by replacing the orthogonal rake angle  $\alpha$  with the oblique normal rake angle  $\alpha_n$ . Oxley [64] has developed an analytical model to predict orthogonal cutting forces, temperature, and stresses. This model is known as the chip flow model, which is based on the slip line theory. The cutting conditions and workpiece material properties are utilized in his model. Lalwani et al. [80] extended this model to use the Johnson-Cook flow stress equation instead of the material's power law, which was used by Oxley. The effect of the strain, strain rate, and temperature on the material flow stress are considered in the Johnson-Cook material model.

In the current model, the extended Oxley's model is modified in order to include the SPRT equivalent parameters (i.e., relative cutting speed  $V_{wr}$  and relative width of cut  $b$ ) to determine the cutting force  $F_c$  and the thrust force  $F_t$  for the SPRT. Extension of Oxley's machining theory was discussed in detail by Lalwani et al. [80]. Thus, the final modified relationships expressing the shear velocity, cutting force, and the thrust force are provided in equation 3-7, equation 3-8, and equation 3-9, respectively.

$$V_s = V_w \frac{\cos i \cos \alpha}{\cos (\phi - \alpha) \cos \left( \tan^{-1} \left( \frac{V_w \sin i - V_r}{V_w \cos i} \right) \right)} \quad 3-7$$

$$F_c = \frac{k_{AB} l B \cos \left( \tan^{-1} \left( \frac{V_w \sin i - V_r}{V_w \cos i} \right) \right) \cos (\beta - \alpha)}{\cos \theta \cos i} \quad 3-8$$

$$F_t = \frac{k_{AB} l B \cos \left( \tan^{-1} \left( \frac{V_w \sin i - V_r}{V_w \cos i} \right) \right) \sin (\beta - \alpha)}{\cos \theta \cos i} \quad 3-9$$

where  $\phi$  is the shear angle,  $k_{AB}$  is the shear stress at the primary shear plane,  $l$  is the length of the plane AB and  $B$  is the width of cut, and  $\theta$  is the angle between the plane AB and the force  $R$ .

### 3.4 Radial cutting force

The third force component  $F_R$ , which is normal to the cutting force  $F_C$  and thrust force  $F_t$ , can be obtained as a function of the relative chip flow angle  $\psi$ . For this reason, the model presented in Kishawy et al. [84] is used in this study to predict the relative chip flow angle for SPRT, as seen in equation 3-10:

$$\psi = \tan^{-1} \left( \frac{\int_{\theta_1}^{\theta_2} \sin \Omega_1 r t_1(\theta) d\theta + \int_{\frac{\pi}{2}}^{\pi} \sin \Omega_2 r t_2(\theta) d(\theta)}{\int_{\theta_1}^{\theta_2} \cos \Omega_1 r t_1(\theta) d\theta + \int_{\frac{\pi}{2}}^{\pi} \cos \Omega_2 r t_2(\theta) d(\theta)} + \frac{\int_{\frac{\pi}{2}}^{\theta_3} \sin \Omega_3 r t_3(\theta) d\theta + \int_{\theta_3}^{\theta_4} \sin \Omega_4 r t_4(\theta) d(\theta)}{\int_{\frac{\pi}{2}}^{\theta_3} \cos \Omega_3 r t_3(\theta) d\theta + \int_{\theta_3}^{\theta_4} \cos \Omega_4 r t_4(\theta) d(\theta)} \right) \quad 3-10$$

where  $\theta_1, \theta_2, \theta_3$ , and  $\theta_4$  are boundary angles for different regions of chip loads,  $t_1, t_2, t_3$ , and  $t_4$  are chip widths corresponding to the boundary angles, and  $\Omega_1, \Omega_2, \Omega_3$ , and  $\Omega_4$  are local chip flow angles for different range of boundary angles.

The resultant force  $R'$  can be presented, as given in equation 3-11:

$$\vec{R}' = \begin{bmatrix} -F_c \\ F_R \\ F_t \end{bmatrix} \quad 3-11$$

This resultant force vector is presented in the relative coordinate system (i.e., XYZ in Figure 3-1), which mean  $F_c$  is in the direction of the relative cutting velocity  $V_{wr}$ . Based on the fact that the resultant force  $R'$  lies on the plane containing the chip force  $F$  and the normal to the rake face force  $N$ , the radial force  $F_R$  can be obtained by rotating the relative coordinate system XYZ around (a) Z-axis with angle ( $i_{eq}$ ), (b) Y-axis with angle ( $-\alpha_n$ ), and (c) X-axis with angle ( $-\psi$ ). Accordingly, the final rotational matrix  $[M]$  can be expressed, as shown below:

$$\begin{aligned} [M] &= [R_X(-\psi)] \cdot [R_Y(-\alpha_n)] \cdot [R_Z(i_{eq})] \\ &= \begin{bmatrix} 1 & 0 & 0 \\ 0 & \cos(-\psi) & -\sin(-\psi) \\ 0 & \sin(-\psi) & \cos(-\psi) \end{bmatrix} \begin{bmatrix} \cos(-\alpha_n) & 0 & \sin(-\alpha_n) \\ 0 & 1 & 0 \\ -\sin(-\alpha_n) & 0 & \cos(-\alpha_n) \end{bmatrix} \begin{bmatrix} \cos(i_{eq}) & -\sin(i_{eq}) & 0 \\ \sin(i_{eq}) & \cos(i_{eq}) & 0 \\ 0 & 0 & 1 \end{bmatrix} \\ &= \begin{bmatrix} \cos(-\alpha_n) & 0 & \sin(-\alpha_n) \\ \sin(-\psi) \sin(-\alpha_n) & \cos(-\psi) & -\sin(-\psi) \cos(-\alpha_n) \\ -\cos(-\psi) \sin(-\alpha_n) & \sin(-\psi) & \cos(-\psi) \cos(-\alpha_n) \end{bmatrix} \\ &= \begin{bmatrix} \cos(-\alpha_n) \cos(i_{eq}) \\ \sin(-\psi) \sin(-\alpha_n) \cos c + \cos(-\psi) \sin(i_{eq}) \\ -\cos(-\psi) \sin(-\alpha_n) \cos c + \sin(-\psi) \sin(i_{eq}) \\ -\cos(-\alpha_n) \sin(i_{eq}) & \sin(-\alpha_n) \\ -\sin(-\psi) \sin(-\alpha_n) \sin(i_{eq}) + \cos(-\psi) \cos(i_{eq}) & -\sin(-\psi) \cos(-\alpha_n) \\ \cos(-\psi) \sin(-\alpha_n) \sin(i_{eq}) + \sin(-\psi) \cos(i_{eq}) & \cos(-\psi) \cos(-\alpha_n) \end{bmatrix} \quad 3-12 \end{aligned}$$

where  $R_X, R_Y, R_Z$  are the rotating matrixes around X, Y, and Z, respectively.

The resultant force vector  $\vec{R}''$  in the new coordinate system is then found as provided in equation 3-13:

$$\vec{R}'' = [M].\vec{R}' = \begin{bmatrix} -N \\ 0 \\ F \end{bmatrix} \quad 3-13$$

In order to satisfy the condition that the resultant force  $R$  lies on the plane containing the chip force  $F$  and the normal to the rake force  $N$ , the  $Y$  component of the  $\vec{R}'$  must be zero. Accordingly, the third force component  $F_R$  is obtained, as provided in equation 3-14:

$$F_R = \frac{F_C(\sin i_{eq} - \cos i_{eq} \sin \alpha_n \tan \psi) - F_t \cos \alpha_n \tan \psi}{\sin i_{eq} \sin \alpha_n \tan \psi + \cos i_{eq}} \quad 3-14$$

Finally, in order to determine the force components in the machining coordinate system, which can be compared to the experimental results, the relative coordinate system XYZ needs to be rotated around  $Z$ -axis with angle  $(i - i_{eq})$ .

### 3.5 Bearing friction

In the steady-state cutting condition, the force component  $F_r$ , which is in the tangential direction of the tool motion, should be equal to the coming force from the bearing friction torque  $T_b$ . Accordingly, the bearing friction torque  $T_b$  can be calculated from the bearing characteristics (as shown in equation 3-20) or by using the tangential force  $F_r$  multiplied by the insert radius  $r$ . The tangential force  $F_r$  can be obtained as a function of  $F_C$ ,  $F_t$ , and  $F_R$  by rotating the relative coordinate system XYZ around (a)  $Z$ -axis with angle  $(i_{eq})$  and (b)  $Y$ -axis with angle  $(-\alpha_n)$ , as shown in  $[M_o]$  (equation 3-15) :

$$\begin{aligned}
 [M_o] &= [R_Y(-\alpha_n)]. [R_Z(i_{eq})] \\
 &= \begin{bmatrix} \cos(-\alpha_n) & 0 & \sin(-\alpha_n) \\ 0 & 1 & 0 \\ -\sin(-\alpha_n) & 0 & \cos(-\alpha_n) \end{bmatrix} \begin{bmatrix} \cos(i_{eq}) & -\sin(i_{eq}) & 0 \\ \sin(i_{eq}) & \cos(i_{eq}) & 0 \\ 0 & 0 & 1 \end{bmatrix} \quad 3-15 \\
 &= \begin{bmatrix} \cos(-\alpha_n) \cos(i_{eq}) & -\cos(-\alpha_n) \sin(i_{eq}) & \sin(-\alpha_n) \\ \sin(i_{eq}) & \cos(i_{eq}) & 0 \\ -\sin(-\alpha_n) \cos(i_{eq}) & \sin(-\alpha_n) \sin(i_{eq}) & \cos(-\alpha_n) \end{bmatrix}
 \end{aligned}$$

The resultant force vector  $\vec{R}_o$  in the normal coordinate system (i.e., xyz in Figure 3-1) can be found as provided in equation 3-16:

$$\vec{R}_o = [M_o]. \vec{R}' = [-N, F_r, F_n]^T \quad 3-16$$

Therefore, the tangential force component  $F_r$  is then calculated as shown in Equation 3-17:

$$F_r = -F_c \sin(i_{eq}) + F_R \cos(i_{eq}) \quad 3-17$$

The other two force components  $N$  and  $F_n$  are provided in equation 3-18 and equation 3-20:

$$N = F_c \cos(\alpha_n) \cos(i_{eq}) - F_R \cos(\alpha_n) \sin(i_{eq}) - F_t \sin(\alpha_n) \quad 3-18$$

$$F_n = F_t \cos(\alpha_n) - F_c \sin(\alpha_n) \cos(i_{eq}) - F_R \sin(\alpha_n) \sin(i_{eq}) \quad 3-19$$

The bearing's coefficient of friction  $\mu_b$  is not constant but depending on the tribological characteristics, which are function in bearing type, axial load, radial load,

Chapter 3: Analytical-based modeling of metal cutting process with SPRT and rotational speed, as detailed in the SKF model [88]. The bearing friction torque is expressed, as shown in equation 20:

$$T_b = 0.5 d \mu_b \sqrt{N^2 + F_n^2} \quad 3-20$$

where  $d$  is the insert diameter,  $\mu_b$  is the bearing friction coefficient,  $N$  is the bearing axial force, and  $F_n$  is the bearing radial force.

### **3.6 Model validation and discussion**

The cutting forces obtained from previous work [85] were used to validate the current proposed model. Li and Kishawy [85] have performed tube end turning for SAE 1045 carbon steel tube with 2 mm thickness. Three cutting speeds were used; 120 m/min, 170 m/min, and 280 m/min; and four feed rates were selected: 0.1 mm/rev, 0.125 mm/rev, 0.15 mm/rev, and 0.2 mm/rev. Carbide round inserts with a diameter 27 mm was used. The tool rake angle was  $-5^\circ$ , while the tool inclination angle was  $17^\circ$ . For each run, the three cutting force components were measured using Kistler 9251A dynamometer.

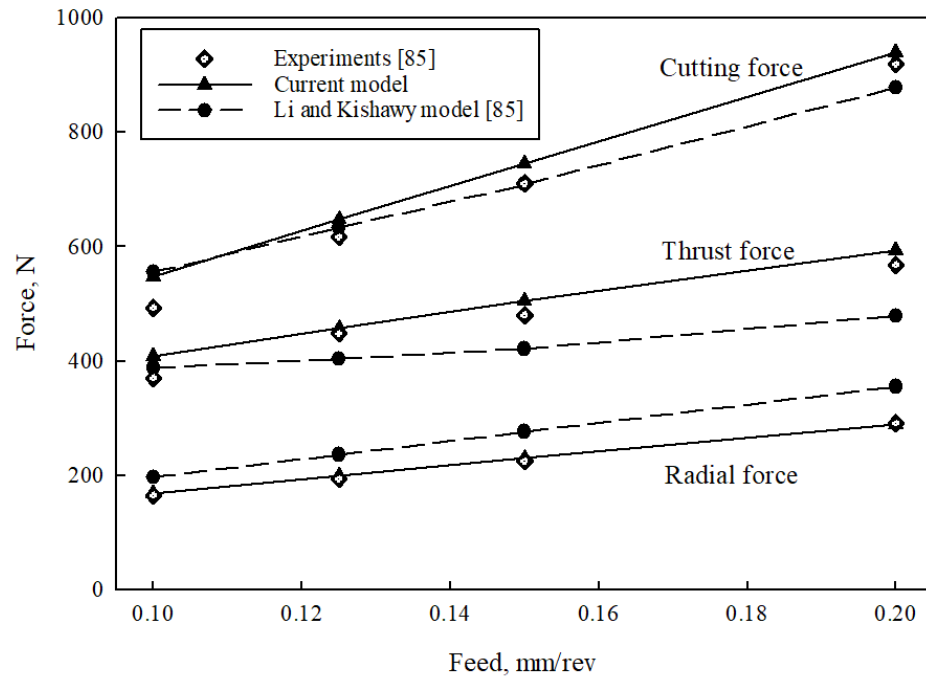


Figure 3-4. A comparison between the predicted and measured forces at cutting velocity of 120 m/min

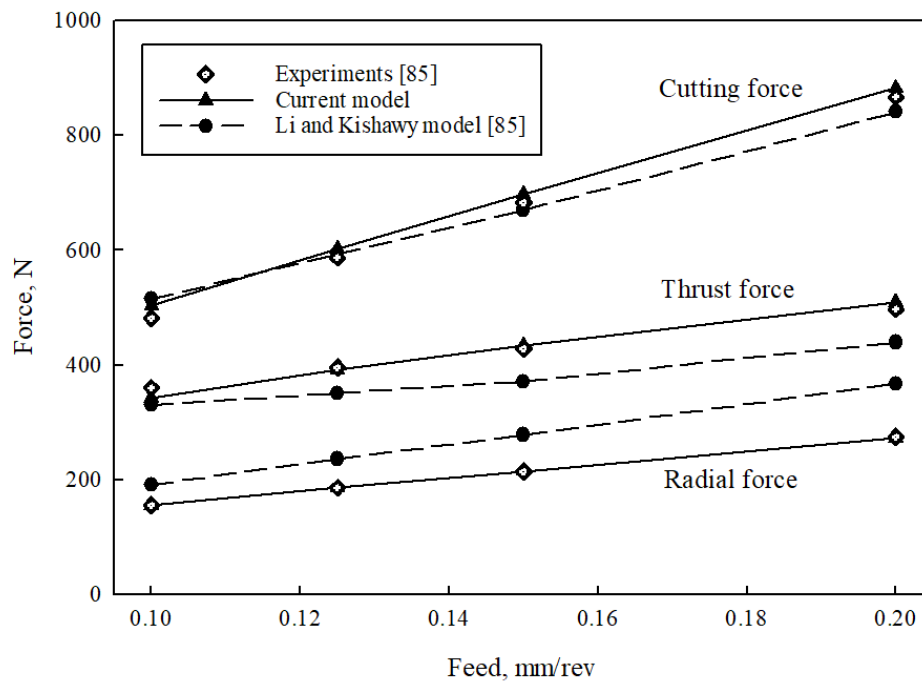


Figure 3-5. A comparison between the predicted and measured forces at cutting velocity of 170 m/min

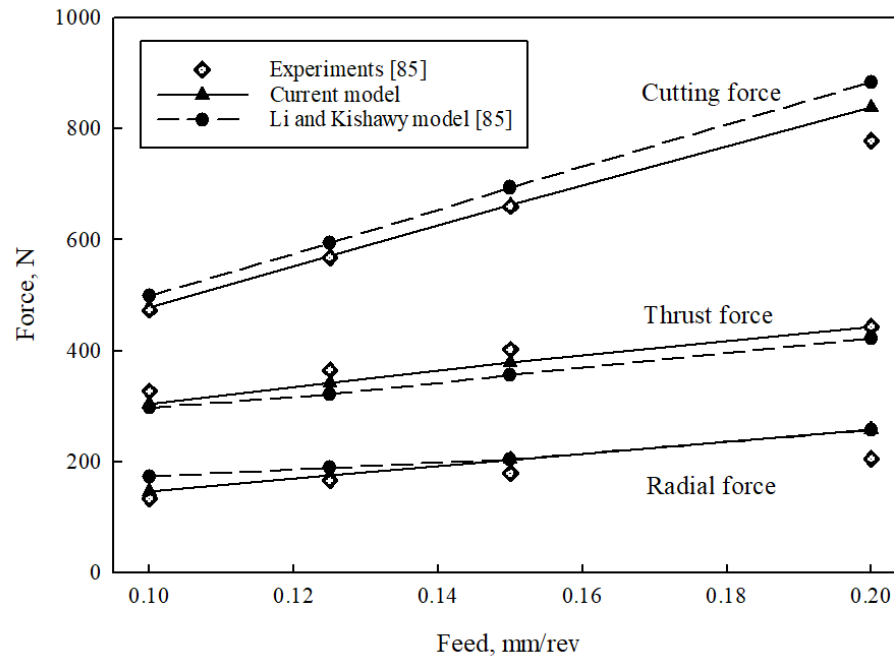


Figure 3-6. A comparison between the predicted and measured forces at cutting velocity of 230 m/min

Figure 3-4, Figure 3-5, and Figure 3-6 show a comparison between the proposed model, Li's model, and experimentally measured forces at three different cutting velocities; 120 m/min, 170 m/min, and 230 m/min, respectively. The results show linear relations between the feed rates and the cutting forces for constant cutting velocity (i.e., cutting forces increases with the increase of feed rate values). The proposed model results are more accurate compared to Li's model results and almost consistent with the measured experimental cutting forces, even under using different values of feed rate. For example, in Figure 3-6, the maximum error obtained is around 5%. In addition, at a cutting speed of 120 m/min (see Figure 3-4), the proposed model showed an average accuracy of 95.5%. In general, the overall model accuracy for all cutting experiments is 94.54%, with a maximum error of 25.85%. The only relatively high error was found in the radial force prediction at one point (i.e., cutting velocity of 230 m/min and feed rate of 0.2 mm/rev). That is attributed to the small magnitude of the radial force components, which means any slight difference will lead to a high error percentage.

### Chapter 3: Analytical-based modeling of metal cutting process with SPRT

The obtained errors in the radial and cutting force components were relatively high at the highest level of cutting speed and feed rate. That's mainly because the model assumes that the inclination angle of the round cutting edge is consistent with the tool inclination angle, while in reality, the engaged portion of the cutting edge with the workpiece isn't straight and has a curvature shape. To sum up, the maximum error occurred at the highest levels of feed rate and cutting speed is related to the maximum tool rotational speed, as will be clarified when presenting the tool rotational speed results. Other sources of error can be due to the difficulty of exactly setting the tool in the center of the tube thickness, which changes the chip flow speed and chip angle. Besides, no chip side flow is considered in the current model.

Regarding the tool's rotational speed, the predicted results are compared to the experimental results, which were obtained by Kishawy and Wilcox [61], as shown in Figure 3-7. A good agreement between the measured and predicted values is observed, as the current proposed model considers the reduction in the tool rotational speed due to the friction of the bearing. It is found that the average accuracy of the proposed model is 93.63%. The best agreement is observed at an inclination angle of 20°, while the error seems to be increased as cutting speed increases. That could be due to assumptions made (i.e., no chip side flow and the tool is exactly centered in the middle of the tube thickness), which is mentioned earlier. However, the obtained error is still within the acceptable limit (i.e., the maximum error of 22% and an average error of 6%). It can be seen that the relationship between the cutting speed and the tool's rotational speed is linear for all used inclination angles. Besides, increasing the inclination angle at the same cutting speed will lead to an increase in the tool rotational speed.

It should be stated that the current proposed model offers the unique capability to accurately predict the tool rotational speed values, which is a significant design aspect when machining with SPRT. Besides, having such a valuable aspect (i.e., tool rotational speed) is also significantly important to determine the cutting forces.

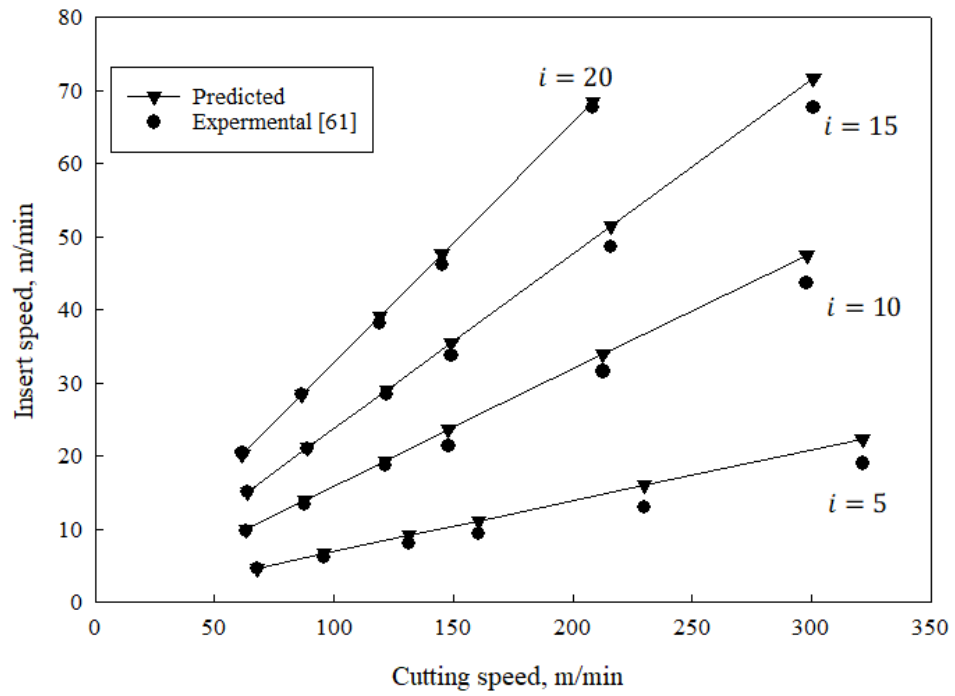


Figure 3-7. A comparison between the predicted and measured tool rotational speeds

# Chapter 4: Finite element modeling

## 4.1 Preamble

The main objectives of metal cutting studies are to find the best cutting conditions and cutting tool geometry parameters (i.e., cutting angles) to obtain the highest process efficiency. The experimental approach can be used to achieve the mentioned objectives; however, experimental tests are expensive in terms of operating costs and the cycle time. Analytical models are also utilized to study the cutting processes in terms of cutting forces, tool wear, and machining temperature; however, these models have limited applications and cannot be used for complex operations. That is because all the analytical models are based on a lot of assumptions, which leads to a large deviation between the models and the actual processes.

Finite Element Modeling (FEM) is a suitable solution that can be used to simulate and model cutting processes with a minimum number of assumptions, and without needing to perform any experimental tests. Recently, finite element methods (FEM) are widely used to simulate the metal cutting process. The reason behind that is the ability of the FEM to predict various machining characteristics such as temperature and stresses, which are not easy to be experimentally measured. Furthermore, the complex tool geometries can be built up similar to the actual tool geometries, unlike the analytical models, which usually use the sharp cutting edge assumption. Moreover, the FEM can predict an accurate chip shape (i.e., chip flow angle and chip thickness) better than analytical models. Besides, it can be used to simulate any complex process with various cutting conditions.

In this chapter, Finite Element Modeling (FEM) based on a material plastic model, damage model, and friction law is utilized to simulate the cutting process using SPRT. The used geometry and mesh characteristics are presented. Afterward, detailed

information in terms of materials behavior (i.e., constitutive equations) and interaction model between the tool and workpiece are described. Finally, in order to validate the current model, a comparison between the experimental and predicted results is presented in terms of cutting forces and the chip morphology.

## 4.2 Model formation

Three different models can be used to simulate the metal cutting process; Lagrangian, Eulerian, and arbitrary Lagrangian-Eulerian (ALE). The Lagrangian approach is usually used for solving solid problems. In this model, the mesh elements are assigned to the tool and the workpiece solid materials. Therefore, this model is preferred for unconstrained material flow problems. For this reason, the Lagrange model is used in the metal cutting simulation due to its ability to predict the chip geometry formation from the beginning without needing to initially include the formed chip in the workpiece geometry domain, which requires prior knowledge of the chip shape and dimensions. Besides, this model can be used to predict different types of chips such as continuous, discontinuous, and saw-tooth chips by assigning failure criteria to the workpiece materials. However, this model has some drawbacks; the main disadvantage is the high distortion of the elements, which occurs due to high plastic stresses during metal cutting simulations. This issue can be avoided by using the available remeshing techniques such as adaptive or automatic remeshing; however, it is computationally expensive, especially with 3D models.

Eulerian model is usually used to simulate flow problems, but some attempts utilized the Eulerian model to solve solid problems. In this model, the mesh elements are assigned to a certain control volume domain, which is fixed in the space, and the material can be moved within this domain (i.e., enter or leave the domain boundaries). According to that, the element distortion issue is solved in this model; besides, a relatively low number of elements, comparing to the Lagrangian model, can be used to simulate the problem. Furthermore, the steady-state solution can be easily achieved using this model. Moreover, there is no need to define chip separation criteria.

However, the main disadvantage of using this model in metal cutting simulation is that the chip geometry shape should be known and considered in the workpiece domain in advance (i.e., before starting the solution). In other words, the chip thickness and the contact length between the tool and the chip should be known before starting the solution. Also, the contact conditions between the chip and the workpiece are assumed to be constant during the solution. As a result, this assumption makes the Eulerian model does not match an actual metal cutting process.

The Arbitrary Lagrange-Eulerian (ALE) model is used to have a combination of the Lagrange and Eulerian models. In this model, the mesh is not attached to the solid domain, and also it is not assigned to a fixed control volume in the space. Instead, the mesh follows the flow of the solid domain, and the elements reposition itself after each time step. By doing that, the elements distortion problem, which occurs in the Lagrange model, is avoided without using any remeshing techniques. Initial estimation of the chip should be defined in the workpiece model, and then the final shape of the chip is obtained during the analysis. Figure 4-1 shows the boundary conditions used in the ALE model.

It should be noticed that the Eulerian and Arbitrary Lagrange-Eulerian (ALE) model can be used only for orthogonal cutting cases, as these are simple cases, and the chip flows normal to the cutting edge. For complex process such as the current case (i.e., rotary tools), using of Lagrange model is the best way for the simulation, since there is no need to include the chip in the workpiece geometry.



where  $\nu$  and  $\dot{\varepsilon}_0$  are material constants, while  $\dot{\varepsilon}$  is the strain rate.

- Johnson and Cook model: This model was developed in 1983 by Johnson and Cook [75]. In this model, the stress relates to the torsion and Hopkinson bar experiment results, which should be obtained for a wide range of temperatures and strain rates. This model is widely used in the metal cutting simulation. The static yield stress  $\sigma^o$  in this model is defined by equation 4-3:

$$\sigma^o = (A + B \bar{\varepsilon}_{pl}^n) \left[ 1 + C \ln \left( \frac{\dot{\bar{\varepsilon}}_{pl}}{\dot{\varepsilon}_0} \right) \right] \left[ 1 - \left( \frac{T - T_{ref}}{T_{melt} - T_{ref}} \right)^m \right] \quad 4-3$$

where A, B, C, n, m and  $\dot{\varepsilon}_0$  are material constants, which can be experimentally obtained at the reference temperature  $T_{ref}$ . Besides,  $\bar{\varepsilon}_{pl}$  is the equivalent plastic strain, and  $\dot{\bar{\varepsilon}}_{pl}$  is the equivalent plastic strain rate. Besides, this model assumes that the previous parameters are independently affecting the yield stress. The first bracket in the Johnson-Cook equation is the elastic-plastic related term, and it presents the strain hardening. The second bracket is the viscosity term, and it shows that the material stress increases at high strain rates. The last bracket accounts for the temperature softening effect.

- Zerilli- Armstrong Material Model: This model has been developed in 1987 for face-centered cubic (f.c.c) and body-centered cubic (b.c.c) materials [91]. There are two different models due to the high difference in temperature and the strain rate response between these two material types:

- The equation for b.c.c can be written as shown in equation 4-4:

$$\sigma = C_0 + C_1 \exp(-C_3 T + C_4 T \ln \frac{\dot{\varepsilon}}{\dot{\varepsilon}_0}) + C_5 \varepsilon^n \quad 4-4$$

- The equation for f.c.c can be presented by equation 4-5:

$$\sigma = C_0 + C_2 \varepsilon^{-1/2} \exp(-C_3 T + C_4 T \ln \frac{\dot{\varepsilon}}{\dot{\varepsilon}_0}) \quad 4-5$$

where  $C_0$  is the stress component to consider the dislocation density on the material flow stress. While  $C_1$  to  $C_5$  and  $n$  are material constants.

Many studies were done using different material constitutive models. For example, a rigid plastic model was used by Ceretti et al. [92] in 1999. Besides, a rigid viscoplastic model was used by Kountanya [93] in 2002. Furthermore, elasto-viscoplastic model was also utilized in the Umbrello et al. work [94]. Elastic-plastic materials model is also commonly used to simulate the metal cutting process. The plastic strain rate dependency was used in some studies as well [93, 95]. Moreover, Johnson and Cook (JC) presented elasto-thermo-visco-plastic material model [96], which is widely used to simulate the metal cutting process. Many previous studies proved the effectiveness of this model [97, 98]. Johnson and Cook's model was improved by Sima and Ozel [99] by including the effect of the temperature on the material softening.

## 4.4 Chip separation modeling

Different methods can be used to simulate the chip formation. These methods are classified as follow:

- Node separation technique: this is a geometry-based method [100, 101], in which the chip separation occurs along a pre-defined parting line. This line is used to separate the chip from the workpiece, as shown in Figure 4-2. Along the parting line, every two nodes are tied together and initially have the same degree of freedom. When the cutting tool approaches this point, the separation between the nodes occurs once a pre-specified criterion is met. Many separation criteria can be used include node distances, maximum plastic strain, and maximum effective stress.

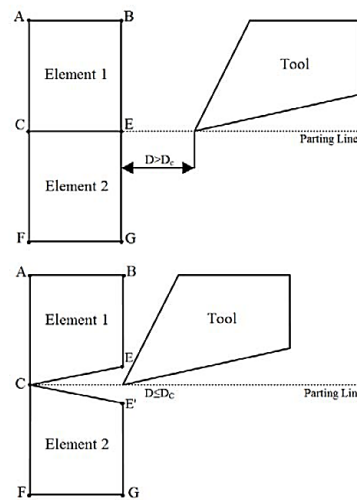


Figure 4-2. Node separation technique [102]

- Element deletion technique: this method is also based on the geometry approach. A predefined sacrificial element zone is assigned between the chip and the workpiece to have a chip separation [103], as shown in Figure 4-3. The elements are deleted when the predefined criteria, such as maximum distance or maximum energy, are met.

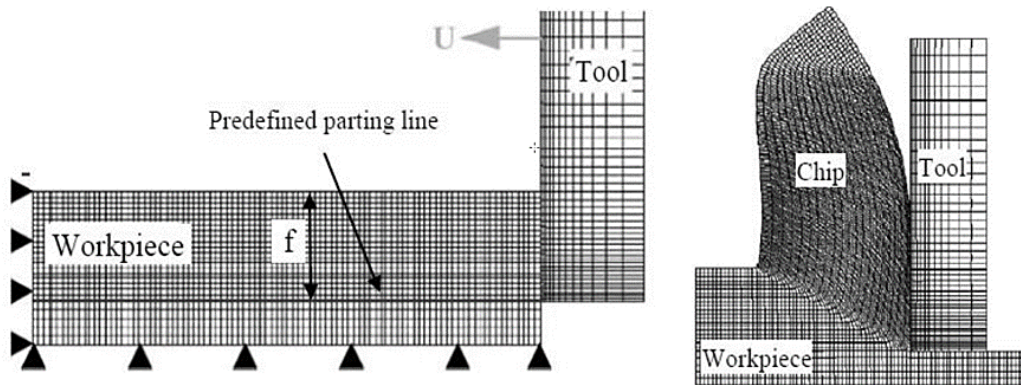


Figure 4-3. Element deletion technique [104]

## 4.5 Failure damage models

The failure damage model is used to simulate the chip formation. Figure 4-4 shows the uniaxial stress-strain diagram for a ductile material. The stress-strain relation is linear in the first part (OA), followed by a plastic yielding zone associated with strain hardening (region AB). The curve (ABC) shows undamaged stress-strain behavior. The damage effect starts at point B and causes a gradual decrease in the hardening modulus (i.e., tangent modulus). The maximum stress occurs at point D when the tangential modulus reaches zero, at which the significant value of D is higher than 0.3 and lower than 0.7 depending on the material type. The observed fracture occurs at point E, while point F represents the theoretical fracture. The deformation in the zone (BF) occurs locally in the neck portion of the workpiece. As the damage starts at point B, the evolution of stiffness degradation is used to govern the stress-strain behavior beyond that point (i.e., region BF) at the localization stress area. There are two steps for the chip formation in the ductile failure approach. The first step relates to the damage initiations, while the second step relates to the damage evaluation by the fracture energy method.

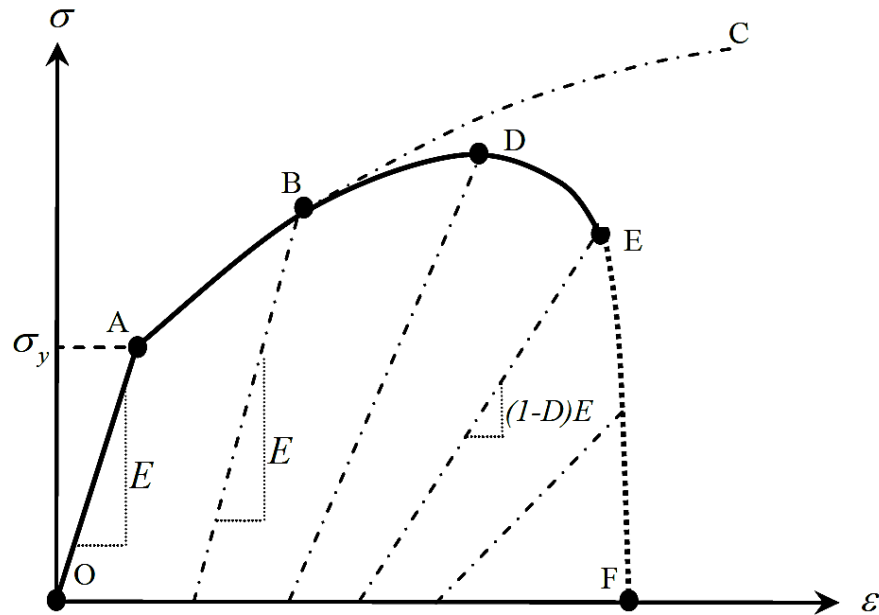


Figure 4-4. Stress-strain relation for a metal workpiece

### 4.5.1 Damage initiation

In the current study, Johnson-Cook damage initiation criteria is used. For this model, five different parameters ( $D_1$ ,  $D_2$ ,  $D_3$ ,  $D_4$ , and  $D_5$ ) should be defined. These parameters can be experimentally obtained for any workpiece material. As can be seen in Equation 4-6, the fracture strain is calculated based on the triaxiality stress (i.e., the average of the normal stress components over the Von-Mises equivalent stress), the strain rate, and the temperature [96]. The first bracket addresses the effect of stress triaxiality and can be estimated based on Hancock expression [105]. While the second bracket indicates the effect of the strain rate. Besides, the third bracket is included to consider the temperature effect.

$$\mathcal{E}^f = [D_1 + D_2 \exp D_3 \sigma^*][1 + D_4 \ln \dot{\mathcal{E}}^*][1 + D_5 T^*] \quad 4-6$$

where  $\mathcal{E}^*$  is the dimensionless strain rate, and  $T^*$  is the homogeneous temperature, and it can be calculated as shown in equation 4-7:

$$T^* = \frac{T - T_{room}}{T_{melt} - T_{room}} \quad 4-7$$

where  $T_{room}$  is the room temperature, while  $T_{melt}$  is the material melting temperature.

Besides,  $\sigma^*$  is the triaxiality stress, and it can be calculated as shown in equation 4-8:

$$\sigma^* = \frac{1}{3} + \ln \left( 1 + \frac{a}{2R} \right) \quad 4-8$$

where  $R$  is the curvature radius of the neck in the tensile test, and “a” is the minimum cross-section radius.

According to this model, the damage initiated is based on a cumulative law, which is used to obtain a scalar damage parameter  $w$  (see equation 4-9). The damage is initiated when the value of  $w$  exceeds one.

$$w = \sum_{i=1}^n \left( \frac{\Delta \bar{\mathcal{E}}^p}{\bar{\mathcal{E}}_F^p} \right)_i \quad 4-9$$

where  $\Delta \bar{\mathcal{E}}^p$  is the equivalent plastic strain increment, and  $\bar{\mathcal{E}}_F^p$  is the fracture equivalent plastic strain.

## 4.5.2 Damage evaluation

The fracture energy damage evaluation model was presented by Hillerborg [106]. This model is used to offer a stable failure process by controlling the material degradation, which occurs after the damage initiates. Besides, it is also used to detect the high strain localization, which occurs during chip formation.

When material damage occurs, the behavior of the material no longer follows the stress-strain relationship, especially when using relatively coarse elements. That is because the energy dissipation is strongly affected by the mesh size based on the strain location. However, the material behavior can still be modeled by the stress-strain relationship even after the damage initiates when using a very fine mesh size (i.e., 2  $\mu\text{m}$ ), as presented and discussed by Calamaz [107]. After damage initiations, the fracture energy damage evaluation ( $G_f$ ) is used to reduce the mesh dependency by applying different stress displacement relation, which is expressed by equation 4-10:

$$G_f = \int_{\bar{\varepsilon}_B^p}^{\bar{\varepsilon}_F^p} L \bar{\sigma} d\bar{\varepsilon}^p = \int_0^{\bar{u}_F^p} \bar{\sigma} d\bar{u}^p \quad 4-10$$

where  $L$  is the characteristic length, which is equal to the square root of the area bounded by the integration points. Besides,  $\bar{\varepsilon}_B^p$  is the equivalent plastic strain at point B (see Figure 4-4), and  $\bar{\varepsilon}_F^p$  is the fracture equivalent plastic strain (point F in Figure 4-4). Besides,  $\bar{u}^p$  is the equivalent plastic displacement, while  $\bar{\sigma}$  is the equivalent stress.

The stiffness degradation of the damage process region (EF) is expressed by equation 4-11:

$$D = \frac{\int_{\bar{\varepsilon}^p l_B}^{\varepsilon^f} L \bar{\sigma} d\bar{\varepsilon}^p l_B}{G_f} \quad 4-11$$

The damage occurs when  $D$  reaches unity (point F). Where the material damage energy  $G_f$  can be given by equation 4-12:

$$G_f = K_c^2 \frac{(1 - \nu^2)}{E} \quad 4-12$$

Where  $K_c$  is the material fracture toughness, which can be experimentally obtained.

## 4.6 Friction modeling

The friction interaction between the tool and the workpiece is complicated, especially when machining using rotary tools due to the extra rotational motion of the tool. Not only the tool temperature, tool wear, and surface roughness are affected by the friction interaction, but also the power consumption during the machining process. The stick-slip friction model is one of the most widely used models for the friction interaction in the metal cutting simulation area. This model was developed by Zorev [108] in 1963. In this model, two different contact regions take place along the contact length. The first one is the sticking region, which occurs near the cutting edge tip. In this region, the shear stress is assumed to be constant and equal the material yield shear stress  $\tau_Y$ . On the other hand, the remaining region is the sliding region, in which the shear stress  $\tau$  is proportional to the normal stress  $\sigma_n$ . This model can be presented by equation 4-13:

$$\tau_f = \begin{cases} \tau_Y, 0 \leq l \leq l_c \ (\mu\sigma_n \geq \tau_Y) & \rightarrow \text{stick} \\ \mu\sigma_n, l > l_c \ (\mu\sigma_n < \tau_Y) & \rightarrow \text{slide} \end{cases} \quad 4-13$$

where  $\mu$  is the Coulomb's friction coefficient, and  $l_c$  is the contact length between the chip and the tool. As mentioned before, this contact length should be known in advance when using Eulerian and arbitrary Lagrangian-Eulerian approaches. However, it is not required to be known when using the Lagrangian approach, which is used in the current study. In addition, there are some different methods that also used to define the friction during the metal cutting simulation. For example, an average friction coefficient was assumed in the contact area between the tool and the chip in a few works. Furthermore,

other works [109, 110] assumed constant friction stress on the rake face, which can be roughly estimated by equation 4-14, where  $m$  is lower than one.

$$\tau_f = m \tau_Y \quad 4-14$$

However, other studies [111-113] used more realistic models. Moreover, Usui et al. [114] presented an experimental model in order to relate the non-linearly friction stress to the normal stress, as shown in equation 4-15:

$$\tau_f = \tau_Y \left[ 1 - \exp \left( -\frac{\mu \sigma_n}{\tau_Y} \right) \right] \quad 4-15$$

where  $\mu$  is the tool-chip materials constant (i.e., the friction coefficient), and  $\tau_Y$  is the yield shear stress of the chip. From equation 4-15, it can be seen that  $\tau_f = \tau_Y$  at large normal stress (sticking zone), and  $\tau_f = \mu \sigma_n$  at small normal stress (sliding region), as shown in Figure 4-5.

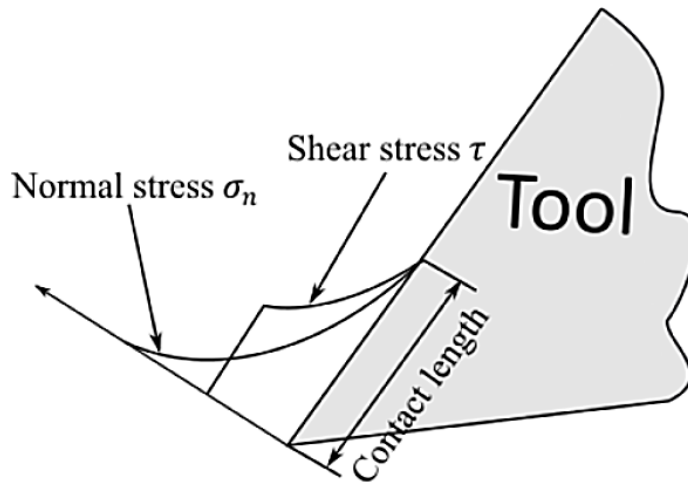


Figure 4-5. Normal and shear stresses along the rake face [108]

The previous model was modified later by Childs et al. [115, 116], as shown in equation 4-16:

$$\tau_f = m\tau_Y [1 - \exp(-\frac{\mu\sigma_n}{m\tau_Y})^n]^{1/n} \quad 4-16$$

where  $n$  is used to control the contact region (i.e., sticking or sliding), and  $m$  is used to consider the lubrication effect.

Özel [117] compared the experimental results based on the previous models, and he found that the results were more accurate when using friction models compared to the obtained results, which were based on the measured normal and friction stresses. Furthermore, Iwata et al. [118] experimentally developed a friction model, which was based on the friction coefficient, Vickers hardness  $H_V$ , and normal stress  $\sigma_n$  of the workpiece material, as shown in equation 4-17:

$$\tau_f = \frac{H_V}{0.07} \tanh\left(\frac{\mu\sigma_n}{H_V/0.07}\right) \rightarrow \tau_f = m\tau_f \tanh\left(\frac{\mu\sigma_n}{m\tau_Y}\right) \quad 4-17$$

Moreover, some studies assumed frictionless contact between the tool and the workpiece [119-121]. However, due to the importance of friction in the metal cutting simulation, using friction models is very important to accurately define the interaction between the tool and the workpiece.

## 4.7 Finite element modeling of machining with rotary tools

### 4.7.1 Model geometry and meshing

Three different models can be used to simulate the metal cutting process: Lagrangian, Eulerian, and arbitrary Lagrangian-Eulerian (ALE). Many previous researchers have

used a predefined chip geometry to simulate the orthogonal machining process using Lagrangian, Eulerian, and ALE [122-125]. However, a predefined chip geometry can not be used in the current model as it is a complex process, and the prediction of the 3D chip shape can not offer a realistic simulation. Therefore, the Lagrangian model was used in the current simulation, where the mesh follows the geometry material, and hence there is no need to predefine the chip in the workpiece geometry domain. For the sake of validation, the current model is followed by the experimental work that was done by Li and Kishawy [85].

A typical cutting tool consists of a rotary insert and a tool holder was used during the experimental work. The insert was mounted over the tool holder by using a radial bearing. The rotary insert diameter was 27 mm with a rake and flank angle of  $0^\circ$ . The tool holder has been used to set an inclination angle of  $17^\circ$ , rake angle of  $-5^\circ$ , and flank (or clearance) angle of  $5^\circ$ . In the current model, the insert's geometry was only considered to simplify the model. However, the same angles have been assigned to the insert to match the experiment case. The rounded cutting edge is used to simulate a more realistic case with a higher degree of accuracy. The total number of elements of the tool was 97353, while the total number of nodes was 79672. The tool domain was meshed by coupled displacement-temperature linear hexahedral (C3D8RT) and tetrahedral (C3D4T) elements. Figure 4-6 illustrates that the elements mesh size is very fine within and around the expected contact area between the chip and the tool. That's mainly to capture the changes and distributions of the properties in that interesting area. Besides, the coarse element's size is used to discretize the rest of the tool domain to reduce the computational time by using a relatively low number of elements without affecting the solution accuracy. The insert was considered as a rigid body. Table 4-1 represents the material properties of the uncoated carbide tool, which were used in the simulation.

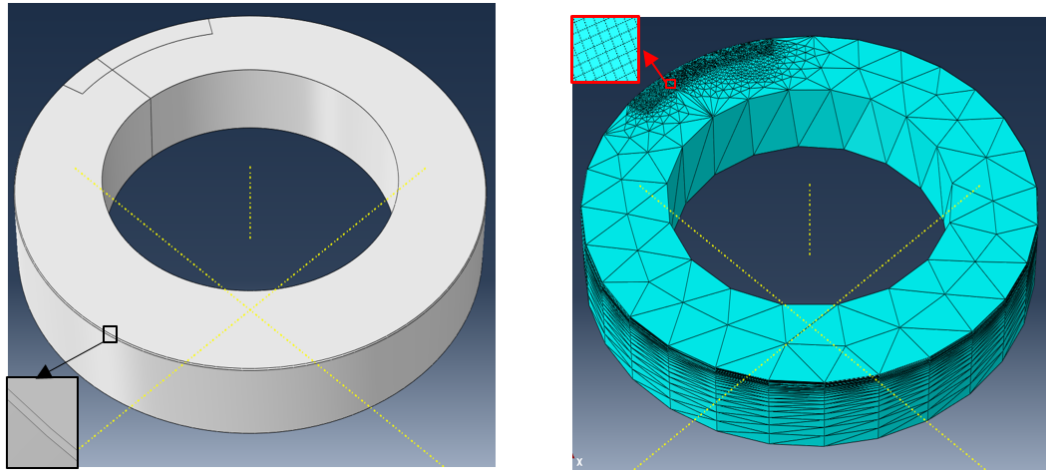


Figure 4-6. Rotary insert geometry and mesh

Table 4-1: Properties of the uncoated carbide [126]

Properties	Value
Thermal conductivity	$50 \text{ Wm}^{-1} \text{ C}^{-1}$
Specific heat	$400 \text{ J kg}^{-1} \text{ C}^{-1}$
Density	$11900 \text{ kg m}^{-3}$
Young's modulus	534 GPa
Poisson's ratio	0.22
Expansion coefficient	$6.3\text{e}^{-6}$

A hollow cylinder with an outer diameter of 48 mm and a wall thickness of 2 mm was used as a workpiece in the experimental work. The developed workpiece domain was 5 mm length, 2 mm width, and 0.6 mm depth. The width of the model domain was selected as 2 mm to match the width of cut of the workpiece, while the height of the model was selected as 0.6 mm which is three times of the highest used feed (i.e., 0.2 mm/rev) since the variation of the measured characteristics is expected to occur only within this distance beneath the newly generated surface. Besides, the length of the model was selected as 5 mm because it was noticed that the steady-state characteristics

such as cutting forces, tool rotational speed and heat flux were satisfied within this length.

Regarding the workpiece meshing, structural elements have been used to discretize the workpiece domain to minimize the numerical errors. The total number of elements was 214650, while the total number of nodes was 228312. The workpiece domain was meshed by a coupled displacement-temperature linear hexahedral (C3D8RT) elements. A relatively fine element size was used within a distance equals to double the feed value. Therefore, the chip and the area under the newly generated surface can have a fine mesh. Figure 4-7 (left-side) shows the workpiece mesh, while Figure 4-7 (right-side) presents the assembly of the tool and the workpiece. The angles are assigned to match the experimental setup.

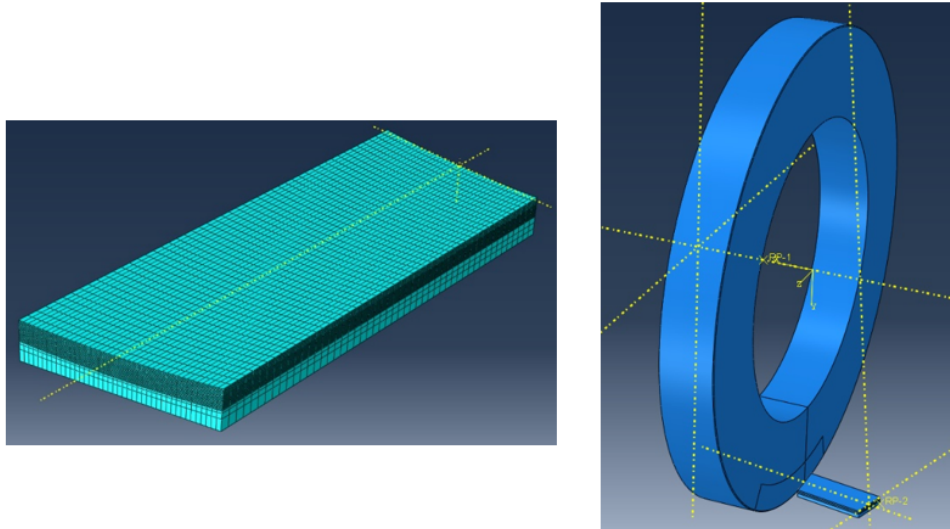


Figure 4-7. Workpiece geometry and mesh (left-side), tool-workpiece assembly (right-side)

## 4.7.2 Material behavior

In this study, a workpiece made of carbon steel AISI/SAE 1045 is used. Table 4-2 presents the workpiece chemical composition. The Johnson-Cook model is utilized as a plastic model in order to define the plastic behavior of the workpiece. This model is widely used in the metal cutting simulation due to its ability to consider the effect of the strain rate and temperature on the stress. AISI/SAE 1045 steel properties and Johnson-Cook equation parameters are listed in Table 4-3.

Table 4-2. AISI/SAE 1045 chemical composition [85]

Carbon (C)	Manganese (Mn)	Phosphorus (P)	Sulfur (S)	Iron (Fe)
0.43–0.50%	0.60—0.90%	0.04%	0.05%	balance

Table 4-3. Mechanical properties and Johnson–Cook parameters for AISI 1045 steel [127]

Properties	Notation	Value
Thermal conductivity	$k$	$38 \text{ Wm}^{-1} \text{ C}^{-1}$
Specific heat	$c$	$420 \text{ J kg}^{-1} \text{ C}^{-1}$
Density	$\rho$	$7800 \text{ kg m}^{-3}$
Young’s modulus	$E$	200 GPa
Poisson’s ratio	$\nu$	0.3
Initial yield stress	$A$	553 MPa
Hardening modulus	$B$	600 MPa
Strain sensitivity parameter	$C$	0.0134
Strain hardening index	$n$	0.234
Reference temperature	$T_{\text{ref}}$	20 °C
Melting temperature	$T_{\text{melt}}$	1460 °C
Thermal softening coefficient	$m$	1
Reference strain rate	$\dot{\epsilon}_0$	$1 \text{ s}^{-1}$

### 4.7.3 Chip formation modeling

Johnson-Cook failure model was used to simulate the separation of the chip from the workpiece by using the element deletion approach. When the workpiece is fed towards the cutting tool, the contact stress can be noticed, and the workpiece elements start to be compressed. Afterward, the damage initiates in some elements, and the behavior of the material is no longer following the plastic model. After damage initiations, the failure model is used to control the material behavior and delete the elements in which the “damage evaluation” criteria are reached. It is worth mentioning that Johnson-Cook failure model is suitable for cases associated with high strain rate deformation such as metal cutting processes. The values of Johnson-Cook failure model constants are specified in Table 4-4.

Table 4-4. Johnson–Cook damage parameters for AISI 1045 steel [128]

Damage model parameters	Value
D1	0.06
D2	3.31
D3	-1.96
D4	0.0018
D5	0.58

In the current work, Coulomb’s friction model is used as the friction model between the tool and the workpiece. The surface contact method is used to define the friction coefficient  $\mu$  between the chip and the tool. The coefficient of friction was tuned for each test in order to obtain the best agreement with the experimental forces. The contact type (i.e., sticking or rolling) can be estimated by ABAQUS based on the contact stress value between the tool and the chip.

#### 4.7.4 Model validation and discussion

For the sake of validation, four reference tests were selected to compare the experimental and predicted results. The cutting conditions for these four tests are listed in Table 4-5. These specific tests were selected to cover the experimental conditions ranges. A comparison between the experimental and numerical forces (i.e., cutting and radial forces) is shown in Figure 4-8. The force suddenly increases when engaging with the workpiece and then fluctuates around an average value, which is used for the comparison. The model shows a good agreement compared to the experimental results with a model's accuracy of about 91.3 %. The deviation between the experimental and numerical results could be due to the numerical errors, experimental human errors (i.e., the tool is not exactly centered in the middle of the tube thickness), and measuring device uncertainties.

Table 4-5. Validation tests cutting conditions

Test number	Feed (mm/rev)	Cutting speed (m/min)
1	0.1	120
2	0.125	170
3	0.15	230
4	0.2	170

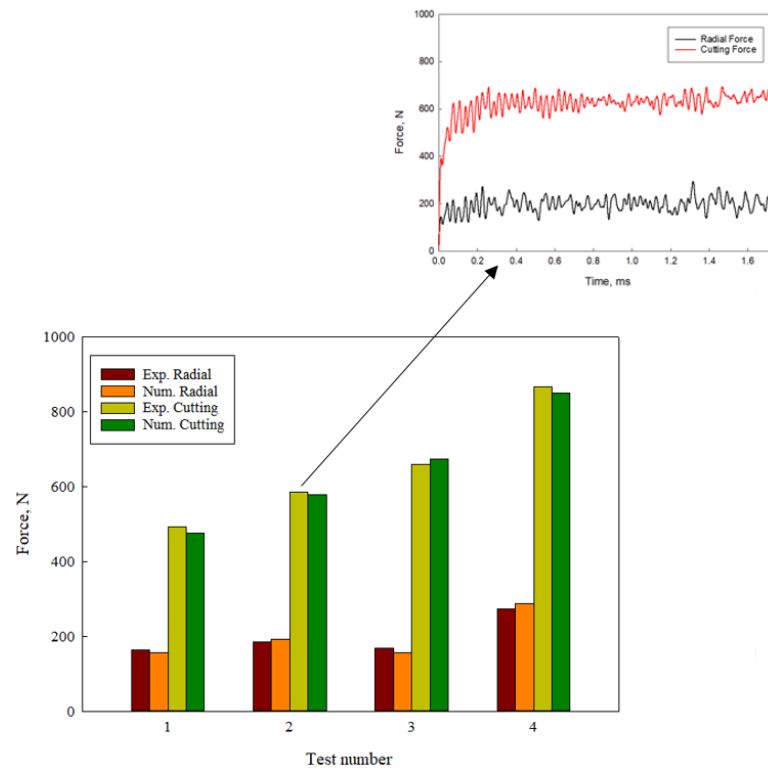


Figure 4-8. A comparison between the predicted and experimental [85] forces

Figure 4-9 shows a comparison between the model and experimental chip morphology results. It can be noticed that the model chip shape shows a good agreement with the experimental chips in terms of chip curling pitch and chip edge shape.

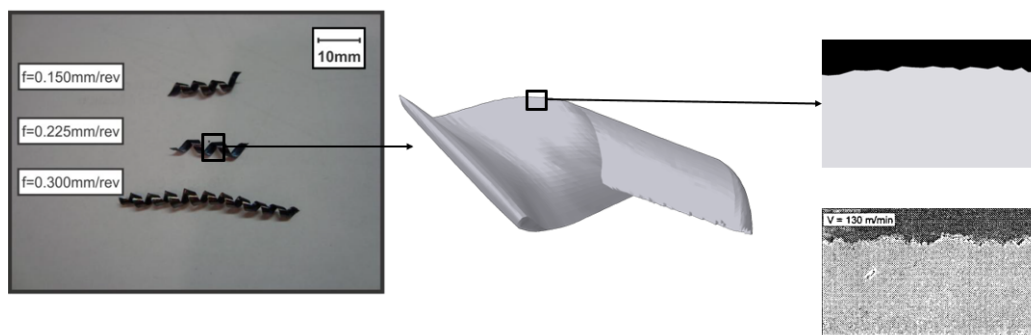


Figure 4-9. A comparison between the simulated chip morphology and experimental chips images at 130 m/min cutting velocity and 0.225 mm/rev feed rate: left is the chip's image obtained by Parker [129] and right is the ESM image obtained by Zhang [130]

Another indicator that can be used for comparison between the simulation and experimental results is the chip flow angle. Figure 4-10 shows a comparison between the predicted and experimental chip flow angle. The result shows that the model can predict the chip flow angle with an accuracy of around 92 %. Since this is an oblique cutting operation, the friction force should have an angle with the tool axis (chip flow angle), and accordingly, there is a tangential component of the friction force guides the tool to rotate in the proper direction.

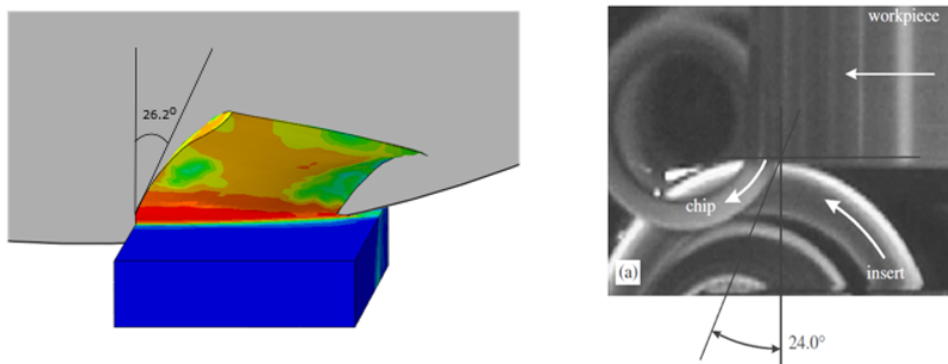


Figure 4-10. A comparison between the predicted and experimental [84] chip flow angle at 230 m/min cutting speed and 0.2 mm/rev feed rate

# Chapter 5: Cutting temperature hybrid model

## 5.1 Preamble

The generated heat is one of the main concerns during the metal cutting processes. That is because many economic and technical issues are directly or indirectly related to the generated heat. This heat is generated due to the plastic deformation at the primary shear zone, friction between the tool and the chip at the secondary shear zone, and the friction at the tertiary zone, as shown in Figure 5-1. As the properties of the materials highly depends on temperature; thus, the stress, strain, and temperature should be captured simultaneously by a coupled temperature displacement model. In such a model, the temperature in each element is calculated directly using the energy balance equation. However, some of the previous studies were developed based on the adiabatic assumption [131, 132]. The adiabatic assumption cannot be used when the residual stress is one of the required outputs. That is because the cooling process at room temperature should be considered to capture the residual stresses [133].

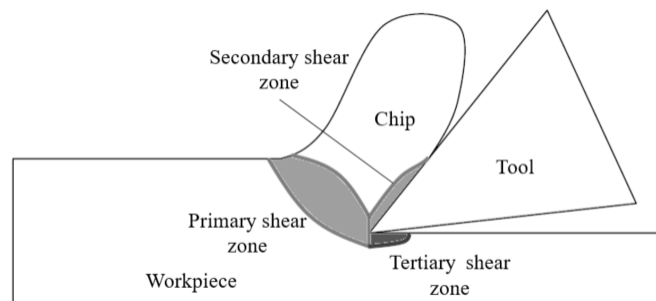


Figure 5-1. Heat generation in metal cutting

The generated heat during the metal cutting process influences the tool and the workpiece materials properties. The high temperature in the cutting zone can lead to thermal softening of the tool material; therefore, the tool wear rate increases, and permanent damage of the cutting insert may occur. As a result, the tool life and the product accuracy decrease, which leads to an increase in the machining cost and time.

Many methods can be used to solve the temperature issue. Flood coolant is widely used to dissipate the generated heat to keep the cutting zone temperature within acceptable limits. However, using flood coolant increases the machining cost and causes high harmful effects on the environment and human health. Therefore, machining with self-propelled rotary tools can be a suitable alternative. That is because of the ability of the rotary tools to machine difficult to cut materials with acceptable tool life, even under dry conditions. This chapter is aimed to model and investigate the temperature characteristics when machining using self-propelled rotary tools.

## **5.2 Hybrid modeling approach: stages and methodology**

Few studies have been done to numerically model and investigate the self-propelled rotary tool temperature field. All of them have used an analytical approach to estimate the model boundary conditions (for example, the generated heat at the secondary shear zone, the contact area between the tool and chip, and the heat partition factor). Generally, these analytical models are developed based on different assumptions, which may lead to a large deviation between the models and experimental values. In the current work, this issue is avoided by using a purely numerical approach, which only requires prior knowledge of the used materials properties and applied operating conditions to simulate the cutting process. Ma et al. [134] developed a finite element model to simulate the corner up milling process of Ti-6Al-4V using AdvantEdge software. Due to the high computational time, a separate FEM numerical model using ABAQUS was used to analyze the heat transfer process. Similarly, in the current work, two separate phases are employed in order to study the steady-state temperature field

during machining with a SPRT. In the first phase, Finite Element Modeling (FEM) which is based on a material plastic model, damage model, and friction law is utilized to simulate the cutting process using SPRT. ABAQUS/Explicit commercial package is employed in the first modeling phase, where a 3-D coupled temperature-displacement domain is solved. The simulation results in terms of cutting forces, heat flux, temperature, chip morphology, and the contact area between the chip and tool are obtained. To provide a steady-state temperature distribution, more than one tool revolution should be simulated. However, that's not easy to be achieved using ABAQUS due to the high computational time. Hence, the second modeling phase is utilized to investigate the SPRT steady-state temperature.

In the second phase, the 3-D domain for the cutting tool is built, and a moving heat source is considered within the energy equation. COMSOL software is utilized in the second phase modeling. The obtained results from ABAQUS (i.e., the contact area, the heat flux, and the tool rotational speed) are used as boundary conditions for the tool model. Finally, the 3-D steady-state temperature field is determined using this proposed hybrid model. Figure 5-2 shows the flow chart for the proposed model.

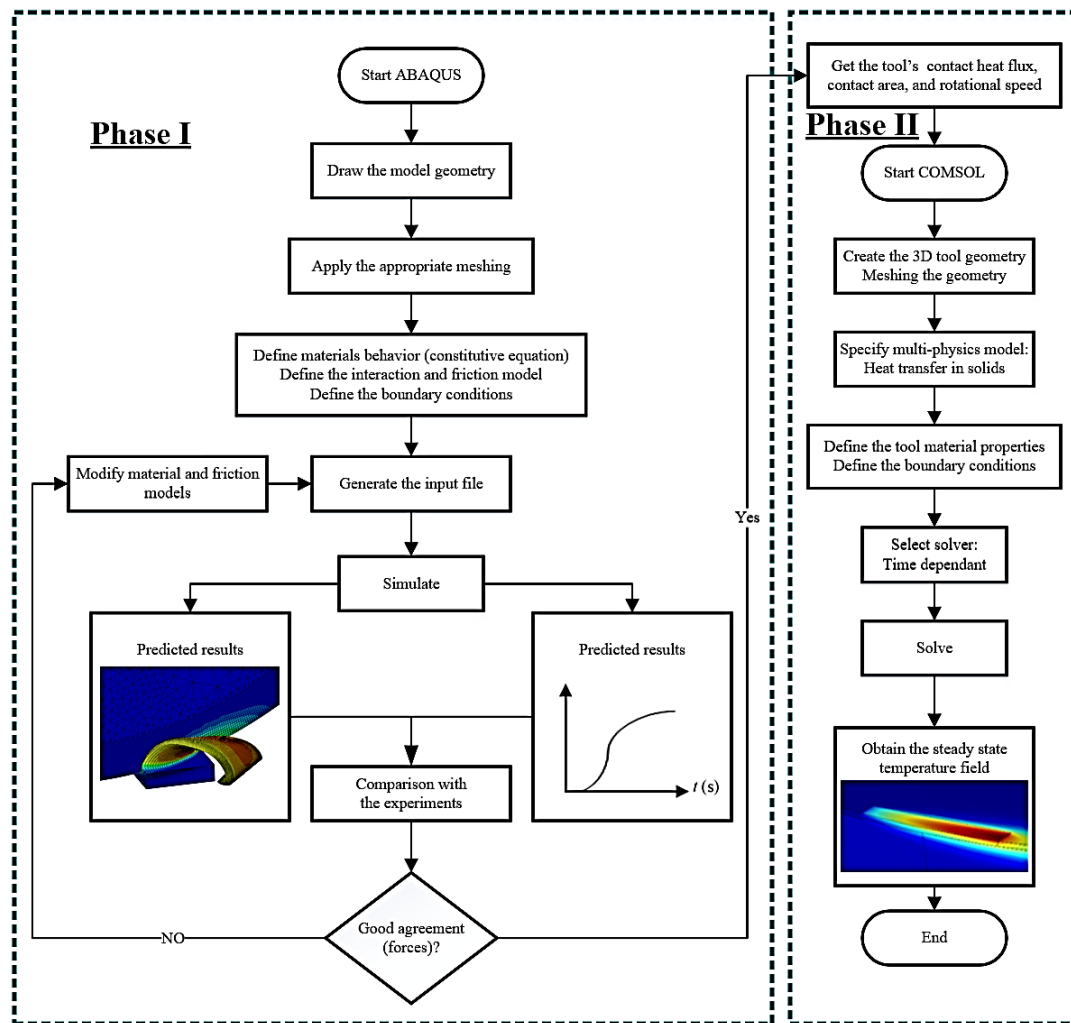


Figure 5-2. Hybrid model flowchart

### 5.3 Phase II: heat transfer modeling

In this phase, the tool geometry with a moving heat source is used to consider the heat flows into the tool. This model follows the same steps presented by Dessoly et al. [135]. However, a rounded cutting edge is considered in the tool geometry to achieve a more realistic model. The moving heat source is considered in the equation 5-2 by adding a convective flux term “ $\rho c \vec{V} T$ ” to the conductive heat equation (equation 5-2).

$$\rho c \frac{\partial T}{\partial t} - k \nabla^2 T = \dot{Q} \quad 5-1$$

$$\rho_t c_t \frac{\partial T}{\partial t} + \nabla \cdot (-k_t \nabla T + \rho_t c_t \vec{V} T) = \dot{Q} \quad 5-2$$

where  $\rho_t$  is the tool density,  $c_t$  is the tool's specific heat capacity,  $k_t$  is the tool thermal conductivity,  $\vec{V}$  is the velocity vector, and  $\dot{Q}$  is the volume heat source. The moving heat source is applied as a boundary condition in the contact area. Thus, there is no need to use the volume heat source  $\dot{Q}$ . The Cartesian velocity vector can be obtained using the cross product of the rotational speed vector  $\omega$  to the displacement vector  $\vec{r}$  as shown in equation 5-3; knowing that, the tool has only a rotational speed  $\omega_t$  around z-direction. Based on that, the energy equation can be solved in the Cartesian coordinates (i.e., x, y, and z). The energy equation is further simplified by using the conservative of mass equation (see equation 5-4). Finally, Equation 5-5 is numerically solved to provide the temperature distribution inside the tool domain.

$$\vec{V} = \omega_t \begin{pmatrix} -y \\ x \\ 0 \end{pmatrix}_{i,j,k} \quad 5-3$$

$$\frac{\partial \rho_t}{\partial t} + \nabla \cdot (\rho_t \vec{V}) = 0 \quad 5-4$$

$$\rho_t c_t \frac{\partial T}{\partial t} - \nabla \cdot (k_t \nabla T) = \rho_t c_t \omega_t (y \frac{\partial T}{\partial x} - x \frac{\partial T}{\partial y}) \quad 5-5$$

## 5.4 Mesh and boundary conditions

Figure 5-3 shows the domain and boundary conditions that were used for the COMSOL model. The boundary conditions include the heat flux rate at the contact area and

convection heat flux with a heat transfer coefficient of  $100 \frac{W}{m^2K}$  for the outer surfaces [62]. Besides, isolated boundary conditions for the inner surfaces are applied. The heat flux of the contact area is directly obtained from the ABAQUS model. Hence, there is no need for the heat partition factor. The contact area between the chip and the tool is considered as can be seen in Figure 5-3 (left-side), where  $l$  the tool-chip is contact length and  $w$  is the width of the cut. Accurate contact area dimensions are also obtained from the ABAQUS model, and it is neither a comma [62] nor a triangle [135, 136] because it is a tube end turning process. It should be stated here that as the moving heat flux applied, the moving mesh function utilized, which displaces the mesh nodes inside the bulk of the solid. In other words, the mesh nodes are rotating while the bulk of the solid is stationary.

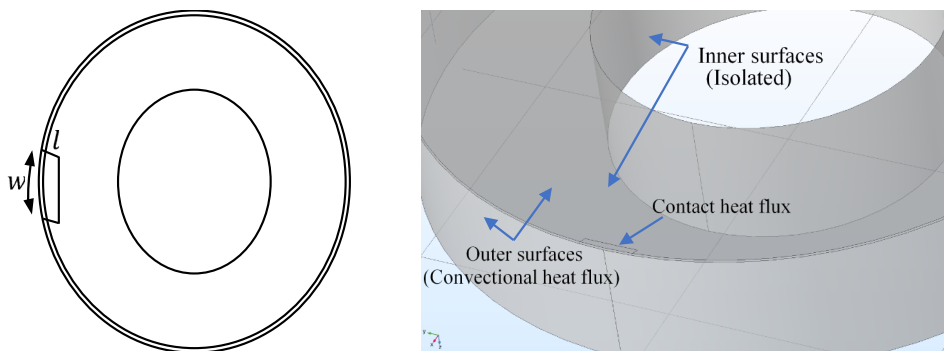


Figure 5-3. COMSOL tool model geometry

Figure 5-4 represents the domain's mesh, where the total number of elements is 20144. Mixed-element types include hexagonal and tetrahedral are used. Hexagonal fine elements are utilized in the contact area to accurately capture the temperature characteristics inside and around this area of interest. Tetra coarse elements are used to discretize the rest of the domain. The element size gradually increases from fine to coarse with a transition factor of 1.2.

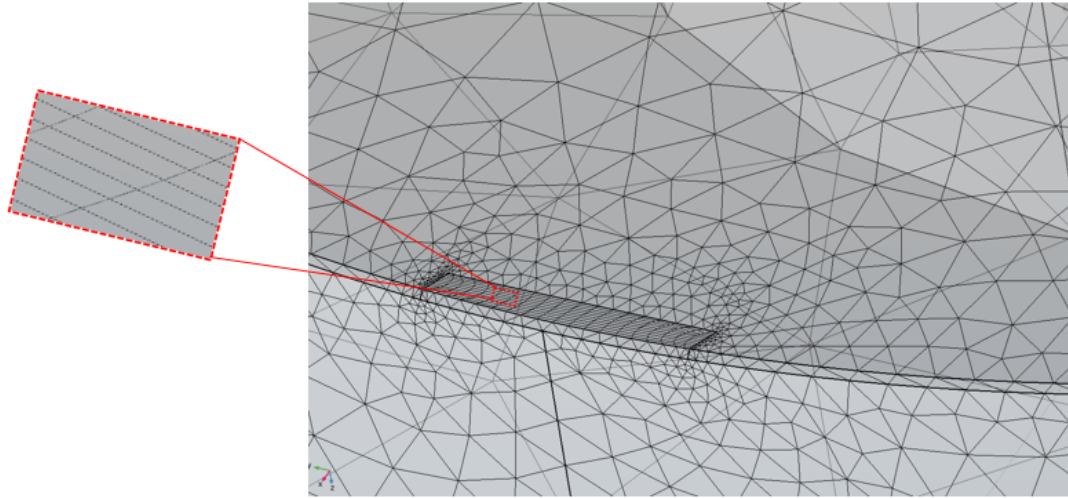


Figure 5-4. COMSOL tool model mesh

## 5.5 Temperature model results and discussions

Figure 5-5 illustrates the temperature distribution for the tool and the workpiece after 3 ms of cutting time. This result was obtained using ABAQUS. It can be noticed that the maximum temperature was observed in the tool-chip interface area (secondary shear zone) as expected. Furthermore, the chip temperature is relatively high, which indicates that a large amount of heat goes directly to the chip. Besides, the tool temperature increases in the direction of the tool rotation as the heat is carried away from the cutting zone by the tool motion. Furthermore, it is observed that all the interesting areas such as the contact area, chip, and near the surface area have a fine mesh as designed, which confirms the capability of the model to capture results' influence in these important regions.

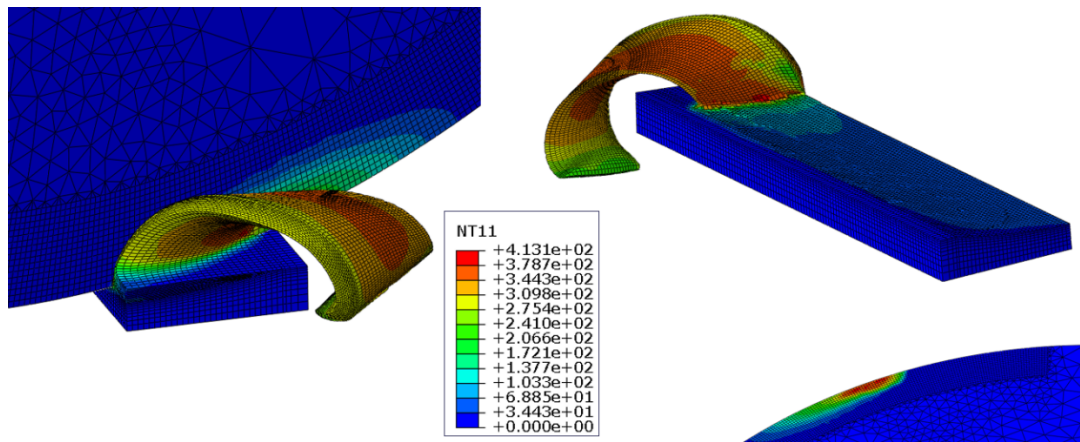


Figure 5-5. Rotary tool predicted temperature distribution (in °C) at 170 m/min cutting speed and 0.2 mm/rev feed rate

To investigate the benefits of the tool rotary motion, a fixed case is solved to compare the temperature field with a rotating case. Figure 5-6 represents the temperature distribution on the tool rake face for fixed and rotating cases. Figure 5-7 shows a comparison between the spatial average tool temperature at the contact area of the rotary and fixed tool. It can be seen that the average temperature difference between the fixed and rotating tools are about 65 degrees. Consequently, the tool's rotary motion reduced the tool temperature by about 15 %. This observation is in agreement with the result that is obtained by Dessoly et al. [135]. Besides, It can be seen that the heat is concentrated around the cutting zone in the fixed tool case, and slowly propagating by conduction to the rest of the tool material. While, the temperature is relatively high in a large tool area in the case of the rotating tool, as the heat is moving with the material flow. In addition, the contact length seems to be shorter in the rotary tool case compared with the fixed one. That might be attributed to the change in the chip flow angle and chip relative velocity as a result of tool motion.

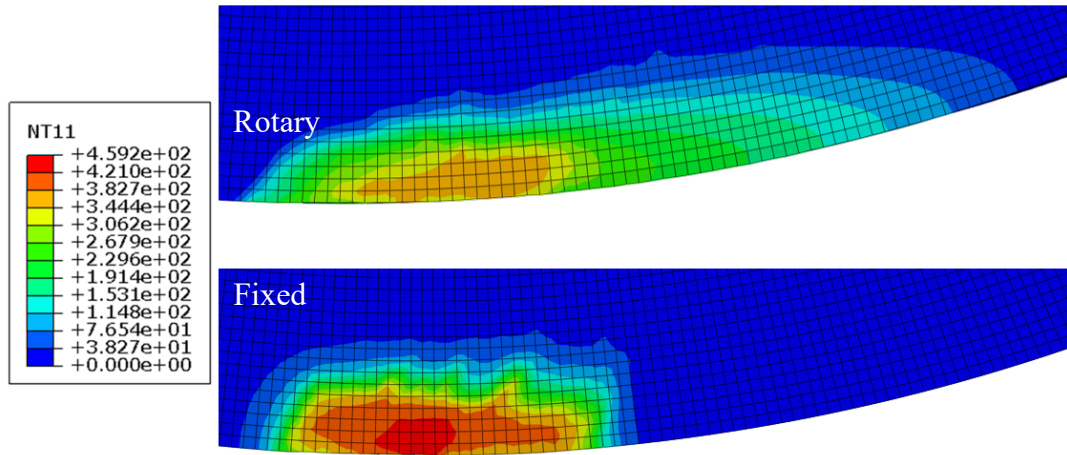


Figure 5-6. Temperature distribution over the rake face for fixed and rotating cases (in °C) at 170 m/min cutting speed and 0.2 mm/rev feed rate

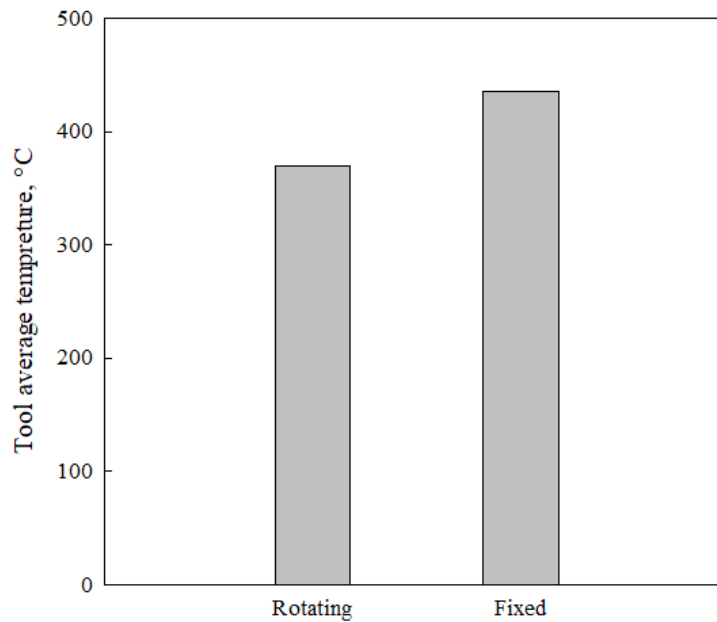


Figure 5-7. Average tool temperature for fixed and rotating cases (in °C) at 170 m/min cutting speed and 0.2 mm/rev feed rate

Figure 5-8 shows the temperature pattern at an intermediate cross-section of fixed and rotary tool cases. The maximum temperature in the case of a fixed tool occurs inside the chip core and expands towards the cutting tool rake face (secondary shear zone).

This observation is expected and noticed in many previous studies. While in the rotary tool case, the maximum temperature is observed in the core of the chip, and it is not observed or extended at the tool chip interface. It is worth mentioning that this is a new observation, which occurs as the generated heat in the secondary shear zone is continuously removed by the tool rotational motion.

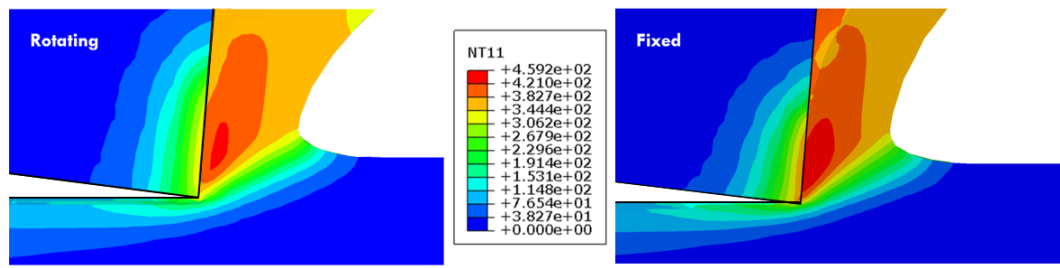


Figure 5-8. Temperature pattern at an intermediate cross-section plane of fixed and rotating cases (in °C) at 170 m/min cutting speed and 0.2 mm/rev feed rate

As mentioned before, the steady-state tool temperature can be obtained by using a combination of ABAQUS and COMSOL software. For example, Figure 5-9 shows the average heat flux of the tool/chip interface area at a cutting velocity of 170 m/min and feed rate of 0.2 mm/rev. The average value of the heat flux is obtained from the ABAQUS and then used in the COMSOL as a constant heat flux at the contact area. Figure 5-10 shows the 3-D steady-state temperature distribution, which is obtained using COMSOL for the cutting tool after 10 revolutions. It can be seen that the tool rotational speed of that case offers a suitable time for each portion of the cutting edge to cool enough before engaging again with the workpiece.

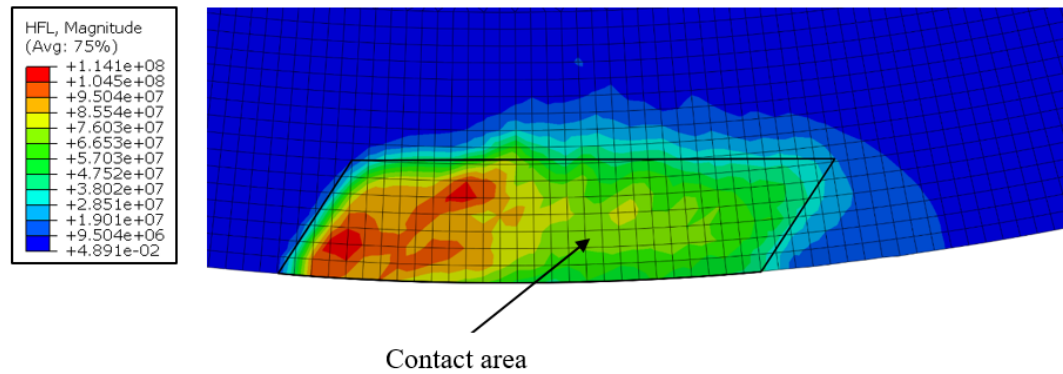


Figure 5-9. Heat flux distribution over the rake face (in  $\text{w/m}^2$ ) at cutting speed of 170 m/min cutting speed and feed rate of 0.2 mm/rev

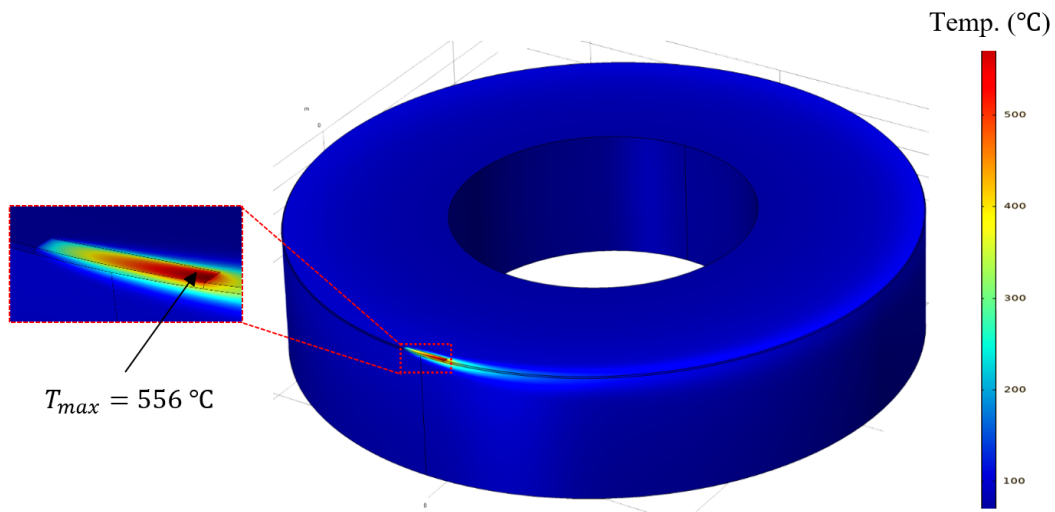


Figure 5-10. COMSOL tool temperature distribution (in  $^\circ\text{C}$ ) at 170 m/min cutting speed and 0.2 mm/rev feed rate

To investigate the effect of the tool rotational speed on the temperature behavior, Figure 5-11 shows the temperature influence over the tool rake face for four different cases. As can be seen, the temperature's peak is observed at a shifted distance from the cutting edge in all cases. The maximum temperature was noticed in the fixed case as expected. As the tool rotational speed increases, the peak temperature as well as the tool bulk temperature decrease. However, the temperature increases again at relatively higher

tool rotational speeds (e.g., 900 rpm). That's because increasing the tool rotational speed beyond a certain value will lead to reducing the cooling time for each portion of the cutting edge. Consequently, that could lead to a noticeable increase in the tool temperature again. Thus, the tool rotational speed should be optimized, by changing the inclination angle  $i$ , to achieve all possible advantages of the tool motion. Moreover, for the fixed case, the temperature gradually decreases while moving away from the contact area as the heat slowly moves by conduction towards the cutting tool center. While, in rotating cases, the temperature of the tool highly decreases after the contact area and almost remains constant beyond it. That is because the largest portion of the heat is quickly carried away by the material flow.

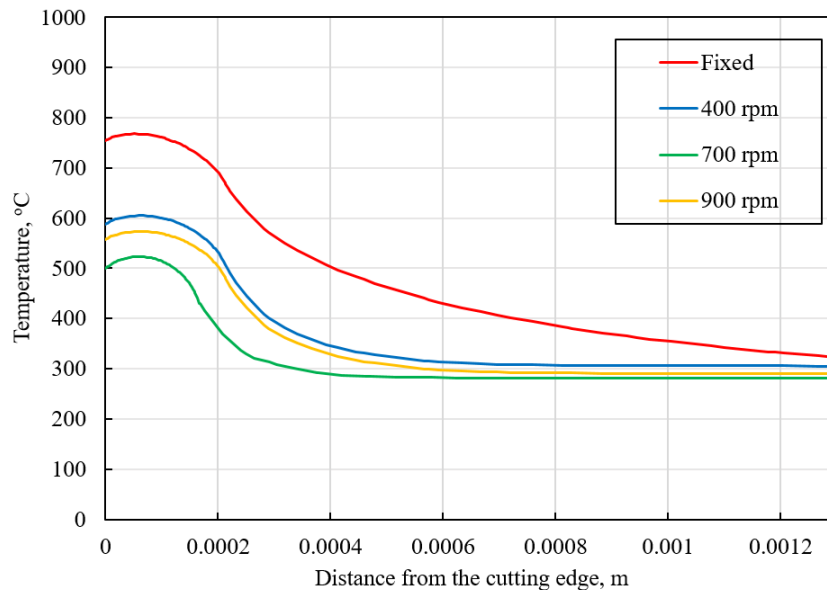


Figure 5-11. The temperature influence over the tool rake face for four different cases

Figure 5-12 shows the temperature history for a point on the cutting edge. It can be observed that the steady state temperature was almost reached after 10 revolutions. Besides, the temperature of the point rapidly increases when it is engaged with the workpiece during a short time. Then, the point temperature decreases as it is disengaged and moved away from the cutting zone. As a result of the tool rotational motion, this

process is repeated during the cutting process and offering a heating-cooling cycle for each portion of the cutting-edge circumference. Not only temperature decreases in the rotating case compared to the fixed case, but also the high temperature at the cutting zone affects each portion of the cutting edge for a relatively short time, as can be seen in Figure 5-12. That will prevent the tool from crater wear, as observed by Kishawy et al. [61].

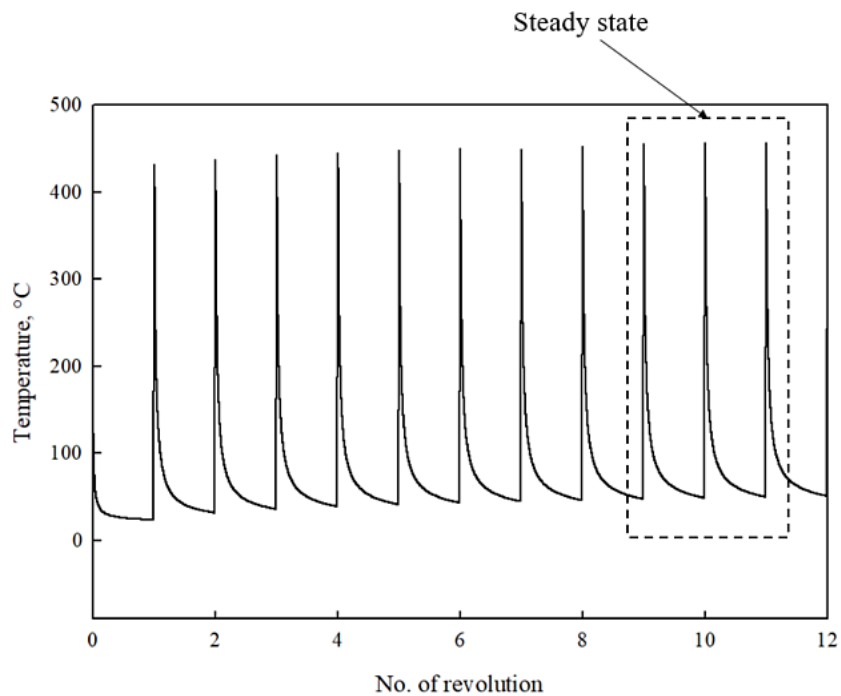


Figure 5-12. Tool temperature history of a point on the cutting edge at 170 m/min cutting speed and 0.2 mm/rev feed rate

## 5.6 Mechanism of machining with SPRT

**Error! Reference source not found.** Figure 5-13 shows a schematic of machining using the self-propelled rotary tool; the mechanism of the rotary tool can be concluded as follows:

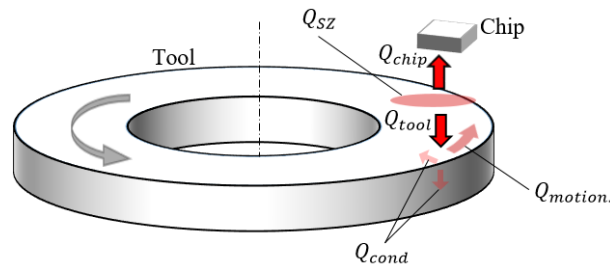


Figure 5-13. Schematic of machining using a rotary tool

- The heat is generated at the secondary heat zone ( $Q_{SZ}$ ) as a result of the friction between the chip and the tool;
- Part of the generated heat is going to the chip ( $Q_{chip}$ ), while the rest of the generated heat is going to the tool ( $Q_{tool}$ );
- Many factors control the secondary shear zone heat partitioning process (i.e.,  $Q_{tool}$  and  $Q_{chip}$ ), these factors include tool and workpiece materials, cutting speed, feed rate, and tool inclination angle (i.e., tool rotational speed);
- The amount of heat which is going to the chip ( $Q_{chip}$ ) should be maximized to reduce the heat portion of the tool ( $Q_{tool}$ );
- The amount of heat which is going to the tool ( $Q_{tool}$ ) should be efficiently dissipated to prevent the tool temperature from reaching excessive levels, which accelerates the tool wear rate and reduces the tool life;
- Part of this heat is transferred by conduction ( $Q_{cond}$ ), while the highest part is carried away from the cutting zone by the tool motion ( $Q_{motion}$ );
- Each portion of the cutting tool edge is engaged with the workpiece for a relatively short time when its temperature starts to be increased. After that, this portion is disengaged and moved away to cool down before engaging again with the workpiece;
- Therefore, the generated heat is efficiently distributed on the whole tool bulk material instead of being concentrated in and around the cutting zone as occurs with conventional tools;

## Chapter 5: Cutting temperature hybrid model

- According to that, the cutting zone temperature is always kept within an acceptable range to prevent the tool damage;
- Besides, the tool motion allows the tool wear to be distributed over the whole round edge instead of being concentrated at a single point, as occurs in the conventional tools, which dramatically increases the tool life.

# Chapter 6: Experimental setup

## 6.1 Preamble

This chapter provides detailed information about the carried out experiments. The main objective of the experiments is to investigate the performance of the self-propelled rotary tools when machining hardened steel under dry environment. Cutting forces, surface roughness, tool wear, tool rotational speed, and temperature are recorded and investigated. The experiments were performed on Standard Modern N/C 17 lathe (10 HP). The used materials, measuring equipment, and the experimental plan are presented in this chapter.

## 6.2 Materials and Methods

The workpiece material used in this study is AISI 4140 steel. A tube shape workpiece with an inner diameter of 50 mm and an outer diameter of 100 mm is used, as shown in Figure 6-1. The workpiece is hardened to  $46 \pm 2$  HRC, and the tube shape of the workpiece helps to have homogeneous properties during the heat treatment. The chemical composition, mechanical, and thermal properties of the workpiece is shown in Table 6-1.

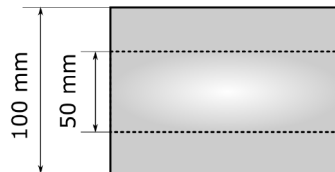


Figure 6-1. Tube shape workpiece

Table 6-1. AISI 4140 steel properties [137]

---

Chemical composition (wt.%): C: 0.38%-0.43%, SI: 0.15%-0.3%, Mn: 0.7%-1%, Cr: 0.8%-1.1%, Mo: 0.15%-0.25%, Fe: 96.75%-97.84%
Density: 7850 Kg/m <sup>3</sup>
Young's modulus (at 25 °C): 198 GPa
Poisson's ratio (at 25 °C): 0.3
Tensile strength: 729.5 MPa
Yield strength: 379.2 MPa
Specific Heat (at 25 °C): 470 J/kg °C
Thermal Conductivity (at 25 °C): 42.7 W/m °C

---

The tool insert is made of carbide with an outer diameter of 27 mm. The insert is properly mounted over the tool holder, and a rake angle of  $-5^\circ$  with a flank angle of  $5^\circ$  was used. The tool holder allows adjusting certain inclination angles;  $5^\circ$ ,  $10^\circ$ ,  $15^\circ$ ,  $20^\circ$ , and  $25^\circ$ . Figure 6-2 shows the experimental setup used in this study.

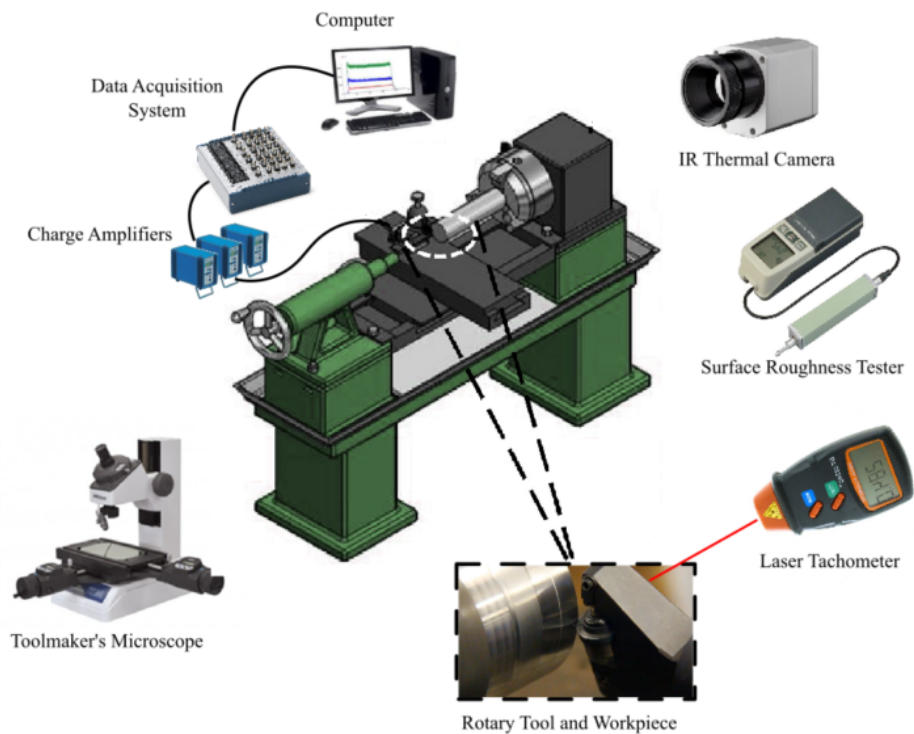


Figure 6-2. Schematic of the experimentation setup for machining with a self-propelled rotary tool

### 6.3 Force measurements

Kistler 9251 A dynamometer was used to capture the signals of the three force components. The captured signals were then connected to the National Instrument data acquisition (NI USB-6221 BNC) through three Kistler (KCA5010B) charge amplifiers. Three data cables were used between the dynamometer sockets and the charge amplifiers. The output signals from the amplifiers were connected to the data acquisition channels by three signal cables. The data acquisition was then connected to the computer using a single USB cable. The forces were read and recorded at a rate of 30 Hz using the LabView software. A low pass filter was applied to the data to remove any signal noises, and average values were obtained and used in the analysis. Figure 6-3 shows the used equipment for force measurements.

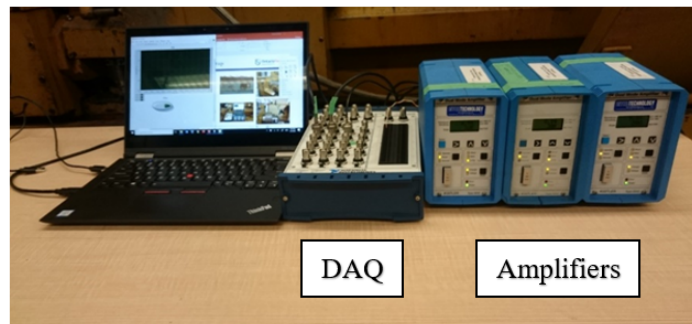


Figure 6-3. The used equipment for measuring forces

## 6.4 Temperature measurements

Infra-red thermal imaging technique was used to measure the temperature of the self-propelled rotary tool. Different techniques such as the tool-workpiece thermocouple and the embedded thermocouple are not suitable for the rotary tools due to the motion of the insert. The infra-red thermal camera is able to provide a real-time temperature for the cutting zone.



Figure 6-4. Optris PI 640 infra-red thermal camera

Optris PI 640 camera was used in the current study, as shown in Figure 6-4. Three temperature ranges can be adjustable to achieve an accuracy of  $\pm 2$  °C. These ranges are -20°C to 100 °C, 0°C to 250 °C, and 150°C to 900 °C. The third range is selected as the temperature is expected to be higher than 150 °C during the hard turning. The camera frame rate of 40 Hz was utilized. One of the main advantages of the used camera

is the capability of performing self-calibration. The camera was mounted to a fixed beam of the machine in order to achieve good stability. Figure 6-5 shows a sample of temperature measurement. The indicator was set to capture the maximum temperature with time, and the average temperature values were obtained and used in the analysis.

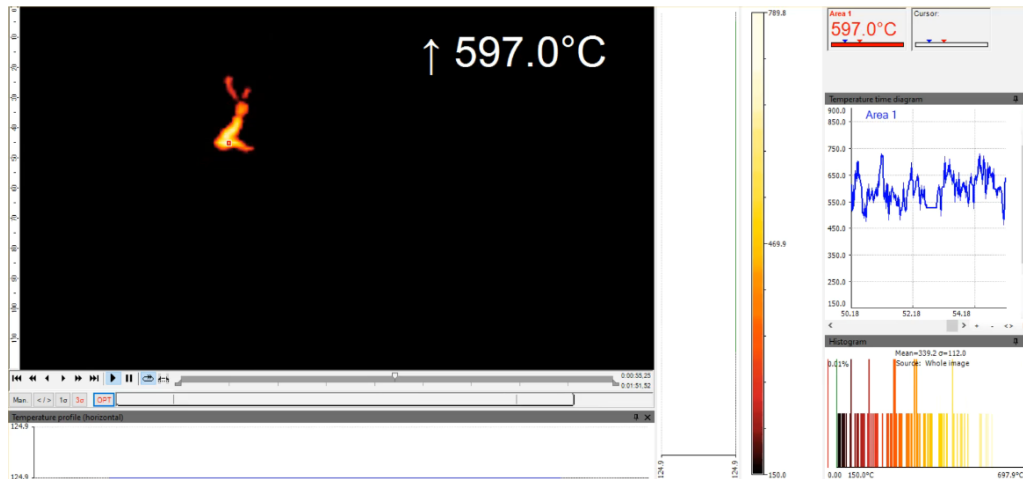


Figure 6-5. A sample of temperature measurement

## 6.5 Surface roughness measurements

The machined surface quality was evaluated using the average surface roughness. Mitutoyo SJ.201 portable surface roughness was used in the current study, as shown in Figure 6-6. Ra is the arithmetic average distance between the mean line and the surface profile irregularities within the measuring length, and it can be used to find the vertical roughness [138]. Ra is a commonly used parameter to measure the surface roughness. Constant cut-off length of 2.5 mm with a speed of 0.25 mm/s is used for all measurements. After every test, the surface roughness is measured in three different locations, and the average value is obtained and used in the analysis.



Figure 6-6. Surface roughness tester (Mitutoyo SJ.201)

## 6.6 Tool wear measurements

After each cutting pass, the flank tool wear was measured using a Mitutoya toolmaker's microscope (TM-A505B), as shown in Figure 6-7. The flank tool wear is occurred due to the high friction between the flank face of the tool and the workpiece. The average flank wear was measured and used in the analysis.



Figure 6-7. Toolmaker microscope (Mitutoyo TM-A505B)

## 6.7 Tool rotational speed measurements

Digital laser tachometer (AGPtek® DT-2234C+) was used to measure the tool's rotational speed during each test, as shown in Figure 6-8. This tachometer is capable of measuring a wide range from 2.5 rpm to 999.9 rpm with a resolution of 0.1 rpm, and  $\pm 0.05\%$  accuracy. Thin silver strips were attached to the insert cartridge, which rotates at the same speed of the insert. The laser beam was then focused to the location of the high reflectivity silver strip to capture the rotational speed in rpm. Three measured values were taken at different times during the test, and the average value was obtained and used in the analysis.



Figure 6-8. Digital laser tachometer

## 6.8 Plan of experimentation

In this study, Taguchi's approach was used in order to perform the minimum number of experiments. Orthogonal arrays are employed in this approach to study how the data statistics (i.e., variance, mean, etc.) are affected by the studied design variables of the

experiments. This method was used to make sure that the optimum level of the design variables is selected to reduce the manufacturing cost without affecting the product quality. The orthogonal array can provide a minimum number of experiments (i.e., a well-balanced number) [139].

Three design variables were selected; cutting speed ( $V$ ), feed rate ( $f$ ), and inclination angle ( $i$ ). The depth of cut was to be constant and equal to 0.2 mm through all experiments. Four levels were assigned for each design variable. Table 6-2 presents the design variables and the assigned levels for each variable. The full array for the current study should be L64OA, as there are three variables, four levels each (i.e.,  $4^3$ ). However, in order to save cost and time, fractional factorial array L16OA was selected. This array consists of 16 rows corresponding to the number of runs, as shown in Table 6-3.

Table 6-2. Assigned level to the design variables

	Level 1	Level 2	Level 3	Level 4
A: $i$ ( $^{\circ}$ )	5	10	15	20
B: $f$ (mm/rev)	0.1	0.15	0.2	0.25
C: $V$ (m/min)	70	127	167	240

The analysis of variation (ANOVA) was then utilized to study the influence of the design variables on the machining performance indicators. This technique is mainly used to detect the most significant variable(s) that affect the studied machining outputs [140]. Besides, the optimum level of each variable can be clearly obtained.

The general steps of the Taguchi's approach and the ANOVA technique can be summarized as follow:

- Define the process
- Define the significant design variables
- Assign the number of levels for each variable
- Select the appropriate orthogonal array

- Perform the experiment runs
- Perform the ANOVA calculations for the required performance indicators
- Analyze the ANOVA results to determine the significant variable and select the optimum level for each variable

Table 6-3. L16OA for the experiment runs

Test #	Inclination angle levels	Feed rate levels	Cutting speed levels
1	1	1	1
2	1	2	2
3	1	3	3
4	1	4	4
5	2	1	2
6	2	2	1
7	2	3	4
8	2	4	3
9	3	1	3
10	3	2	4
11	3	3	1
12	3	4	2
13	4	1	4
14	4	2	3
15	4	3	2
16	4	4	1

The genetic programming (GP) is considered as one of the most effective artificial intelligence techniques, and it is used in many different engineering applications [141]. In genetic programming, each program is built of a tree structure of terminals and functions (i.e., genotype). The terminals (i.e., leaves) are the inputs to the program, and the used functions of the GP program include mathematical functions, programming

functions, and arithmetic operations. Every generated model is presented as a chromosome, and the fitness function is used to evaluate each chromosome. The fitness function measures the error between the model output and the input training data. Genetic operators include mutation, and crossover factors are then utilized to generate new chromosomes. In the open literature, many studies used genetic programming to model the cutting processes [142-144]. In the current study, the Eureka software was used to develop models for the surface roughness and tool wear.

The non-dominated sorting genetic algorithm (NSGA-II) is used in the current study to perform multi-objective optimization of the generated models. The NSGA-II is one of the popular multi-objective optimization techniques as it utilized special features such as fast non-dominated method, fast crowded estimation of distances approach, and simple operator to perform a crowded comparison to find the optimal Pareto-front solutions [145]. The genetic algorithm evolutionary operators such as crossover and mutation are utilized in the NSGA-II algorithm. The general steps of the NSGA-II can be summarized as follows [146]:

- Select the size of the population based on the constraints and their range.
- Perform non-dominated sort for the initialized populations
- Assign crowding distance values for the population individuals
- Select the individuals based on the rank and the crowding distance
- Apply the genetic algorithm crossover and mutation operators
- Recombine and select an individual for the next generation until the population size exceeds the current size

# Chapter 7: Experiments results and analysis

## 7.1 Preamble

This chapter is mainly aimed to experimentally investigate the effect of the inclination angle, feed rate, and cutting speed on the machining performance when using self-propelled rotary tools. The cutting forces, tool wear, temperature, surface roughness, and tool rotational speed were measured and recorded for each run.

Three stages are used to achieve a comprehensive analysis of the machining process using self-propelled rotary tools. In stage one, a mapping matrix is developed to evaluate the performance of each run. Three quality levels are introduced, and their ranges are determined based on the measured values of each performance indicator. This map is useful for the decision-makers in order to select the appropriate run based on the desired objective (i.e., finishing or roughing turning). In stage two, the analysis of variance (ANOVA) is utilized to determine the significant design variables for each performance indicator and select the optimum level of each variable. The last stage is found to perform multi-objective optimization of the machining process. Non dominated sorting genetic algorithm (NSGA-II) is used in this stage. Genetic programming is used to correlate the tool wear and surface roughness to the decision variables. The Pareto-front solutions are then generated and normalized to optimize the solutions based on certain machining scenarios. Finally, confirmation tests are performed to verify the optimized solutions. Figure 7-1 summarizes the experiments methodology of the current research.

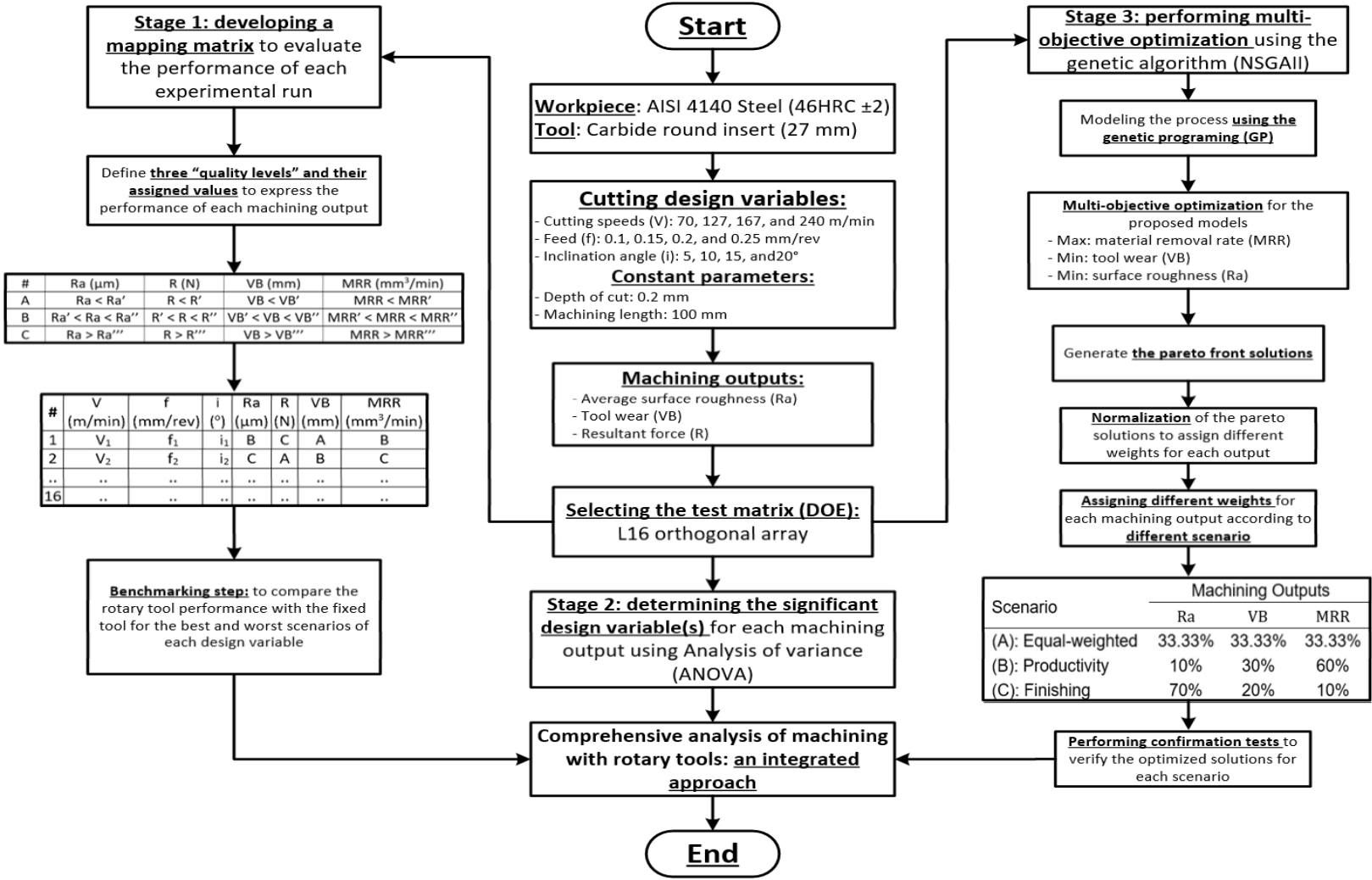


Figure 7-1. Flowchart for the experimental methodology

## 7.2 Mapping matrix results

In this section, a mapping matrix was developed in order to evaluate the performance of each experimental run. Table 7-1 presents the results for the experimental runs. The depth of cut was to be constant and equal to 0.2 mm. The inclination angle  $i$ , the feed rate  $f$ , and the cutting velocity  $V$  were considered as the machining variables, and their values corresponding to each run are shown in Table 7-1. The machining of 100 mm path was performed for each run. The resultant force  $R$ , the flank tool wear  $VB$ , the material removal rate  $MRR$ , and the surface roughness  $Ra$  are selected to evaluate the performance. However, more indicators were measured for each run, such as tool temperature and rotational speed.

Table 7-1. Experimental plan results

	$i$ (°)	$f$ ( $\frac{\text{mm}}{\text{rev}}$ )	$V$ ( $\frac{\text{m}}{\text{min}}$ )	$R$ (N)	$VB$ ( $\mu\text{m}$ )	$Ra$ ( $\mu\text{m}$ )	$MRR$ ( $\frac{\text{mm}^3}{\text{min}}$ )
1	5	0.1	70	176.24	16	0.83	1413
2	5	0.15	127	173.17	38	1.077	3810
3	5	0.2	167	314.2	20	0.78	6680
4	5	0.25	240	386.12	22	0.95	12000
5	10	0.1	127	204.93	61	1.01	2540
6	10	0.15	70	243.28	3	1.13	2100
7	10	0.2	240	242.25	59	0.84	9600
8	10	0.25	167	252.52	14	0.90	8350
9	15	0.1	167	138.81	51	1.18	3340
10	15	0.15	240	186.96	25	0.93	7200
11	15	0.2	70	211.64	5	1.17	2800
12	15	0.25	127	281.07	40	1.48	6350
13	20	0.1	240	183.38	12	0.56	4800
14	20	0.15	167	321.79	71	0.94	5010
15	20	0.2	127	270.91	51	1.11	5080
16	20	0.25	70	253.71	4	1.83	3500

Three quality levels were assigned, and their values were obtained based on the ranges of the result (i.e., minimum and maximum values). Table 7-2 shows the quality levels and their values for each performance indicator. Level A is the best level, and level B is the medium level, while level C is the worst level. The mapping matrix result is

shown in Table 7-3. This result is valuable for the decision-makers in order to quickly select the appropriate run, which is suitable for the desired objectives (i.e., finishing or productivity turning process).

Table 7-2. Quality levels

	R (N)	VB ( $\mu\text{m}$ )	Ra ( $\mu\text{m}$ )	MRR ( $\text{mm}^3/\text{min}$ )
A	$R < 220$	$VB < 25$	$Ra < 1$	$8500 < MRR < 12000$
B	$220 < R < 300$	$25 < VB < 50$	$1 < Ra < 1.5$	$4900 < MRR < 8500$
C	$300 < R < 390$	$50 < VB < 75$	$1.5 < Ra < 2$	$MRR < 4900$

Table 7-3. Tests mapping matrix

	i	f	V	R	VB	Ra	MRR
1	5	0.1	70	A	A	A	C
2	5	0.15	127	A	B	B	C
3	5	0.2	167	C	A	A	B
4	5	0.25	240	C	A	A	A
5	10	0.1	127	A	C	B	C
6	10	0.15	70	B	A	B	C
7	10	0.2	240	B	C	A	A
8	10	0.25	167	B	A	A	B
9	15	0.1	167	A	C	B	C
10	15	0.15	240	A	B	A	B
11	15	0.2	70	A	A	B	C
12	15	0.25	127	B	B	B	B
13	20	0.1	240	A	A	A	C
14	20	0.15	167	C	C	A	B
15	20	0.2	127	B	C	B	B
16	20	0.25	70	B	A	C	C

### 7.3 Cutting forces results and discussion

Figure 7-2 presents the cutting forces results. The results show that the thrust force is the largest force component, followed by the cutting force, and the lowest one is the radial force. The large thrust force is typical and normal for machining such difficult-to-cut material (i.e., hard turning), especially when using a large nose radius (i.e., round insert), as confirmed by Kishawy et al. [147].

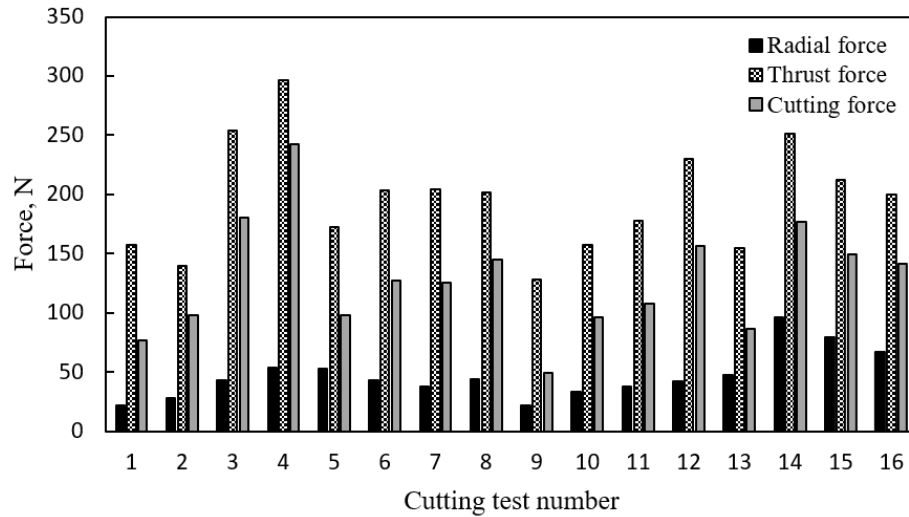


Figure 7-2. Cutting forces results

A sample of the cutting force signal is shown in Figure 7-3. Low pass filter is used to eliminate any unnecessary noise. When the tool engages with the workpiece, a sudden increase in the force occurs, and then the force starts to oscillate around an average value. These average values were extracted and used in the analysis.

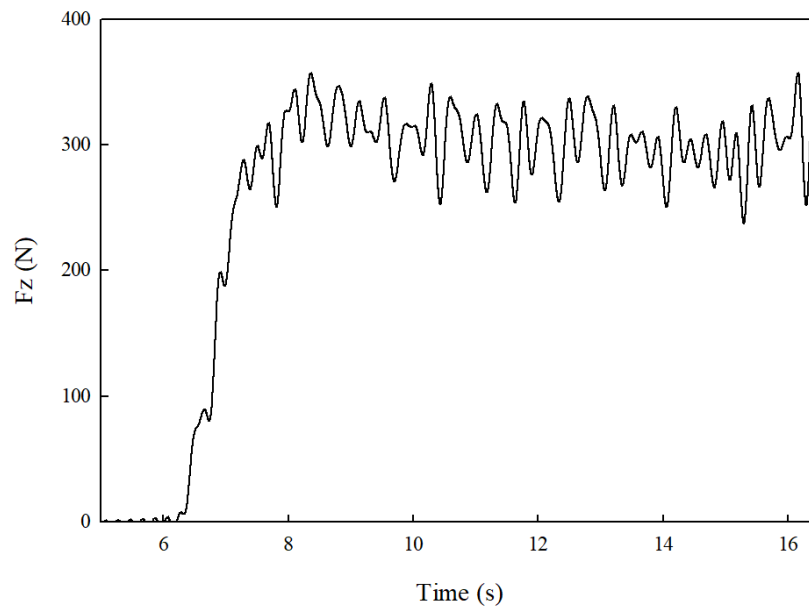
Figure 7-3. Cutting force in Z-direction, at  $V = 240 \frac{\text{m}}{\text{min}}$ ,  $f = 0.3 \frac{\text{mm}}{\text{rev}}$ , and  $i = 5^\circ$

Figure 7-4 shows a one-second period of the cutting force signal in the y-direction. It can be seen that the force signal is oscillating at a constant frequency. This frequency is noticed to be equal to the tool rotational motion frequency, which has also been observed in previous research [86]. That's explained the reason for the signal oscillation, which occurs due to any slight misalignment of the insert.

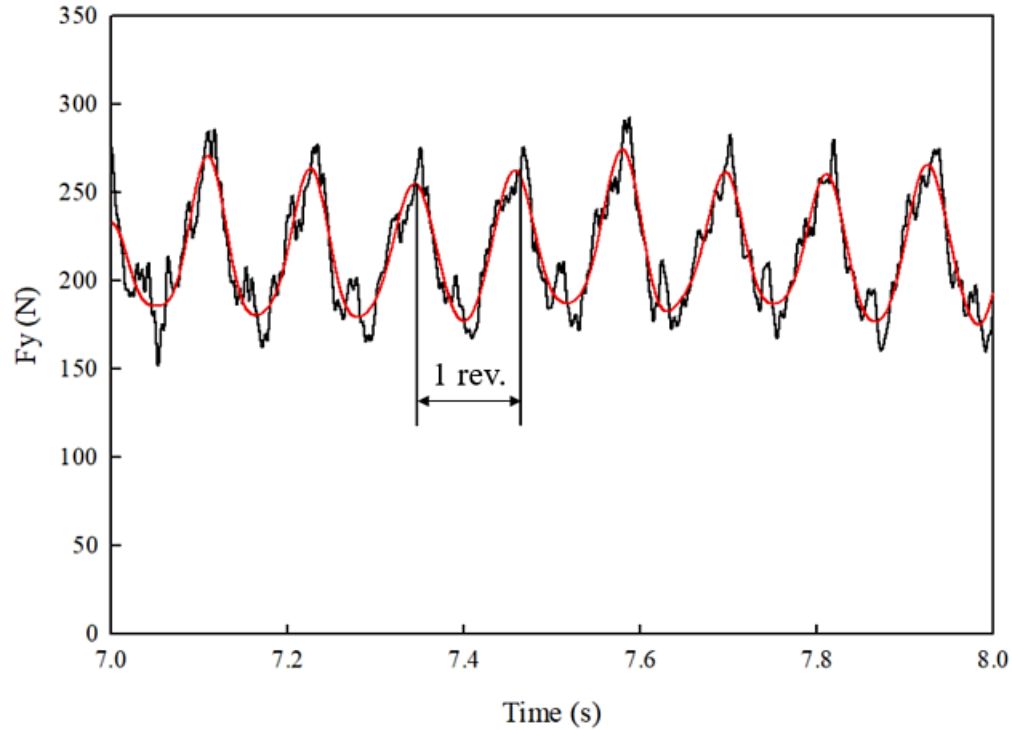


Figure 7-4. Cutting force in y-direction,  $V = 127 \frac{m}{min}$ ,  $f = 0.25 \frac{mm}{rev}$ , and  $i = 15^\circ$

Table 7-5 presents the ANOVA results for the resultant force. It can be seen that the feed rate is the most significant process variable that affects the resultant cutting force with a contribution percentage of 46.88%, followed by the tool inclination angle with a contribution percentage of 13.11%, while the cutting velocity has the lowest effect with almost 5% contribution percentage. Figure 7-5 shows the effect of the design variables levels on the resultant cutting force. Increasing the feed rate leads to higher values of the resultant force. That's expected since the chip load increases with increasing the feed rate. In traditional cutting processes, increasing the cutting velocity

reduces the forces as higher temperature values are generated, and accordingly, the thermal softening of the workpiece is increased. However, the same behavior does not occur in the self-propelled rotary tools, as can be seen in Figure 7-5. It is observed that increasing the cutting velocity leads to an increase in the resultant force up to cutting velocity of 167 m/min, and then the resultant force decreases at cutting velocity of 240 m/min. In terms of the inclination angle, the cutting forces decrease with increasing the inclination angle up to level 3 (i.e., 15°); however, the resultant force increases at an inclination angle of 20°. Both observations for cutting velocity and inclination angles effects can be attributed to the fact that increase in the cutting velocity and the inclination angle will lead to a noticeable increase in the tool rotational speed, which represents a contradicted effect on the temperature, and this effect will be fully explained in the discussion of the cutting temperature results. In addition, these observations are in agreement with a previous study [59]. The optimum process variables levels for the resultant force are inclination angle of 15°, feed rate of 0.1 mm/rev, and cutting speed of 70 m/min.

Table 7-4. ANOVA response table for resultant cutting force (N) means

Level	A	B	C
1	262.5	175.8	221.2
2	235.7	231.3	232.5
3	204.6	259.8	256.8
4	257.4	293.4	249.7
Delta	57.8	117.5	35.6
Rank	2	1	3
Contribution %	13.1%	46.9%	4.9%

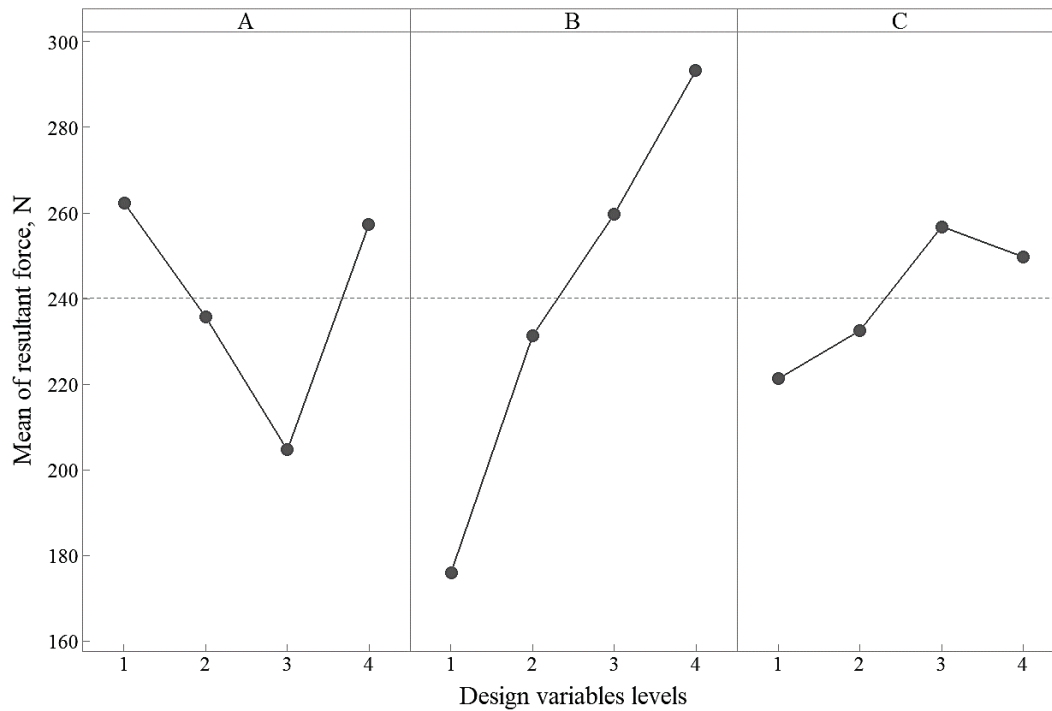


Figure 7-5. Design variables effect on the resultant cutting force

Figure 7-6 shows a comparison between the rotating and fixed cutting tools at the worst and best scenarios (i.e., maximum and minimum values) of the resultant cutting force. It is found that the resultant cutting force is reduced by around 18% at test 4, which has the maximum resultant force. Besides, the resultant force is also reduced by around 11% in test 9, where the lowest resultant force is found. This confirms that less energy and power are required when machining using self-propelled rotary tools. That can be attributed to the significant improvement in the rotary tool life compared to the fixed tool.

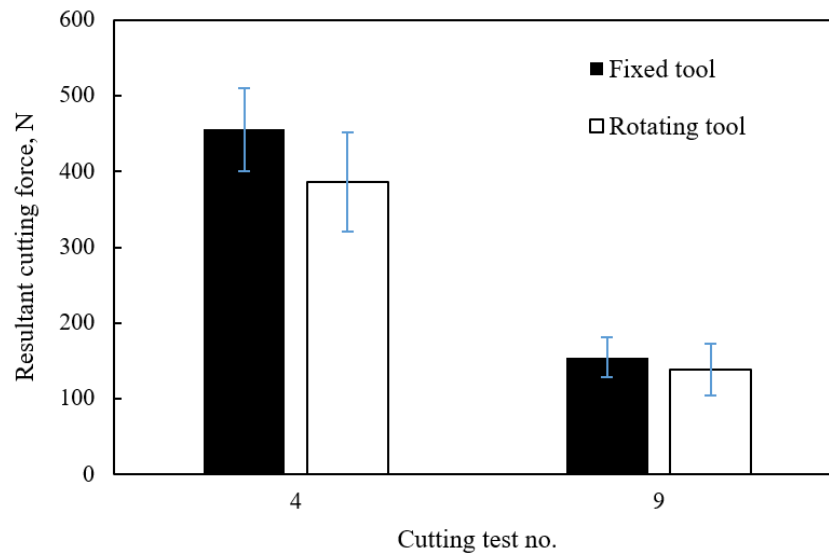


Figure 7-6. Resultant cutting force results for rotatory tool versus fixed tool at worst and best conditions

## 7.4 Flank tool wear results

Figure 7-7 shows the results of the average flank tool wear during dry machining with self-propelled rotary tools. The flank wear is measured after cutting length of 100 mm for each run. The results show that the minimum flank wear occurs at the lowest cutting speed tests (i.e., tests 6, 11, and 16). This is expected because the reduction in the cutting speed reduces the amount of work consumed in the deformation zone and reduces the friction between the tool and the workpiece, which accordingly reduces the tool wear. The highest flank wear is noticed at test 14, in which the tool inclination angle of  $20^\circ$ , the feed rate of 0.15 mm/rev, and cutting velocity of 167 m/min were used. That is due to the increase of the tool rotational velocity with increasing of both the inclination angle and the cutting velocity; thus, the cutting conditions of test 14 would lead to a noticeable increase in the cutting temperature, which adversely affects the tool wear. The same behavior can be noticed in test 5.

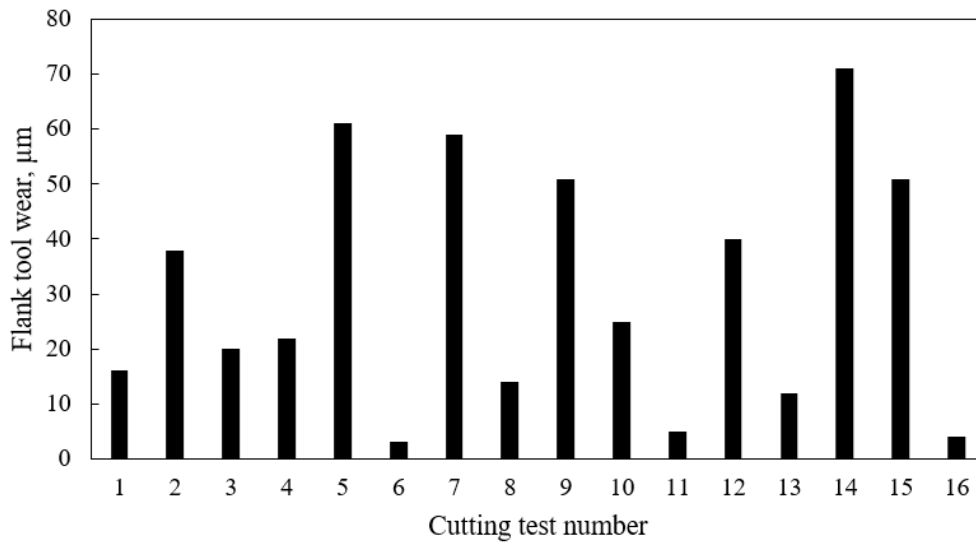


Figure 7-7. Flank tool wear results

Table 7-5 presents the ANOVA results for the flank tool wear. It can be seen that the cutting velocity is the most significant design variable that affects the flank tool wear with contribution percentage of almost 50%, and it is followed by the feed rate with contribution percentage of 8%, while the inclination angle has the lowest effect with almost 4% contribution percentage, which is also expected as the cutting velocity is the most dominant factor affecting the tool life. Figure 7-8 shows the effect of the design variables levels on the flank tool wear. Increasing the feed rate seems to slightly reduce the tool wear up to 0.2 mm/rev, and then a noticeable decrease is observed at a feed rate of 0.25 mm/rev. That is because the process becomes more stable at large feed rates, since the chips tend to be more continuous, as confirmed in a previous study [148]. The optimum process variables levels for the flank tool wear are inclination angle of 5°, feed rate of 0.25 mm/rev, and cutting speed of 70 m/min.

Table 7-5. ANOVA response table for flank tool wear ( $\mu\text{m}$ ) means

Level	A	B	C
1	24	35	6.5
2	34.25	34.25	47.5
3	30.25	33.75	39
4	34	19.5	29.5
Delta	10.25	15.5	41
Rank	3	2	1
Contribution %	3.84%	8.24%	48.66%

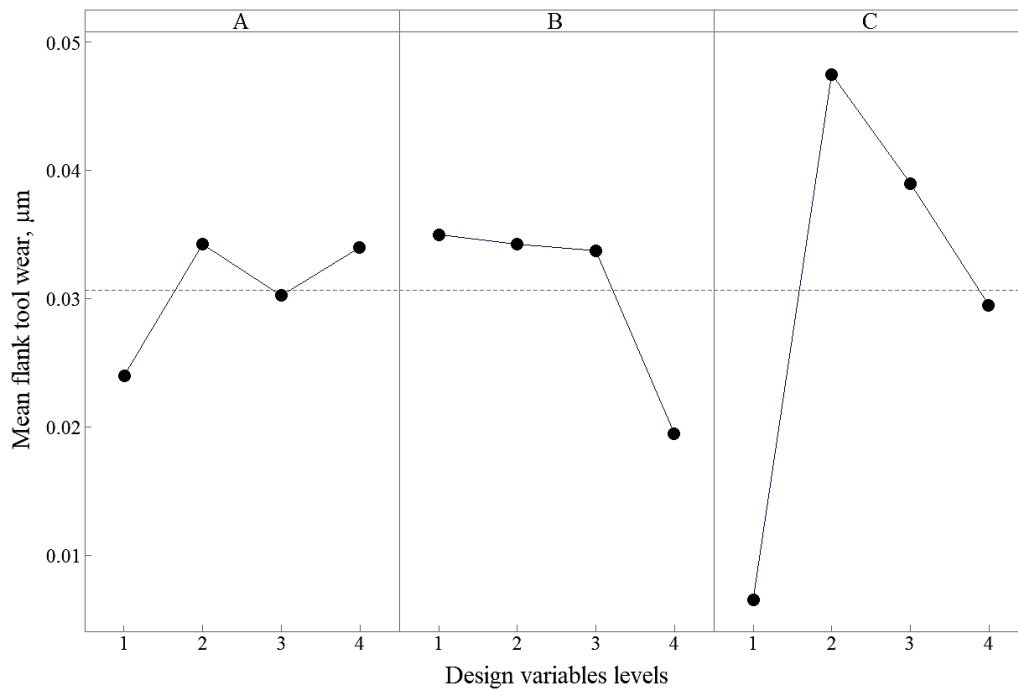


Figure 7-8. Design variables effect on the flank tool wear

Figure 7-9 shows a comparison between the rotating and fixed cutting tools at the worst and best scenarios of the average flank tool wear; the log scale is used for the flank tool wear (i.e., y-axis). It is found that the flank tool wear is reduced by around 37% at test 14, which has the maximum flank tool wear (i.e., 71  $\mu\text{m}$ ). Besides, the flank tool wear is also reduced by around 22% in test 6, where the lowest flank tool wear is observed. This is attributed to the distribution of the tool wear over the whole round cutting edge,

in case of rotary tool, instead of being concentrated at a fixed point, as occurred in the fixed tool case. It is worth mentioning that the tool life of the SPRT is dramatically high compared to fixed tools as confirmed by Chen et al. [59].

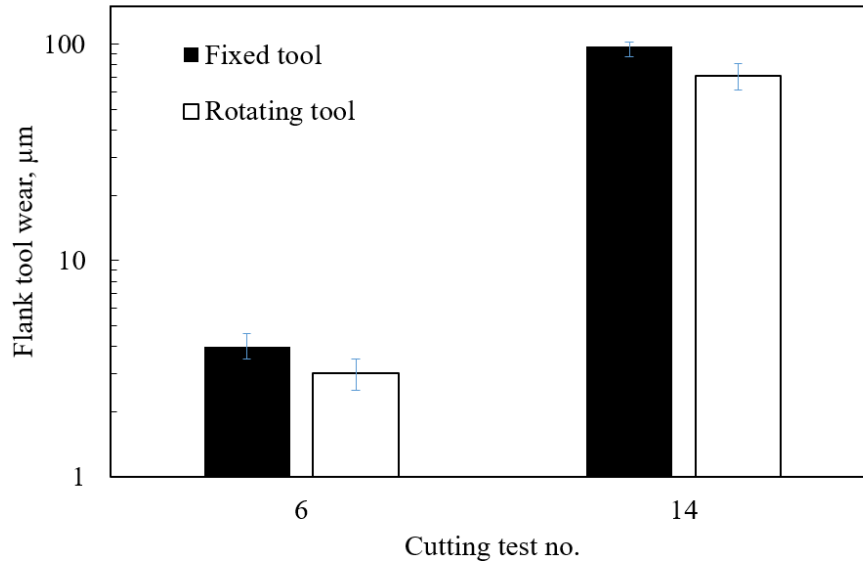


Figure 7-9. Average flank tool wear results for rotary tool versus fixed tool at worst and best conditions

To study the effect of the inclination angle on the tool wear and the surface quality, a comparison was performed between two cutting tests under certain conditions of cutting speed and feed rate (i.e.,  $v=167$  m/min and  $f=0.15$  mm/rev) with two different inclination angles of  $5^\circ$  and  $20^\circ$ , as shown in Figure 7-10. It was observed that when using a low inclination angle (i.e.,  $5^\circ$ ), the chips were collided and pushed into the workpiece surface, as shown in Figure 7-10b. Afterwards, the cutting edge crushes the adhered chips, which increases the tool wear, as can be seen in Figure 7-10d. On the other hand, no chip adhesion was observed in the machined surface at  $20^\circ$  inclination angle (see Figure 7-10a), and accordingly, lower tool wear was obtained compared to the case of  $5^\circ$  inclination angle (see Figure 7-10c). That can be attributed to the increase in the chip flow angle based on the oblique cutting principles, as confirmed by Yamamoto et al. [149].

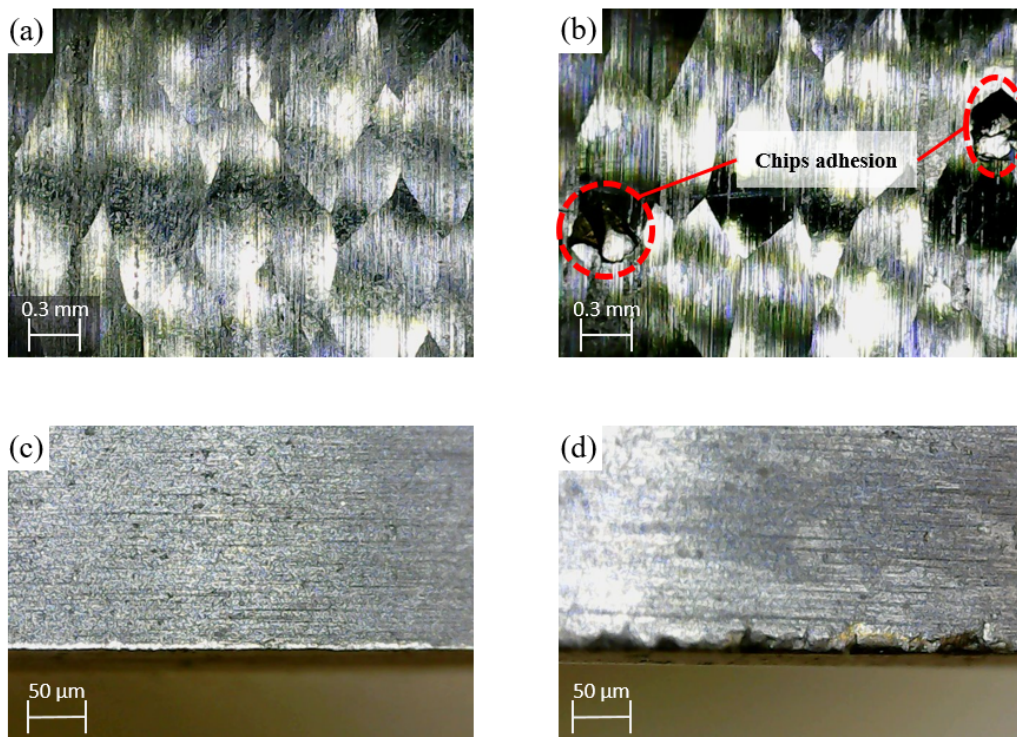


Figure 7-10. A Comparison between the finished surface and corresponding tool damage based on the tool inclination angle; (a, and c) at 20° and (b, and d) at 5°

## 7.5 Average surface roughness results

Figure 7-11 shows the results of the average surface roughness. The cut-off length of 2.5 mm is used for all the runs. The results illustrate that the variation of the cutting conditions has a clear effect on the surface roughness values. The lowest surface roughness is observed at test 13 in which 20° inclination angle, 0.1 mm/rev feed rate, and 240 m/min cutting velocity were used.

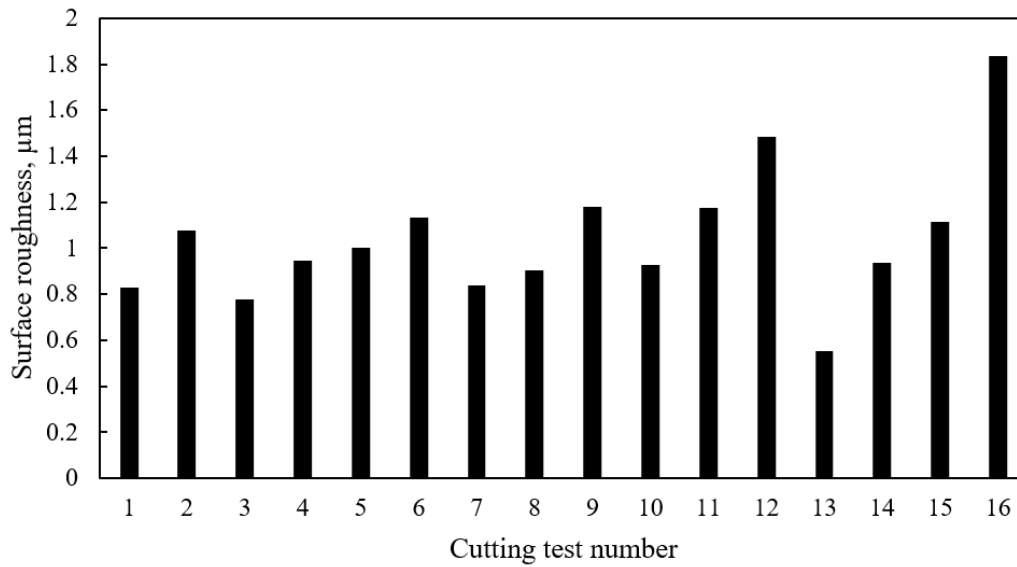


Figure 7-11. Average surface roughness results

Table 7-6 presents the ANOVA results for the average surface roughness. It can be seen that the cutting velocity was the most significant process variable affects the surface roughness with a contribution percentage of almost 35%, followed by the feed rate with a contribution percentage of 27%, while the inclination angle has the lowest effect with a 15% contribution. Figure 7-12 shows the effect of the design variables levels on the average surface roughness. Increasing the cutting speeds improved surface quality, as expected. Besides, increasing the feed rates reduced the surface quality and leads to higher surface roughness values. The surface roughness values increased with increasing the inclination angle up to level 3 (i.e.,  $15^\circ$ ). That is because the inclination angle directly affects the tool rotational speed, and increasing the tool rotational speed increases the dynamic of the cutting process, which affects the surface quality. However, a further increase in the inclination (i.e.,  $20^\circ$ ) improved the surface roughness due to the large change of the chip flow angle, which prevents any adhesions or scratches of the machined surface, as confirmed by Yamamoto et al. [149]. The optimum process variables levels for the surface roughness were  $5^\circ$  inclination angle, 0.1 mm/rev feed rate, and 240 m/min cutting velocity.

Table 7-6. ANOVA response table for surface roughness ( $\mu\text{m}$ ) means

Level	A	B	C
1	0.90	0.89	1.24
2	0.97	1.02	1.17
3	1.19	0.98	0.95
4	1.11	1.29	0.82
Delta	0.28	0.40	0.43
Rank	3	2	1
Contribution %	15.19%	27.25%	34.98%

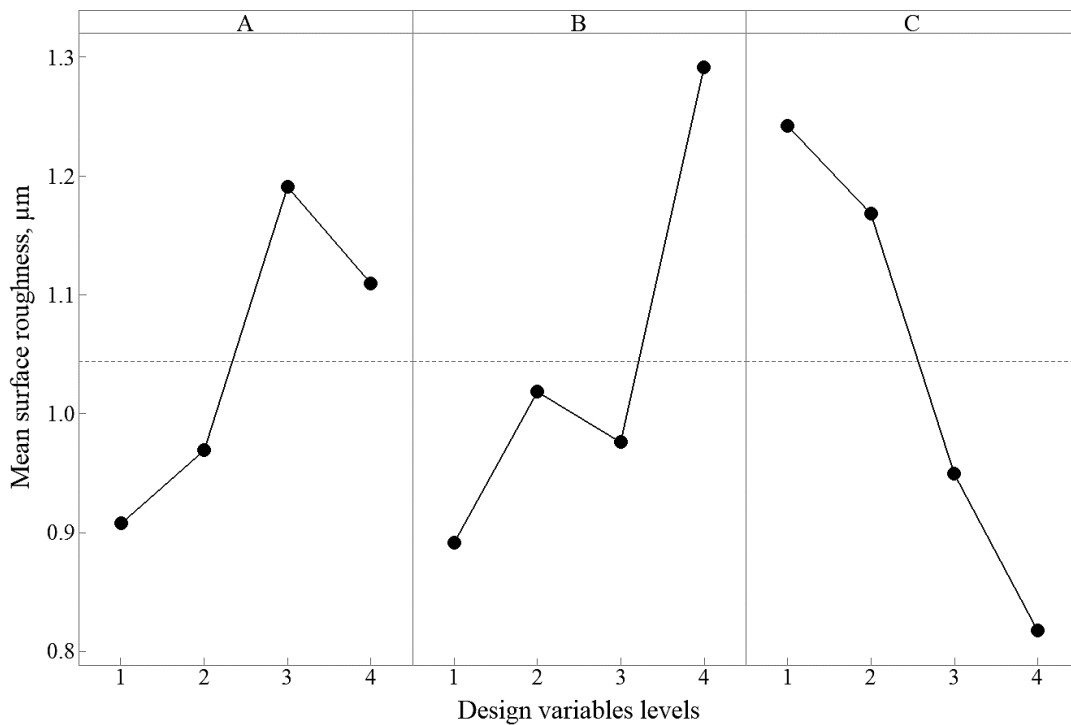


Figure 7-12. Design variables levels effect on the surface roughness

Figure 7-13 shows a comparison between the rotary and fixed cutting tools at the worst and best cutting conditions for the surface roughness results. Generally, the values of the surface roughness for the round insert in both SPRT and fixed tools are

relatively low compared to the conventional tools due to the large radius of the round insert compared to the nose radius. It is observed that the fixed tool provides better surface roughness compared to the SPRT, especially at test 16, which has the worst surface roughness. That can be attributed to several possible factors such as the machining stability, which is largely affected by the moving nature of the SPRT, and also the generated marks in the direction of the relative cutting velocity in SPRT, as indicated by Kishawy et al. [147].

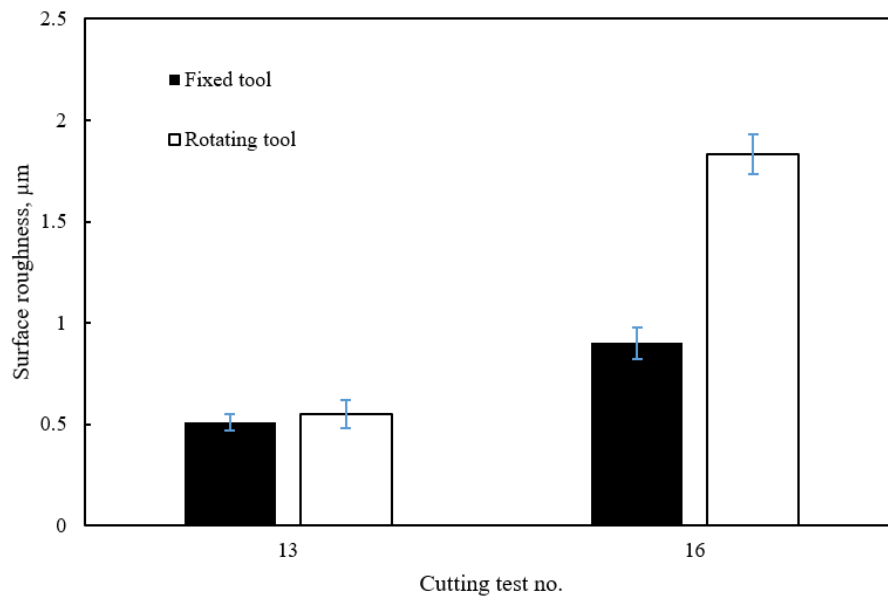


Figure 7-13. Surface roughness results for rotary tool versus fixed tool at worst and best conditions

## 7.6 Temperature results and influence of the tool speed on the thermal behavior

Table 7-7 presents the ANOVA results for the tool rotational speed. It can be seen that the cutting inclination angle is the most significant process variable that affects the tool rotational speed with contribution percentage of 55%, and it is followed by the cutting velocity with contribution percentage of 35%, while the feed rate has the lowest effect

with only 3% contribution percentage. Figure 7-14 shows the effect of the design variables levels on the tool rotational speed. It is clearly noticed that increasing the cutting speeds and the inclination angle lead to a significant increase in the tool rotational speed. This is expected as the tool rotational speed can be analytically estimated by equation 7-1 [63]:

$$V_r = C V_W \sin i \quad 7-1$$

where  $V_r$  is the tool rotational speed,  $V_W$  is the cutting velocity,  $i$  is the inclination angle, and  $C$  is a process constant.

It can be observed that increasing the feed rate reduces the tool rotational speed. That can be explained by the fact that the chip load increases with increasing the feed rate, which accordingly leads to an increase in the friction losses.

Table 7-7. ANOVA response table for the tool rotational speed (RPM) means

Level	A	B	C
1	155.3	452.5	177.9
2	309.1	419.9	322.5
3	460.7	347.2	424.1
4	608.9	314.6	609.5
Delta	453.5	137.9	431.5
Rank	1	3	2
Contribution %	54.8%	7.1%	35.3%

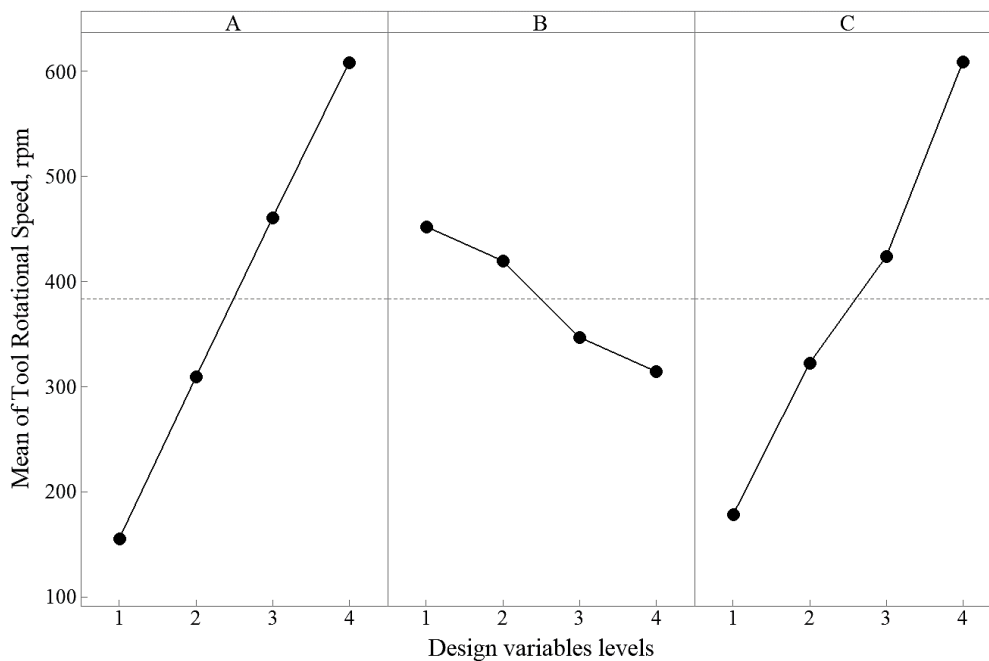


Figure 7-14. Design variables levels effect on the tool rotational speed

Figure 7-15 shows the cutting tool temperature results for the machining process using self-propelled rotary tools. The results illustrate that the variation of the cutting conditions has a direct corresponding effect on the tool temperature values. The highest temperature of 582 °C is observed at test 1, while the lowest temperature of 178 °C is observed at test 16. Table 7-8 presents the ANOVA results for the tool temperature. It is found that the cutting inclination angle is the most significant variable that affects the tool temperature with contribution percentage of 65%, and it is followed by the cutting velocity with contribution percentage of almost 10%, while the feed rate has the lowest effect with only 2.35 % contribution percentage. Figure 7-16 shows the effect of the design variables levels on the tool temperature. Increasing the inclination angle, which directly affects the tool rotational speed, reduces the tool temperature up to a certain level (i.e., level 3), then a slight increase in the cutting temperature is observed at level 4. A confounding behavior is observed when changing the cutting velocity as increasing the cutting velocity increases the generated heat flux; however, increasing the cutting velocity will also increase the

tool rotational speed. The effect of the tool rotational speed on the cutting temperature can be explained as follows:

- Increasing the tool rotational speed reduces the engaging time with the workpiece for each portion of the cutting edge, which accordingly reduces this portion temperature (i.e., maximum tool temperature);
- However, increasing the tool speed also reduces the cooling time for each portion of the cutting edge before engaging again with the workpiece, which would increase the average tool temperature;
- Thus, the tool rotational speed represents a contradicted effect on the cutting temperature, and increasing either the cutting velocity or the inclination angle isn't necessarily leading to an increase in the cutting temperature.

The optimum process variables levels for the cutting temperature are 15° inclination angle, 0.25 mm/rev feed rate, and 240 m/min cutting velocity.

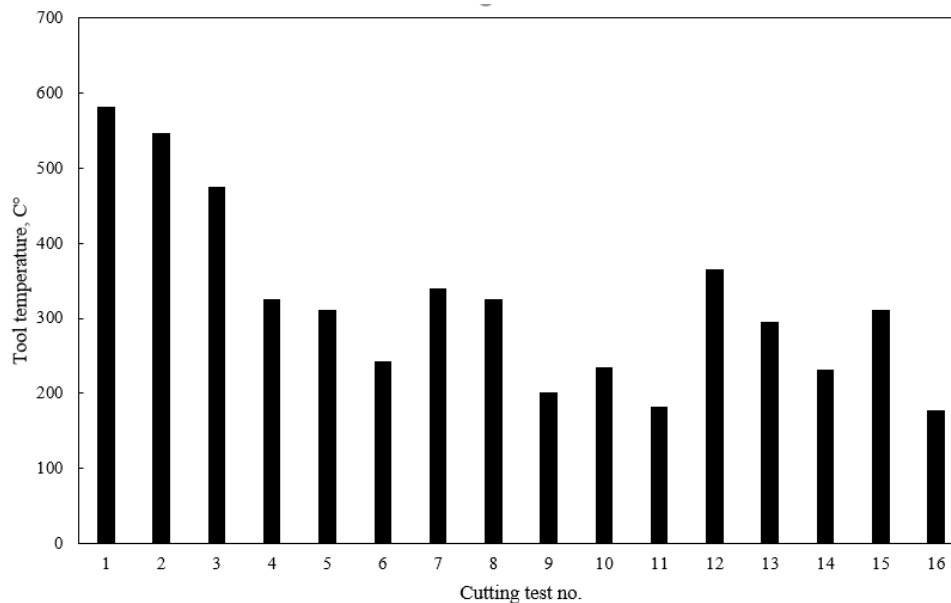


Figure 7-15. Cutting temperature results

Table 7-8. ANOVA response table for the tool temperature ( $^{\circ}\text{C}$ ) means

Level	A	B	C
1	482.8	347.6	296.6
2	305.1	314.2	384.0
3	245.7	327.5	308.5
4	254.3	298.4	298.8
Delta	237.1	49.2	87.4
Rank	1	3	2
Contribution %	65.7%	2.3%	9.3%

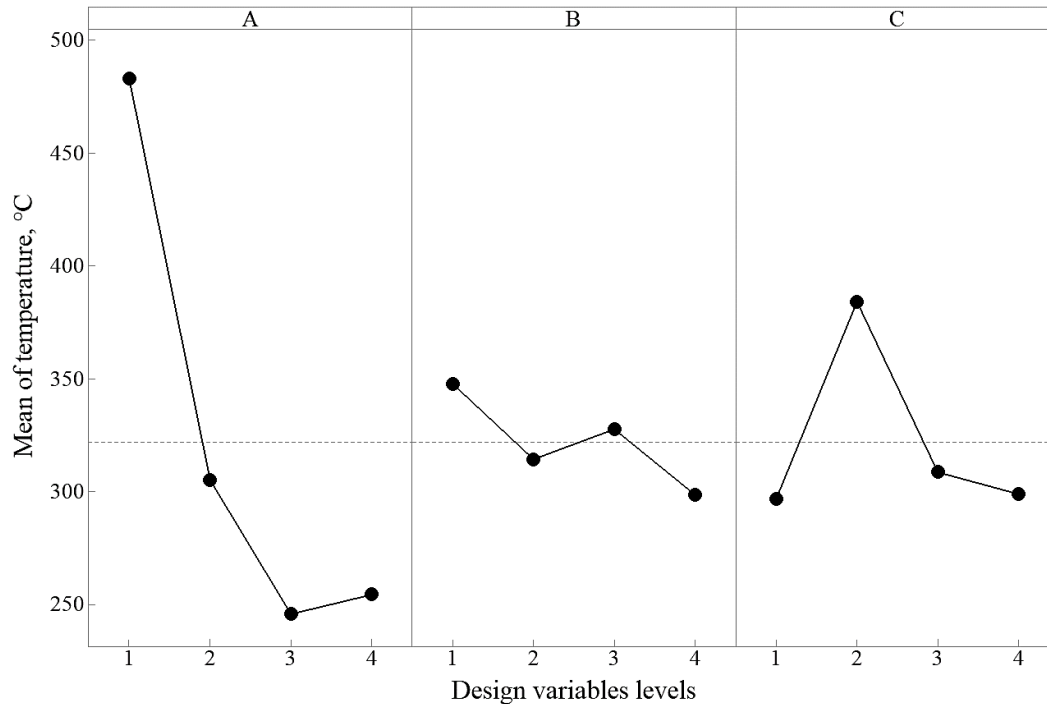


Figure 7-16. Design variables levels effect on the cutting temperature

Figure 7-17 shows a comparison between the rotating and fixed cutting tools at the worst and best scenarios of the tool temperature. It is observed that the cutting tool temperature is reduced by around 13% at test 1, which has the maximum tool temperature. Besides, the tool temperature is also reduced by around 37% at test 16,

where the lowest temperature is captured. Consequently, the tool's rotary motion improved the tool temperature, as proved by Dessoly et al. [135]. The improvement in the cutting temperature when using the rotary tool compared to the fixed wasn't only the main advantage, but also using the rotary tools allows each portion of cutting edge to be affected by this high temperature for a relatively short time (i.e., engaging time), instead of being concentrated at a single point during the whole cutting process as occurred in the fixed tool.

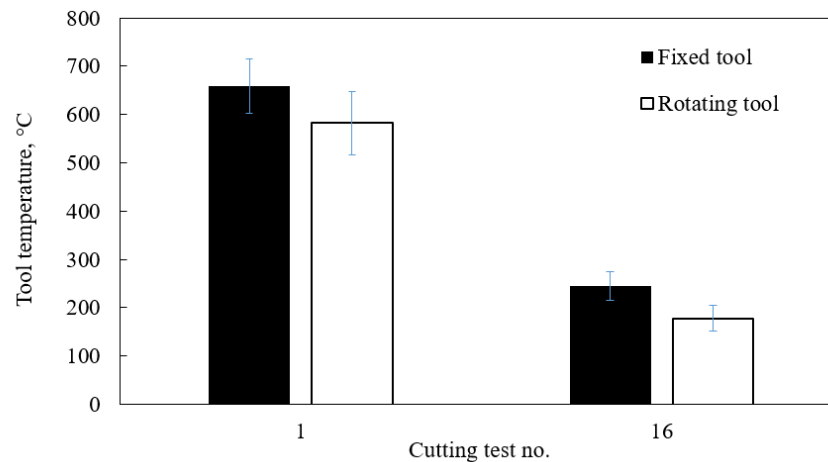


Figure 7-17. Cutting temperature results for rotary tool versus fixed tool at worst and best conditions

## 7.7 Machining performance characteristics modeling and optimization

In this section, the genetic programming (GP) is used to develop models for the surface roughness and tool wear, as shown in equation 7-2 and equation 7-3. Afterward, the non-dominated sorting genetic algorithm (NSGA-II) is utilized to perform multi-objective optimization for the machining performance characteristics.

$$Ra = 0.0066 * i^2 + 42.91 * i * f^4 - 0.07 * i - 2.20e^{-9} * V * i^5 - 10.9 * i * f^3 + 1.12 \quad 7-2$$

$$VB = 387.22 + \frac{8.32}{f} + 16.53 * i * f + 0.03 * f * V^2 - \frac{21799.6 + 16.53 * i^2 * f^2}{V} - 2.31 * V - 50.67 * V * f^3 \quad 7-3$$

Three machining objectives functions were considered in the optimization process; tool wear, surface roughness, and material removal rate. The problem constraints, according to the current experimental plan, are as follows:

$$\begin{cases} 5^\circ \leq i \leq 20^\circ \\ 0.1 \text{ mm/rev} \leq f \leq 0.25 \text{ mm/rev} \\ 70 \text{ m/min} \leq V \leq 240 \text{ m/min} \end{cases}$$

Figure 7-18 and Figure 7-19 show a comparison between the experimental and predicted results for flank tool wear and average surface roughness, respectively. The surface roughness  $R_a$  model showed average model accuracy of 94.33% with 0.89 goodness of fit  $R^2$ . Besides, the average model accuracy of 87.44% was achieved for tool wear model with 0.88 goodness of fit  $R^2$  and 4.02 mean absolute error.

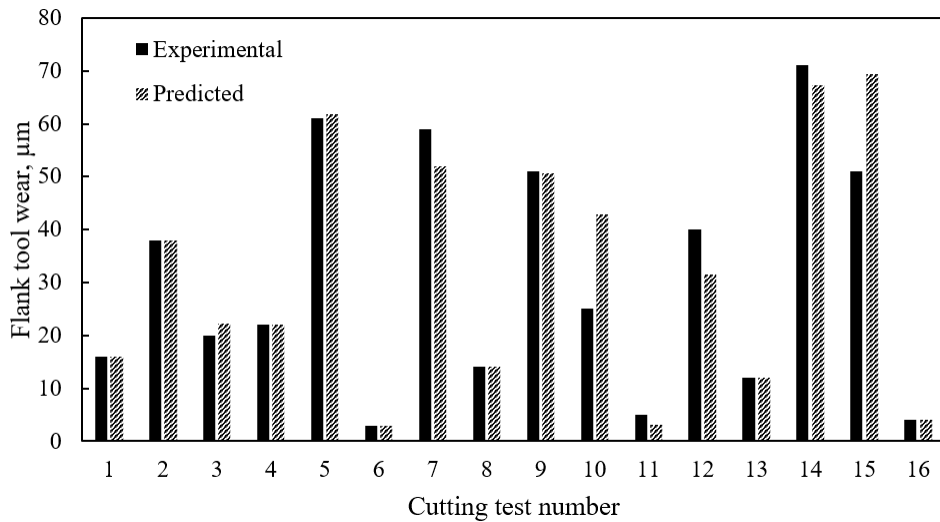


Figure 7-18. A Comparison between experimental and predicted flank tool wear

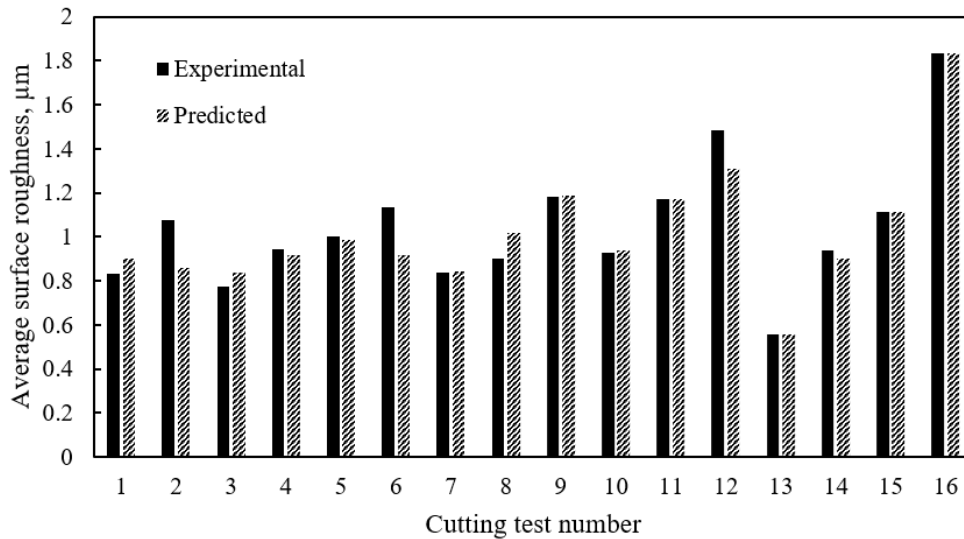


Figure 7-19. A Comparison between experimental and predicted average surface roughness

Regarding the multi-objective optimization, a sensitivity analysis is performed in order to select the best optimization parameters. Population size of 400, mutation factor of 0.01, and cross-over rate of 0.7 were selected, as they provide a convergence solution. The solver was allowed to proceed until the function tolerance of  $10^{-4}$  was achieved.

The binary chromosome was utilized to express the individuals (i.e., solutions), as can be seen in Figure 7-20a. The crossover, selection, and mutation operations are conducted to offer a new offsprings population for the next generation. In terms of the selection, the binary tournament operation was utilized to determine the individuals in the first generation for the mating pool. Then, the crowded-comparison operator has used for the selection operation in the next generations based on the rank and the crowded-distance, as discussed in previous work [145]. Then, the selected solutions in the mating pool are used for the crossover and mutation process. Two-point crossover is randomly adopted to provide offspring pairs through exchanging parts of their parents, as provided in Figure 7-20b. In the single point mutation process, offspring is clarified by changing 1-gen in the original solution to maintain the diversity in the population, as provided in Figure 7-20c. These steps are repeated until reaching the stopping criterion. In the end, the set of non-dominated solutions are considered as the highest-ranked front after achieving the stop criterion.

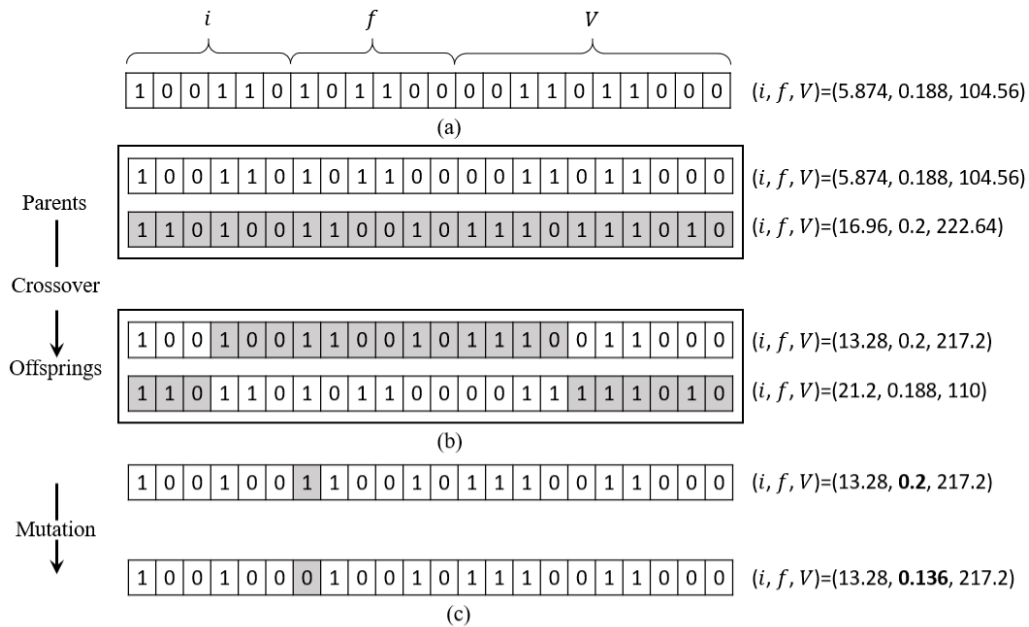


Figure 7-20. (a) Individual's binary representation (genotype), (b) schematic of the crossover process, (c) schematic of the mutation process

Figure 7-21 shows the Pareto-front solutions for the three objectives functions. The Pareto-front solution is distributed into two groups, group 1 and group 2. For the first group, it can be noticed that the dominant relationship between the tool wear and the material removal rate is an interdependent based-relation. That could be attributed to the high cutting velocity, which associates the high material removal rate. Besides, there is a reduction in the surface roughness values when decreasing the inclination angle and the cutting speed. That is because the surface roughness when machining with self-propelled rotary tools mainly depends on the machining stability due to the dynamic nature of the process. The tool rotational speed is directly affected by the cutting velocity and the inclination angle, as seen in equation 7-1. Therefore, the low inclination angle and cutting velocity lead to slower rotational speed of the cutting insert, which increases the machining stability and produces better surface quality. For the second group, the dominant relationship is the interdependent relationship between the surface roughness and the material removal rate. The higher values of the surface roughness at the high material removal rate are due to the large value of the cutting velocity, which increases the rotational speed of the insert (see equation 8-1) and accordingly reduces the machining stability.

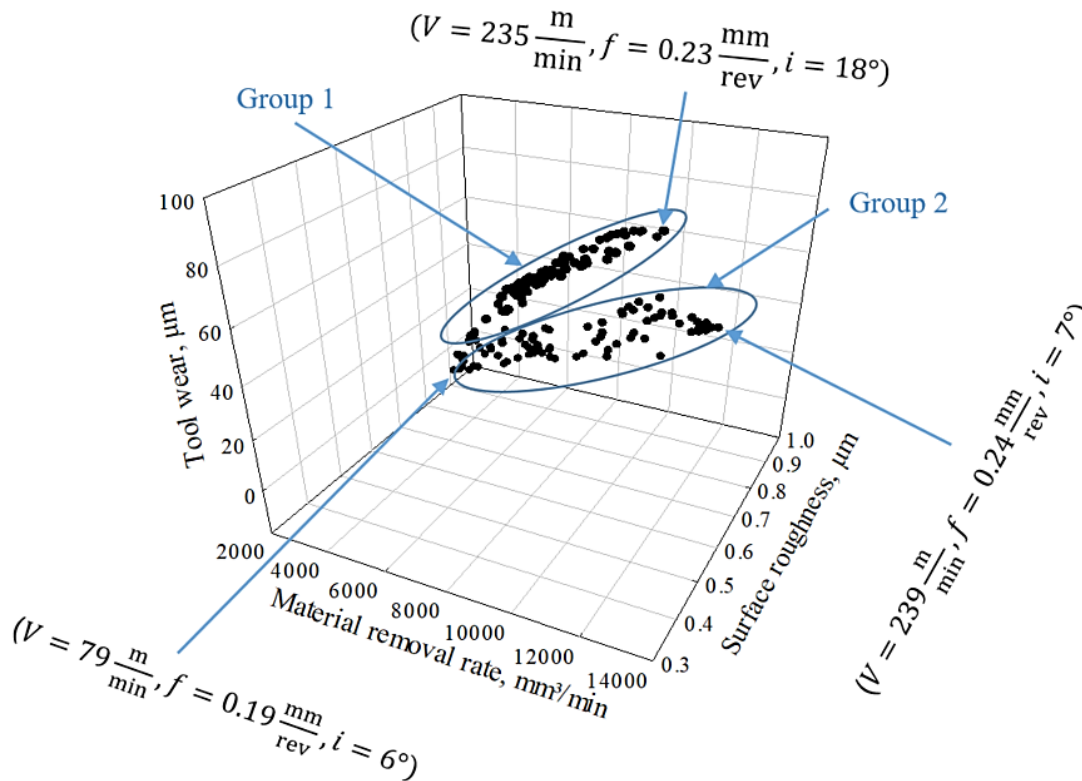


Figure 7-21. Pareto-front solutions

## 7.8 Optimized scenarios

This section provides a new approach to optimize Pareto-front solutions based on different machining scenarios. Three different machining scenarios were investigated; equal-weighted, productivity, and finishing. Different weighting factors were assigned to each scenario to evaluate the output responses. Table 7-9 presents the scenarios used and the weighting factors for each scenario. The multi-objective optimization NSGA-II provides a number of Pareto-front solutions, and to choose the best optimal solution for a certain scenario (e.g., finishing or productivity), normalized Pareto-front solutions based on each scenario were obtained. Afterward, the highest normalized solution in each scenario was considered. The highest optimized solution means that the selected

solution achieves the best balance between all the output responses within each studied scenario.

Table 7-9. Weighting factors for the machining scenarios

Scenario	Machining Outputs		
	Ra	VB	MRR
(A): Equal-weighted	33.34%	33.33%	33.33%
(B): Productivity	10%	30%	60%
(C): Finishing	70%	20%	10%

Table 7-10 shows the result of the normalized optimal solutions for the three studied scenarios. The optimal cutting conditions for the productivity scenario were obtained at the highest cutting velocity and feed rate (i.e.,  $V=240$  m/min and  $f=0.25$  mm/rev), as expected, and at an inclination angle of  $7^\circ$ . While the optimum conditions for the finishing scenario were found at a cutting velocity of 235 m/min, a feed rate of 0.19 mm/rev, and an inclination angle of  $19^\circ$ . Moreover, the optimal conditions for the equal-weighted scenario) were found at a cutting velocity of 98 m/min, a feed rate of 0.23 mm/rev, and an inclination angle of  $7^\circ$ .

To validate the effectiveness of the three studied scenarios, confirmation experimental tests have been conducted, and the results showed good agreement with the predicted values, as can be seen in Figure 7-22. For the flank wear results, the maximum deviation was about  $8 \mu\text{m}$  at the finishing scenario. Regarding the surface roughness results, the maximum deviation was about  $0.17 \mu\text{m}$  for the equal-weighted case.

Table 7-10. A summary of the optimal solutions for the studied scenarios

Scenario	Machining Outputs		
	Ra ( $\mu\text{m}$ )	VB ( $\mu\text{m}$ )	MRR ( $\text{mm}^3/\text{min}$ )
(A): Equal-weighted	0.87	2.42	4580
(B): Productivity	0.92	32.56	11851
(C): Finishing	0.38	79.93	9156

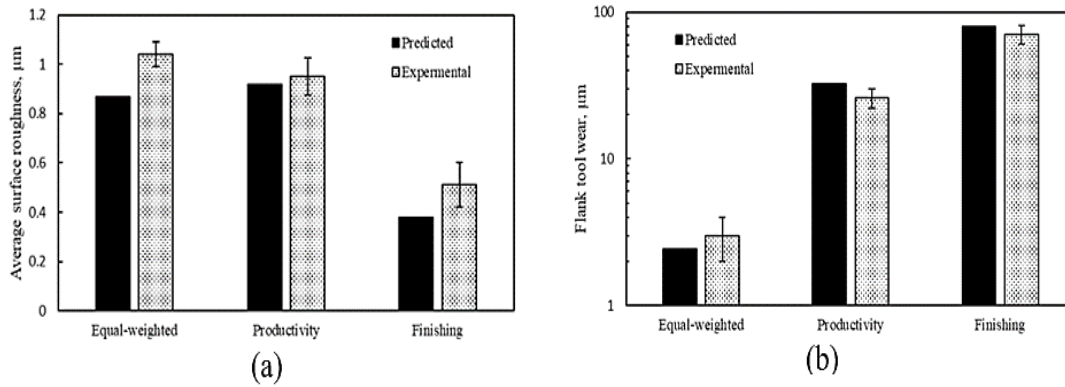


Figure 7-22. Experimental validation of the optimized scenarios results; (a) Average surface roughness and (b) Flank tool wear

## Chapter 8: Conclusions

The most important findings of this research are summarized as follows:

- An analytical-based model was proposed to predict the cutting forces and tool rotational speeds during the machining process with self-propelled rotary tools. The insert bearing friction is considered in order to provide accurate and more realistic results. The model shows very good agreement with the experimentally observed results in terms of cutting forces and tool rotational speed. The average model accuracy was 95.54% for the cutting forces, while the average accuracy of 93.63% is achieved for the tool's rotational speed;
- Finite Element Modeling (FEM) based on a material plastic model, damage model, and friction law is utilized to simulate the cutting process using SRPT. The simulation results in terms of cutting forces, temperature, heat flux, and the contact area between the chip and the tool are obtained. Good agreement is observed between the numerical and experimental results in terms of cutting forces and chip morphology. The average model accuracy was 96.39% for the cutting forces, while the average accuracy of 90.83% is achieved for the chip's flow angle;
- In order to achieve the steady-state temperature field, the energy equation with a moving heat source is numerically solved for the tool domain. COMSOL software is utilized for this purpose;
- According to the numerical results, a reduction of 65 °C as an average cutting temperature was noticed between the fixed and rotating tools, which significantly demonstrates the effectiveness of using SRPT;
- In the rotary tool case, the maximum temperature is observed in the core of the chip and does not extend to the secondary shear zone. It is worth to mention that this is a new and an important observation, which occurs due to that the generated heat in the secondary shear zone is continuously removed by the tool rotational motion;

- As the tool rotational speed increases, the peak temperature as well as the tool bulk temperature decrease. However, the temperature increases again at a relatively high tool rotational speed. That is because increasing the tool rotational speed beyond a certain value may reduce the cooling time for each portion of the cutting edge. Consequently, that could lead to a noticeable increase in the tool temperature again;
- During machining using the SPRT, it is found that the thrust force is the largest force component, and it oscillates around the average value with a frequency equal to the rotational motion frequency;
- The feed rate is the most significant process variable that affects the resultant cutting force with a contribution percentage of 46.88%; followed by the tool inclination angle with a contribution percentage of 13.11%, while the cutting velocity has the lowest effect with almost 5% contribution percentage;
- Using self-propelled rotary tools reduces the resultant force by 18% and 11% at the worst and best cutting conditions, respectively, compared to the fixed tool;
- The average flank tool wear after cutting 100 mm was measured for each run, and the cutting velocity is the most significant design variable that affects the flank tool wear with a contribution percentage of almost 50%, and it is followed by the feed rate with contribution percentage of 8%, while the inclination angle has the lowest effect with almost 4% contribution percentage;
- When machining with self-propelled rotary tools, the flank tool wear was reduced by 22% and 37% at the best and worst cutting conditions, respectively, compared to the fixed tool;
- The average surface roughness with a cut-off length of 2.5 mm was measured for the machined surface after each run, and it is observed that the cutting velocity is the most significant process variable affects the surface roughness with a contribution percentage of almost 35%, followed by the feed rate with contribution percentage of 27%, while the inclination angle has the lowest effect with 15% contribution;

- The comparison between the self-propelled rotary tool and the fixed tool shows that the fixed tool provides better surface roughness;
- The cutting inclination angle is found to be the most significant process variable that affects the tool rotational speed with a contribution percentage of 55%, and it is followed by the cutting velocity with a contribution percentage of 35%, while the feed rate has the lowest effect with only 3% contribution percentage;
- It is found that the inclination angle is the most significant variable that affects the tool temperature with a contribution percentage of 65%, and it is followed by the cutting velocity with a contribution percentage of almost 10%, while the feed rate has the lowest effect with only 2.35 % contribution percentage;
- A comparison between the rotary and fixed cutting tools was performed at the worst and best cutting conditions of the tool temperature. It is observed that the cutting tool temperature is reduced by around 13% at test 1, which has the maximum tool temperature. Besides, the tool temperature is also reduced by around 37% at test 16, where the lowest temperature is captured;
- The improvement in the cutting temperature when using the self-propelled rotary tool compared to the fixed wasn't only the main advantage, but also using the rotary tools allows each portion of the cutting edge to be affected by this high temperature for a relatively short time (i.e., engaging time), instead of being concentrated at a single point during the whole cutting process as occurred in the fixed tool;
- A detailed mechanism for machining process with self-propelled rotary tools is fully presented and discussed;
- A comparison between two cutting tests with different inclination angles shows that there is no chip adhesion observed in the machined surface at 20° inclination angle, and accordingly, lower tool wear was obtained compared to the case of 5° inclination angle;
- Based on the optimized scenarios of multi-objective optimization (NSGA-II), the optimal cutting variable levels for the equal-weighted scenario were found at a cutting velocity of 98 m/min, a feed rate of 0.23 mm/rev, and an inclination

angle of  $7^\circ$ . In addition, the optimal cutting conditions for the productivity scenario were obtained at the highest cutting velocity and feed rate (i.e.,  $V=240$  m/min and  $f=0.25$  mm/rev), and at an inclination angle of  $7^\circ$ . While the optimum conditions for the finishing scenario were found at a cutting velocity of 235 m/min, a feed rate of 0.19 mm/rev, and an inclination angle of  $19^\circ$ ;

- To validate the effectiveness of the three studied scenarios, confirmation experimental tests have been conducted, and the results showed a good agreement with the predicted values.

# Chapter 9: Thesis contributions and future work

## 9.1 Contributions

The main contributions offered in this thesis are summarized as follows:

- A novel analytical based model was developed to predict the cutting forces and tool rotational speeds during the machining process with self-propelled rotary tools, which offered higher overall accuracy compared to all existing models in the open literature;
- A hybrid numerical model was proposed to predict the temperature distribution during cutting with SPRT. The proposed model addresses the limitation of other previous models as it is purely focused on significant aspects such as; generated heat flux, and the contact area between the tool and the chip;
- The experimental investigation offered deep-understanding of the mechanisms related to machining processes with SPRT.

## 9.2 Future work

The following suggestions are presented in terms of future work:

- Improving the design of SPRT to enhance the dynamic nature of the process in order to provide better surface roughness;
- Investigating the surface integrity (e.g., microstructure and residual stresses analysis);
- Extending the current presented models for the milling processes using self-propelled rotary tools;

## Chapter 9: Thesis contributions and future work

- Establishing a solid sustainability assessment of the machining process with SPRT including; environmental impact, energy consumption, waste management, total processing cost, and personal health and safety.

## References

1. Klocke, F., Manufacturing processes 1: cutting. 2011: Springer Science & Business Media.
2. Kishawy, H., An experimental evaluation of cutting temperatures during high speed machining of hardened D2 tool steel. 2002.
3. Lütjering, G. and J.C. Williams, Titanium. 2007: Springer Science & Business Media.
4. Kishawy, H.A. and A. Hosseini, Machining Difficult-to-cut Materials: Basic Principles and Challenges. 2018: Springer.
5. Abukhshim, N., P. Mativenga, and M.A. Sheikh, Heat generation and temperature prediction in metal cutting: A review and implications for high speed machining. *International Journal of Machine Tools and Manufacture*, 2006. 46(7-8): p. 782-800.
6. Shokrani, A., V. Dhokia, and S.T. Newman, Environmentally conscious machining of difficult-to-machine materials with regard to cutting fluids. *International Journal of machine Tools and manufacture*, 2012. 57: p. 83-101.
7. Sun, S., M. Brandt, and M. Dargusch, Machining Ti-6Al-4V alloy with cryogenic compressed air cooling. *International Journal of Machine Tools and Manufacture*, 2010. 50(11): p. 933-942.
8. Marksberry, P., Micro-flood (MF) technology for sustainable manufacturing operations that are coolant less and occupationally friendly. *Journal of Cleaner Production*, 2007. 15(10): p. 958-971.
9. Aggarwal, A., et al., Optimization of multiple quality characteristics for CNC turning under cryogenic cutting environment using desirability function. *Journal of materials processing technology*, 2008. 205(1-3): p. 42-50.
10. Krishna, P.V., et al. Application of nanomaterials as coolants/lubricants in machining. in *International Conference on Advanced Nanomaterials & Emerging Engineering Technologies*. 2013. IEEE.
11. Lu, T., A metrics-based sustainability assessment of cryogenic machining using modeling and optimization of process performance. 2014.
12. Hosokawa, A., et al., Turning of difficult-to-machine materials with actively driven rotary tool. *CIRP annals*, 2010. 59(1): p. 89-92.

13. Shaw, M.C., P.A. Smith, and N.H. Cook, The rotary cutting tool. Trans. ASME, 1952. 74: p. 1065-1076.
14. Sokolov, N.V. and A.M. Ignayatev, type of cutting tool. ONTI, MKT1, USSR, Goshmashmetizdat, 1934.
15. H., R.G., A rotating turning tool bit. Machinery, 1936. 49: p. 247.
16. Ahivchikov, A.V., Machining of Cylindrical Surfaces with Rotating Disc Shaped Tools. Stanki'-i-Instrument, 1950. 7: p. 21.
17. Granin, Y.F., Experimental Investigations on the Life of Circular Self Rotating Tools While Turning Difficult-to-Machine Materials. Sb. Obrabativaemost Zharaprochnikh i titanovikh splavov, Trudi Vessoyuznoi Mezhvuzovskoi Konferentsii, Kuibishev, 1962: p. 208-217.
18. Kooshner, I.S., Investigations on the Turning Process While Working With Circular Self Rotating Tools. Sb. Obrabativaemost Zharaprochnikh i titanovikh splavov, Trudi Vessoyuznoi Mezhvuzovskoi Konferentsii, Kuibishev, 1962: p. 218-229.
19. Reznikov, A.N., Theoretical Fundamentals about Active Cooling of Tools. Sb. Obrabativaemost Zharaprochnikh i titanovikh splavov, Trudi Vessoyuznoi Mezhvuzovskoi Konferentsii, Kuibishev, 1962: p. 247-259.
20. Zemlyanskii, V.A., Investigations on Self Rotating Tools. Izvestia Vuzov Mashinostroenie, 1960. 7: p. 1960.
21. Zemlyanskii, V.A., Kinematics of Machining with Self Rotating Tools. Samoletostroenie i Tekhnika Vozdushnogo Flota, 1963: p. 112-119.
22. Zemlyanskii, V.A., Wear of Circular Self Rotating Tools Expressed as a Function of the Length of Path of Travel of the Cutting edge on the Workpiece. Samoletostroenie i Tekhnika Vozdushnogo Flota, 1965: p. 86-91.
23. Zemlyanskii, V.A., On the Problem of Increasing the Productivity of Machining. Samoletostroenie i Tekhnika Vozdushnogo Flota, 1965: p. 104-111.
24. Zemlyanskii, V.A., Investigation on the Three dimensional Deformation of Metal While Machining with a Circular Self Rotating Tool. Samoletostroenie i Tekhnika Vozdushnogo Flota, 1965: p. 98-105.
25. Zemlyanskii, V.A. and Y.F. Granin, Dynamic Investigations on Circular Self Rotating Tools. Izvestia Visshik Uchebnikzavednli Mashinostrosnie, No. 1, 1965.

26. Zemlyanskii, V.A., Y.F. Granin, and B.V. Starchenko, Circular Self Rotating Tools. *Izvestia PMPTO Obrabotka Metalloy Rezardem*, No. M -62-71/10, 1962. 6(No. M -62-71/10): p. 1960.
27. Zemlyanskii, V., Method of Analyzing the Kinematics of Circular Self-Rotating Tools. *Stanki I Rezh. Instrumentu, Resp. Mezhved, Nauchno Tekhn Sbornik*, 1966. 2: p. 19.
28. Zemlyanskii, V., Cutting Speeds While Machining with Circular Self-Rotating Tools. *Stanki I Rezh. Instrumentu, Resp. Mezhved, Nauchno Tekhn Sbornik*, 1966. 2: p. 43.
29. Zemlyanskii, V., Self Induced Rotation of Round Tool Tips. *Russian Engineering Journal*, 1966. 156(9): p. 66.
30. Granin, Y.F., Investigation on the Longitudinal Chip Reduction while machining with Self Rotating Tools. *Trudi Kharkovskogo Aviatsonnogo Institute*, 1963. 22.
31. Granin, Y.F., Wear and Life of Circular Self Rotating Tools. *Samoletostroenie i Tekhnika Vozdushnaya Flota*, 1965. 2: p. 106-111.
32. Reznikov, A.N. and I.S. Kooshner, Tools with Great Potentials. *Promishlenno Ekonomicheskoi Bulletin, Kuibishev*, 1962: p. 247.
33. Kooshner, I., Circular Self Rotating Tools with Long Life in Turning. *PNPTO, Izd-Vo-KHGU*, 1963. 22(14-63): p. 762.
34. Kooshner, I., Investigations on the Turning Process While Working with Circular Self-Rotating Tools. *Sb. Obrabativaemost Zharaprochnikh I Titaovikh Splavov, Trudi Vessoyuznoi Mezhvuzovski Konferentsii, Kuibishev*, 1962: p. 218.
35. Konovalov, E.G., Finish-milling Plane Surface with a Rotational Tool. *Machines and tooling*, 1972. XVIII(8): p. 46-47.
36. Konovalov, E.G. and L.A. Gik, Application of Rotary Lathe-tools. *Russian Engineering Journal*, 1969. XLIX(8): p. 75-78.
37. Bobrov, V.F. and E.S. Spiridonov, Thermal Phenomena when Cutting with Driven and Freely-rotating Disc-type Lathe Tools. *Russian Engineering Journal*, 1971. LI(6): p. 63-66.
38. Venuvinod, P.K., Analysis of Rotary Cutting Tools. PhD Thesis, University of Manchester,, 1971.

39. Venuvinod, P.K. and P.N. Reddy, Some Studies on Cutting with Self Propelled Rotary Tools. ASME, 1981. 81-WA/Prod-16: p. 1-11.
40. Venkatesh, V., S. Rajesham, and V. Kamala. Wear and surface finish in face-milling with rotary inserts. in Proceedings of 5th AIMTDR conference. 1972.
41. Venuvinocl, P.K., An Investigation to E xplain and Evaluate the Performance of a Rotary Turning Tool. M.Tech. Dis sertation , Indian Institute of Technology, 1965.
42. Venuvinocl, P.K., S. Somasundaram, and N. Ramaswamy Iyer Rotary Tools. Machine Building Industry, India, 1966.
43. Ramaswamy Iyer, N. and F. Koenigsberger, Experiments with Self-Propelled Rotary Cutting Tools. Advances in Machine Tool Design and Research, 9th International M.T.D.R. Conference, Birmingham, 1968: p. 961-973.
44. Karri, V., Fundamental studies of rotary tool cutting processes. 1991, University of Melbourne.
45. Zemlyanskii, V.A. and V. Lubking, Machining of high strength materials using self-propelled rotary cutting tools. National Defence Industry Press, 1983.
46. Qiao, Z., Oblique cutting. The Office of Mass Technology Cooperation, Shenyang City Union, 1978.
47. Anon, Principles and practice in metal cutting. Beijing Publishing House, 1985. 2.
48. Gu, Z. and X. Chang, Self-propelled rotary face milling cutters. New Technology and New Process, 1986. 5: p. 20-22.
49. Bekkala, A.H. and C.H. Kahng, A study on the seld-propelled rotary tool. Manufacturing Engineering Transactions, 7th NAMRC, 1979: p. 255-261.
50. Pauls, F.E., Introduction to the rotary cutter. Cutting Tool Engineering, 1977. 29.
51. Thomas, R.M. and R.L.J. Lawson, Application of a rotary cutting tool. Proc. 17th Int. MTDR Conf., 1976: p. 125-131.
52. Pang, X., An initial study on rotary cutting tools. M.Sc. thesis, Taiyuan Institute of Machinery, 1988.
53. Chang, X. and X. Pang, The application of self-propelled rotary cutting tools. Presented at the 4th Annual Conf. of Shanxi Production Engineering Association, Shanxi, China,, 1989.

54. Zhang, T., Design of the rotary face milling cutter. Pinal year project, Dept. of Mechanical Engineering, Taiyuan Institute of Machinery, 1989.
55. Products introduction. published by Tecmaco International Ltd.
56. Armarego, E., V. Karri, and A. Smith, Computer-aided predictive models for fundamental rotary tool cutting processes. CIRP annals, 1993. 42(1): p. 49-54.
57. Armarego, E., V. Karri, and A. Smith, Fundamental studies of driven and self-propelled rotary tool cutting processes—I. Theoretical investigation. International Journal of Machine Tools and Manufacture, 1994. 34(6): p. 785-801.
58. Armarego, E. and R. Katta, Predictive cutting model for forces and power in self-propelled rotary tool turning operations. CiRP Annals, 1997. 46(1): p. 19-24.
59. Chen, P. and T. Hoshi, High-performance machining of SiC whisker-reinforced aluminium composite by self-propelled rotary tools. CIRP Annals, 1992. 41(1): p. 59-62.
60. Kishawy, H., L. Pang, and M. Balazinski, Modeling of tool wear during hard turning with self-propelled rotary tools. International Journal of Mechanical Sciences, 2011. 53(11): p. 1015-1021.
61. Kishawy, H. and J. Wilcox, Tool wear and chip formation during hard turning with self-propelled rotary tools. International Journal of Machine Tools and Manufacture, 2003. 43(4): p. 433-439.
62. Kishawy, H. and A. Gerber. A model for the tool temperature during machining with a rotary tool. in International mechanical engineering congress and exposition symposium on fundamental issues in machining. 2001.
63. Sasahara, H., et al., High-speed rotary cutting of difficult-to-cut materials on multitasking lathe. International journal of machine tools and manufacture, 2008. 48(7-8): p. 841-850.
64. Oxley, P., The Mechanics of Machining: An Analytical Approach to Assessing Machinability, Ellis Horwood Limited, Chichester, United Kingdom. 1989.
65. Shaw, M.C., Metal cutting principles. Vol. 2. 2005.
66. Merchant, M.E., Mechanics of the metal cutting process. I. Orthogonal cutting and a type 2 chip. Journal of applied physics, 1945. 16(5): p. 267-275.

67. Popović, M., L. Tanović, and K.F. Ehmann, Cutting forces prediction: The experimental identification of orthogonal cutting coefficients. *FME Transactions*, 2017. 45(4): p. 459-467.
68. Armarego, E. and R.H. Brown, *The machining of metals*. PRENTICE-HALL INC, ENGLEWOOD CLIFFS, N. J., 1969, 437 P, 1969.
69. Lee, E., The theory of plasticity applied to a problem of machining. *ASME J. Appl. Mech.*, 1951. 18: p. 405.
70. Shaw, M., N. Cook, and I. Finnie, The shear-angle relationship in metal cutting. *Trans. ASME*, 1953. 75(2): p. 273.
71. Merchant, H.E.-M. and H. Ernst, Chip formation, friction and high quality machined surfaces. *Sur Treat Metal*, 1941: p. 299-378.
72. Palmer, W. and P. Oxley, Mechanics of metal cutting. *Proc. Inst. Mech. Eng*, 1959. 173: p. 623-654.
73. Administration, I., E.P.G.A.M. Group, and G. Boothroyd, Temperatures in orthogonal metal cutting. *Proceedings of the Institution of Mechanical Engineers*, 1963. 177(1): p. 789-810.
74. Stevenson, M. and P. Oxley, An experimental investigation of the influence of speed and scale on the strain-rate in a zone of intense plastic deformation. *Proceedings of the Institution of Mechanical Engineers*, 1969. 184(1): p. 561-576.
75. Johnson, G.R., A constitutive model and data for materials subjected to large strains, high strain rates, and high temperatures. *Proc. 7th Inf. Sympo. Ballistics*, 1983: p. 541-547.
76. Childs, T., Material Property requirements for modeling metal machining. *Journal de Physique(France) IV(France)*, 1997. 7: p. 1.
77. Follansbee, P. and U. Kocks, A constitutive description of the deformation of copper based on the use of the mechanical threshold stress as an internal state variable. *Acta Metallurgica*, 1988. 36(1): p. 81-93.
78. Lin, G., et al., Predicting cutting forces for oblique machining conditions. *Proceedings of the Institution of Mechanical Engineers*, 1982. 196(1): p. 141-148.
79. Bao, H. and M. Stevenson, A basic mechanism for built-up edge formation in machining. *CIRP Ann*, 1976. 25(1): p. 53-57.

80. Lalwani, D., N. Mehta, and P. Jain, Extension of Oxley's predictive machining theory for Johnson and Cook flow stress model. *Journal of materials processing technology*, 2009. 209(12-13): p. 5305-5312.
81. Boothroyd, G., Temperatures in orthogonal metal cutting. *Proceedings of the Institution of Mechanical Engineers*, 1963. 177(1): p. 789-810.
82. Colwell, L.V., Predicting the angle of chip flow for single-point cutting tools. *Transactions of the ASME*, 1954. 76: p. 199.
83. Young, H., P. Mathew, and P. Oxley, Allowing for nose radius effects in predicting the chip flow direction and cutting forces in bar turning. *Proceedings of the Institution of Mechanical Engineers, Part C: Journal of Mechanical Engineering Science*, 1987. 201(3): p. 213-226.
84. Kishawy, H., L. Li, and A. El-Wahab, Prediction of chip flow direction during machining with self-propelled rotary tools. *International Journal of Machine Tools and Manufacture*, 2006. 46(12-13): p. 1680-1688.
85. Li, L. and H. Kishawy, A model for cutting forces generated during machining with self-propelled rotary tools. *International Journal of Machine Tools and Manufacture*, 2006. 46(12-13): p. 1388-1394.
86. Kossakowska, J. and K. Jemielniak, Application of Self-Propelled Rotary Tools for turning of difficult-to-machine materials. *Procedia CIRP*, 2012. 1: p. 425-430.
87. Suzuki, N., et al., Force prediction in cutting operations with self-propelled rotary tools considering bearing friction. *Procedia CIRP*, 2014. 14: p. 125-129.
88. SKF, B., The SKF model for calculating the frictional moment. 2018, SKF.
89. Özel, T. and E. Zeren, Finite element modeling the influence of edge roundness on the stress and temperature fields induced by high-speed machining. *The International Journal of Advanced Manufacturing Technology*, 2007. 35(3-4): p. 255-267.
90. Sartkulvanich, P., T. Altan, and A. Göcmen, Effects of flow stress and friction models in finite element simulation of orthogonal cutting—a sensitivity analysis. *Machine Science and Technology*, 2005. 9(1): p. 1-26.
91. Zerilli, F.J. and R.W. Armstrong, Dislocation-mechanics-based constitutive relations for material dynamics calculations. *Journal of applied physics*, 1987. 61(5): p. 1816-1825.

92. Ceretti, E., M. Lucchi, and T. Altan, FEM simulation of orthogonal cutting: serrated chip formation. *Journal of Materials Processing Technology*, 1999. 95(1-3): p. 17-26.
93. Kountanya, R.K., Process mechanics of metal cutting with edge radiused and worn tools. 2002.
94. Umbrello, D., J. Hua, and R. Shivpuri, Hardness-based flow stress and fracture models for numerical simulation of hard machining AISI 52100 bearing steel. *Materials Science and Engineering: A*, 2004. 374(1-2): p. 90-100.
95. Lin, Z. and S. Lin, A coupled finite element model of thermo-elastic-plastic large deformation for orthogonal cutting. *Journal of engineering materials and technology*, 1992. 114(2): p. 218-226.
96. Johnson, G.R. and W.H. Cook, Fracture characteristics of three metals subjected to various strains, strain rates, temperatures and pressures. *Engineering fracture mechanics*, 1985. 21(1): p. 31-48.
97. Guo, Y. and D.W. Yen, A FEM study on mechanisms of discontinuous chip formation in hard machining. *Journal of Materials Processing Technology*, 2004. 155: p. 1350-1356.
98. Shi, J. and C.R. Liu, The influence of material models on finite element simulation of machining. *Journal of manufacturing science and engineering*, 2004. 126(4): p. 849-857.
99. Sima, M. and T. Özel, Modified material constitutive models for serrated chip formation simulations and experimental validation in machining of titanium alloy Ti-6Al-4V. *International Journal of Machine Tools and Manufacture*, 2010. 50(11): p. 943-960.
100. Guo, Y. and D. Dornfeld, Finite element modeling of burr formation process in drilling 304 stainless steel. *Journal of manufacturing science and engineering*, 2000. 122(4): p. 612-619.
101. Hashimura, M., Y. Chang, and D. Dornfeld, Analysis of burr formation mechanism in orthogonal cutting. *Journal of Manufacturing Science and Engineering*, 1999. 121(1): p. 1-7.
102. Mamalis, A., et al., Finite element simulation of chip formation in orthogonal metal cutting. *Journal of Materials Processing Technology*, 2001. 110(1): p. 19-27.
103. Ramesh, A., Prediction of process-induced microstructural changes and residual stresses in orthogonal hard machining. 2003.

104. Ng, E.-G. and D.K. Aspinwall, Modelling of hard part machining. *Journal of materials processing technology*, 2002. 127(2): p. 222-229.
105. Hancock, J. and A. Mackenzie, On the mechanisms of ductile failure in high-strength steels subjected to multi-axial stress-states. *Journal of the Mechanics and Physics of Solids*, 1976. 24(2-3): p. 147-160.
106. Hillerborg, A., M. Mod er, and P.-E. Petersson, Analysis of crack formation and crack growth in concrete by means of fracture mechanics and finite elements. *Cement and concrete research*, 1976. 6(6): p. 773-781.
107. Calamaz, M., D. Coupard, and F. Girot, A new material model for 2D numerical simulation of serrated chip formation when machining titanium alloy Ti-6Al-4V. *International Journal of Machine Tools and Manufacture*, 2008. 48(3-4): p. 275-288.
108. Zorev, N., Inter-relationship between shear processes occurring along tool face and shear plane in metal cutting. *International research in production engineering*, 1963. 49: p. 143-152.
109. Guo, Y., Q. Wen, and K. Woodbury, Dynamic material behavior modeling using internal state variable plasticity and its application in hard machining simulations. *Journal of Manufacturing Science and Engineering*, 2006. 128(3): p. 749-759.
110. Hua, J. and R. Shivpuri, Prediction of chip morphology and segmentation during the machining of titanium alloys. *Journal of materials processing technology*, 2004. 150(1-2): p. 124-133.
111. Obikawa, T., et al., Application of computational machining method to discontinuous chip formation. *Journal of Manufacturing Science and Engineering*, 1997. 119(4B): p. 667-674.
112. Obikawa, T. and E. Usui, Computational machining of titanium alloy—finite element modeling and a few results. *Journal of Manufacturing Science and Engineering*, 1996. 118(2): p. 208-215.
113. Shirakashi, T. and E. Usui. Simulation analysis of orthogonal metal cutting mechanism. in *Proceedings of the International Conference on Production Engineering*. 1974.
114. Usui, E. and T. Shirakashi, Mechanics of machining—from descriptive to predictive theory. *On the Art of Cutting Metals—75 Years Later*, 1982. 7: p. 13-35.
115. Childs, T., et al., *Metal machining: theory and applications*. 2000: Butterworth-Heinemann.

116. Dirikolu, M., T. Childs, and K. Maekawa, Finite element simulation of chip flow in metal machining. *International Journal of Mechanical Sciences*, 2001. 43(11): p. 2699-2713.
117. Özel, T., The influence of friction models on finite element simulations of machining. *International Journal of Machine Tools and Manufacture*, 2006. 46(5): p. 518-530.
118. Iwata, K., K. Osakada, and Y. Terasaka, Process modeling of orthogonal cutting by the rigid-plastic finite element method. *Journal of Engineering Materials and Technology*, 1984. 106(2): p. 132-138.
119. Bäker, M., The influence of plastic properties on chip formation. *Computational Materials Science*, 2003. 28(3-4): p. 556-562.
120. Bäker, M., Finite element investigation of the flow stress dependence of chip formation. *Journal of Materials Processing Technology*, 2005. 167(1): p. 1-13.
121. Bäker, M., Finite element simulation of high-speed cutting forces. *Journal of Materials Processing Technology*, 2006. 176(1-3): p. 117-126.
122. Madhavan, V. and A. Adibi-Sedeh, Understanding of finite element analysis results under the framework of Oxley's machining model. *Machining Science and Technology*, 2005. 9(3): p. 345-368.
123. Özel, T., Modeling of hard part machining: effect of insert edge preparation in CBN cutting tools. *Journal of Materials Processing Technology*, 2003. 141(2): p. 284-293.
124. Özel, T. and E. Zeren. Finite element modeling of stresses induced by high speed machining with round edge cutting tools. in *Proceedings of IMECE*. 2005.
125. Shet, C. and X. Deng, Residual stresses and strains in orthogonal metal cutting. *International Journal of Machine Tools and Manufacture*, 2003. 43(6): p. 573-587.
126. Priyadarshini, A., S.K. Pal, and A.K. Samantaray, A finite element study of chip formation process in orthogonal machining, in *Dynamic Methods and Process Advancements in Mechanical, Manufacturing, and Materials Engineering*. 2013, IGI Global. p. 197-225.
127. Ye, G., et al., Cutting AISI 1045 steel at very high speeds. *International Journal of Machine Tools and Manufacture*, 2012. 56: p. 1-9.

128. Duan, C., et al., Finite element simulation and experiment of chip formation process during high speed machining of AISI 1045 hardened steel. *International Journal of Recent Trends in Engineering*, 2009. 1(5): p. 46.
129. Parker, G., Self-propelled rotary tool for turning difficult-to-cut materials. 2012, UOIT.
130. Zhang, Y., An assessment of self-propelled rotary tools during machining hardened steel. 2004.
131. Mabrouki, T. and J.-F. Rigal, A contribution to a qualitative understanding of thermo-mechanical effects during chip formation in hard turning. *Journal of Materials Processing Technology*, 2006. 176(1-3): p. 214-221.
132. Wen, Q., Guo, Y. B., & Todd, B. A. (2006). An adaptive FEA method to predict surface quality in hard machining. *Journal of materials processing technology*, 173(1), 21-28.
133. Vaz, M., et al., Modelling and simulation of machining processes. *Archives of computational methods in engineering*, 2007. 14(2): p. 173-204.
134. Ma, J., et al., Numerical investigation of effects of cutting conditions and cooling schemes on tool performance in up milling of Ti-6AL-4V alloy. *The International Journal of Advanced Manufacturing Technology*, 2015. 78(1-4): p. 361-383.
135. Dessoly, V., S.N. Melkote, and C. Lescallier, Modeling and verification of cutting tool temperatures in rotary tool turning of hardened steel. *International Journal of Machine Tools and Manufacture*, 2004. 44(14): p. 1463-1470.
136. Chen, P., Cutting temperature and forces in machining of high-performance materials with self-propelled rotary tool. *JSME international journal. Ser. 3, Vibration, control engineering, engineering for industry*, 1992. 35(1): p. 180-185.
137. Azom. AISI 4140 Alloy Steel (UNS G41400). 2019 [cited 2021; Available from: <https://www.azom.com/article.aspx?ArticleID=6769>].
138. Davim, J.P., *Surface integrity in machining*. Vol. 1848828742. 2010: Springer.
139. Coşkun, S., et al., Evaluation of control parameters' effects on system performance with Taguchi method in waste heat recovery application using mechanical heat pump. *International journal of refrigeration*, 2012. 35(4): p. 795-809.

140. Yang, W.p. and Y. Tarn, Design optimization of cutting parameters for turning operations based on the Taguchi method. *Journal of materials processing technology*, 1998. 84(1-3): p. 122-129.
141. Banzhaf, W., et al., *Genetic programming*. 1998: Springer.
142. Brezocnik, M., M. Kovacic, and M. Ficko, Prediction of surface roughness with genetic programming. *Journal of materials processing technology*, 2004. 157: p. 28-36.
143. Kök, M., E. Kanca, and Ö. Eyercioglu, Prediction of surface roughness in abrasive waterjet machining of particle reinforced MMCs using genetic expression programming. *The International Journal of Advanced Manufacturing Technology*, 2011. 55(9): p. 955-968.
144. Garg, A. and K. Tai. Review of genetic programming in modeling of machining processes. in *2012 Proceedings of International Conference on Modelling, Identification and Control*. 2012. Ieee.
145. Deb, K., et al., A fast and elitist multiobjective genetic algorithm: NSGA-II. *IEEE transactions on evolutionary computation*, 2002. 6(2): p. 182-197.
146. Chen, J. Multi-objective optimization of cutting parameters with improved NSGA-II. in *2009 International Conference on Management and Service Science*. 2009. IEEE.
147. Kishawy, H., C. Becze, and D. McIntosh, Tool performance and attainable surface quality during the machining of aerospace alloys using self-propelled rotary tools. *Journal of materials processing technology*, 2004. 152(3): p. 266-271.
148. Dessoly, V., *Modeling and Verification of Cutting Tool Temperatures in Rotary Tool Turning of Hardened Steel*. 2004, Georgia Institute of Technology.
149. Yamamoto, H., et al. B29 Thermal Behavior and Chip Formation on Rotary Cutting of Difficult-to-cut Materials Utilizing Multi Tasking Lathe and MQL (Advanced machining technology). in *Proceedings of International Conference on Leading Edge Manufacturing in 21st century: LEM21 2009.5*. 2009. The Japan Society of Mechanical Engineers.